Electrolytes and Electrodes for Electrochemical Synthesis of Ammonia

Lapina, Alberto; Holtappels, Peter; Mogensen, Mogens Bjerg

Publication date:
2013

Document Version
Publisher's PDF, also known as Version of record

Electrolytes and Electrodes for Electrochemical Synthesis of Ammonia

Alberto Lapina

Department of Energy Conversion and Storage
Technical University of Denmark
May 2013

Doctoral thesis defended on August 15th, 2013 at the Technical University of Denmark.

Main Supervisor
Dr. Peter Holtappels, Technical University of Denmark

Co-supervisor
Prof. Mogens Mogensen, Technical University of Denmark

Examiners
Prof. John TS Irvine, University of St Andrews, United Kingdom
Dr. L.G.J. de Haart, Forschungszentrum Jülich, Germany
Dr. Tejs Vegge, Technical University of Denmark

Life is like fitting an impedance spectrum: you never know if you are following the right model, you have way too many variables, you are forced to fix some of them arbitrarily, you drive yourself crazy to make sense out of it, and you never fully succeed...

Acknowledgements

First of all I want to thank my supervisor, Dr. Peter Holtappels, for guiding me through these three years of studies. They were a challenging and formative experience, and I appreciated very much his constant guidance and help. I also want to thank my co-supervisor, Prof. Mogens Mogensen, for his insights and for always finding the time to discuss my research. Thanks also go to Christodoulos Chatzichristodoulou for his advice and for sharing his scientific expertise.

I especially thank my dear colleague Jonathan Hallinder, with whom I went through the highs and lows of countless hours of lab work. I greatly appreciated his friendship and it was a real pleasure to work with him.

I am indebted to Sandrine Ricote, for her help and advice, and to Nikos Bonanos and Finn Willy Poulsen, who helped me enter the world of solid state proton conductors. I also want to express my gratitude to Chris Graves for writing the RAVDAV software and to all the technicians, in particular Jens Borchsenius, that helped me every day in carrying out my work.

I will never thank enough my office mates of three years, Pia Lolk Mollerup and Ane Sælland Christiansen, for their friendship, making me feel at home from the very first day, helping me with life in Denmark and trying to teach me Danish. I also want to thank my CASE colleagues Federica Vico and Frank Allebrod, and Hoang Ngan Pham, for their support.

I am grateful to Davide Ippolito, for his friendship and all the conversations and laughs we shared, and to the rest of the "Italian community" of the Department, in particular Francesco Bozza, for being a little piece of Italy abroad for me. A special thought goes also to Carlo Alberto, for being such a good and supportive friend.

Finally, and most importantly, I wish to thank my family, for their constant love and support during these years abroad. I would have never made it without them.

This work was financially supported by The Catalysis for Sustainable Energy (CASE) initiative funded by the Danish Ministry of Science, Technology and Innovation.

Abstract

In order to make Denmark independent of fossil fuels by 2050 the share of renewable energy in electricity production, in particular wind energy, is expected to increase significantly. Since the power output of renewable energy sources heavily fluctuates over time there is a pressing need to find effective energy storage solutions. Production of synthetic fuels (e.g. ammonia) is a promising possibility. Ammonia (NH_3) can be an interesting energy carrier, thanks to its high energy density and the existence of well developed storage and transportation technologies. However the present-day production technology is based on the Haber-Bosch process, which is energy intensive and requires large-scale plants. One possible way to produce ammonia from sustainable electricity, nitrogen and hydrogen/water is using an electrochemical cell. This thesis studies a number of electrolytes and electrocatalysts to evaluate their applicability to electrochemical synthesis of ammonia.

First a number of potential electrolytes are investigated in the temperature range 25-400 °C in order to find a proton conductor with a conductivity higher than 10^{-4} S/cm in dry atmosphere ($p_{H_2O} < 0.001$ atm).

The conductivity of materials prepared from FeOOH nanoparticles is measured at 25-40 °C between $p_{H_2O} = 0.037$ atm and $p_{H_2O} < 0.001$ atm. The conductivity is low in dry air (10^{-6}-10^{-8} S/cm), while it can be up to $7{\cdot}10^{-3}$ S/cm in wet air.

The conductivity of Y-doped Ti, Si, Sn, Zr, Ce pyrophosphates, Gd-doped cerium phosphate and cerium pyrophosphate - KH_2PO_4 composite is measured at 100-400 °C at p_{H_2O} from 0.2 atm to below 0.001 atm. The phase stability and long term conductivity of the compounds with the highest conductivities are investigated, and conductivity is found to depend heavily on p_{H_2O} and phosphorus content.

High temperature solid state proton conductors are briefly reviewed and defect chemistry and partial conductivities of Y-doped $BaZrO_3$-$BaCeO_3$ solid solutions are studied as a function of temperature, p_{H_2O} and chemical compositions by means of defect chemistry modelling.

$BaCe_{0.2}Zr_{0.6}Y_{0.2}O_{2.9}$ (BCZY26) is chosen as electrolyte, and used to fabricate symmetrical cells with composite metal-BCZY26 electrodes. Two metals (iron and molybdenum) are tested as electrocatalysts: the choice is based on the use of catalysts in the Haber-Bosch process and density functional theory calculations.

The symmetrical cells are tested at OCV (i.e. without polarization) by impedance spectroscopy in dry H_2/N_2 and H_2/Ar atmospheres, in the temperature range 440-650 °C for Mo-BCZY electrodes and 350-500 °C for Fe-BCZY electrodes. No clear evidence of activity of Fe and Mo towards nitrogen reduction to ammonia is found. The kinetics of the electrode rea-

ction (hydrogen oxidation/reduction) at the Mo-BCZY electrode are studied in detail by impedance spectroscopy to identify the electrode processes.

Further studies carried out under polarization will be necessary in order to fully assess the potential of Fe and Mo as electrocatalysts for ammonia synthesis.

Dansk resumé

For at gøre Danmark uafhængig af fossile brændstoffer i 2050 er det forventet, at andelen af vedvarende energi der anvendes til at producere elektricitet, især vindenergi, vil stige kraftigt. Idet energiproduktionen fra vedvarende energikilder varierer meget med tiden, er der et stort behov for at finde en effektiv løsning til lagring af energi. Syntetiske brændstoffer, som f.eks. ammoniak, er en lovende mulighed. Ammoniak (NH_3) er en interessant energibærer på grund af den høje energitæthed og tilstedeværelsen af veludviklede lagrings- og transportteknologier. Den nuværende teknologi til produktion af ammoniak er baseret på Haber-Bosch processen, som er energikrævende og derfor kræver fabrikker med storskala produktion. En alternativ metode til at producere ammoniak fra vedvarende elektricitet, nitrogen og hydrogen/vand er ved at anvende en elektrokemisk celle. Denne afhandling undersøger et antal af forskellige elektrolytter og elektrokatalysatorer, for at evaluere deres anvendelighed til elektrokemisk syntese af ammoniak.

Først er et antal af potentielle elektrolytter undersøgt i temperaturintervallet 25-400 °C, for at finde en protonleder med en ledningsevne på over 10^{-4} S/cm i tør atmosfære ($p_{H_2O} < 0.001$ atm).

Ledningsevnen af materialer lavet af FeOOH nanopartikler er målt ved 25-40 °C mellem $p_{H_2O} = 0.037$ atm og $p_{H_2O} < 0.001$ atm. Ledningsevnen er lav i tør luft (10^{-6}-10^{-8} S/cm), mens den kan være op til $7.10 \cdot 10^{-3}$ S/cm i våd luft.

Ledningsevnen af Y-dopet Ti-, Si-, Sn-, Zr-, Ce-pyrofosfater, Gd-dopet ceriumfosfat og ceriumpyrofosfat - KH_2PO_4 komposit er målt ved 100-400 °C ved p_{H_2O} fra 0.2 atm til under 0.001 atm. Fasestabiliteten og ledningsevnen efter langtidstest af materialerne med de højeste ledningsevner er undersøgt, og det blev fundet at ledningsevnen afhænger kraftigt af p_{H_2O} og fosforindholdet.

Højtemperatur faststof-protonledere er kortfattet beskrevet og defektkemi og partial-ledningsevnerne af Y-dopet $BaZrO_3$-$BaCeO_3$ faste blandinger er undersøgt som funktion af temperatur, p_{H_2O} og kemisk sammensætning vha. defektkemi-modellering.

$BaCe_{0.2}Zr_{0.6}Y_{0.2}O_{2.9}$ (BCZY26) er valgt som elektrolyt, og anvendes til at lave symmetriske celler med komposit metal-BCZY26 elektroder. To metaller (jern og molybdæn) er testet som elektrokatalysatorer. Valget af disse er baseret på anvendelsen af katalysatorer i Haber-Bosch processen og på "density functional theory" beregninger.

De symmetriske celler er testet ved OCV (dvs. uden polarisation) med impedansspektroskopi i tørre H_2/N_2 og H_2/Ar atmosfærer, i temperaturintervallet 440-650 °C for Mo-BCZY elektroder og 350-500 °C for Fe-BCZY elektroder. Intet bevis på at Fe og Mo katalyserer reduktionen af nitro-

gen til ammoniak blev fundet. Kinetikken af elektrodereaktionen (hydrogen oxidation/reduktion) på Mo-BCZY elektroden er undersøgt detaljeret vha. impedansspektroskopi for at identificere elektrodeprocesserne.

Det er nødvendigt at udføre flere målinger under polarisation for fuldt ud at kunne karakterisere Fe og Mo som mulige elektrokatalysatorer til ammoniaksyntese.

Contents

List of Figures

List of Tables

Chapter 1

Introduction

1.1 Moving toward a sustainable, energy self-sustaining Denmark by 2050

In 2011 the Danish Government released its energy policy for the coming decades, stating the intention of making Denmark independent of fossil fuels by 2050.[1]

This extremely ambitious target, the first of its kind in the field of energy policy, is meant to be Denmark's response to the challenges that climate change, increasing energy demand and depletion of fossil fuels are putting on our society.

In order to achieve this goal a number of initiatives are planned, both in the short term (e.g. improvements in energy efficiency of the present infrastructure) and in the long term time-scale (research and development of technologies still at the lab-scale).

One of the pillars on which the strategy is built on is achieving a significant increase of the share of renewable energy in electricity production: renewable energy should cover 62 % of the production by 2020 (Figure 1.1).

Wind energy is expected to be the main contributor, given Denmark's great geographic potential and its expertise in this technology. The magnitude of the effort is exemplified by the Kriegers Flak offshore wind farm in the Baltic Sea, due to be built and put in service by 2020: 600 MW worth of wind turbines, enough to cover the electricity consumption of 600000 households.

However, a massive shift from the conventional power generation technologies (man-controlled and highly reliable) to renewable energy sources (whose power output is fluctuating and difficult to predict) is expected to put much stress on the existing energy distribution infrastructure. The Danish energy strategy includes improvements of the electrical grid to build a so-called "smart grid", integrated with the grids of the neighboring countries, in order to accommodate the difference between energy production

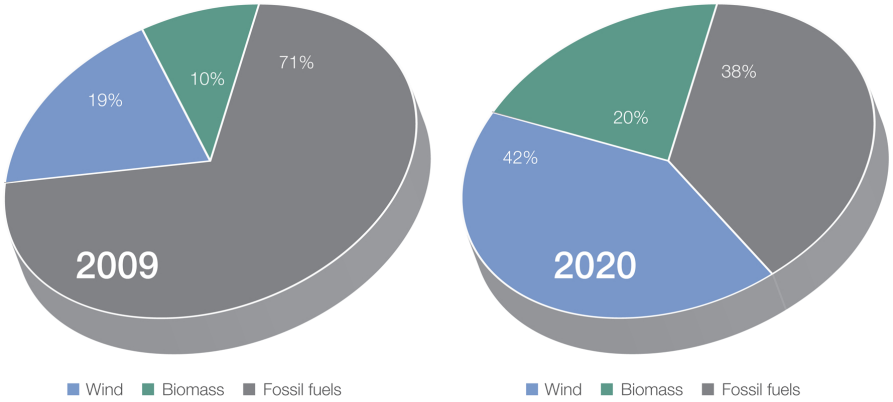

Figure 1.1: Share of renewable energy in Danish electricity production in 2009 and 2020.[1]

and consumption.

Nevertheless a smart energy grid can help only in a limited way in handling significant differences between consumption and production: it is instead necessary to integrate into the system reliable technologies for energy conversion and storage, that would permit to convert the surplus electrical energy production in a form easy to store and to convert again in electrical energy upon need.[2] In particular it is relevant to find a way to store great quantities of energy over long periods of time, e.g. to exploit the greater availability of wind energy during the winter. Moreover, converting and storing energy is pivotal toward powering the transportation sector (which can not always be powered directly by the grid) with sustainable energy.

1.2 Energy storage for sustainable electricity

Nowadays there are a number of energy storage technologies feasible for storage of surplus electrical energy: some of them are well established and extensively used (e.g. pumping water to high altitude repositories for future use in hydroelectric power plants), while others are still under development (e.g. Li-ion batteries). One of the key parameters to evaluate the energy storage potential of an energy source is the energy density (over mass or volume): Table 1.1 gives an overview of such values.

Both high-altitude water storage and batteries have low energy densities: the first is a cheap, feasible option in mountainous regions where hydroelectric plants are available, while batteries are a costly solution, mainly viable for backup solutions, uninterruptible power supply applications and the transportation sector. Hydrogen is an optimal fuel for fuel cells, however, its storage presents technical and economic challenges, particularly in the transportation sector.

Table 1.1: Energy density for different energy sources

Type of storage	Energy density MJ/l	Energy density MJ/kg
Gasoline[2]	33	47
Ammonia (pressurized tank)[3]	13.6	22.5
Ammonia (metal amines tank)[3]	10.4	17.1
Liquid hydrogen[2]	10	141
Li-ion batteries[2]	1	0.5
Lead-acid batteries[2]	0.4	0.15
Water at 1 km elevation[2]	0.01	0.01

Fuels such as hydrocarbons and ammonia are instead very promising. They have a very high energy and power density, and technology and infrastructure are already fully developed. The challenge is finding an efficient way of converting sustainable electricity into fuels. One possible way to produce hydrocarbons from sustainable electricity is to use high-temperature (T > 600 °C) co-electrolysis of H_2O and CO_2 to produce syngas (H_2 + CO), which then can be used to produce liquid hydrocarbons via the Fischer-Tropsch process.[4] The possibility of producing hydrocarbons from co-electrolysis of H_2O and CO_2 in a single step process at 200-300 °C, where hydrocarbons are thermally stable, is currently being investigated at the Technical University of Denmark.[5]

Concerning ammonia, the state-of-the-art production technology and a potential process to produce it from sustainable electricity will be covered in the next sections of the Introduction.

1.3 Ammonia as a fuel

Ammonia (NH_3) is one of the most produced chemicals worldwide, with an annual output of about 160 million tons.[6] More than 80 % of the production is used to prepare fertilizers, while the rest is used in a number of sectors such as refrigeration, transportation, pharmaceuticals and production of explosives.[7]

Ammonia has been first proposed as an energy vector for a hydrogen economy by Green Jr.:[8] as shown in Table 1.1 and stated in Section 1.2, ammonia has a high energy density, comparable with gasoline. It has a large mass fraction of hydrogen (17.65 %)[9] and can be liquified under mild conditions.

Production technology at a large scale is well established, and a good transport technology and infrastructure (ships, pipelines, road/railway tanks) are already well developed thanks to the massive use of ammonia in agriculture and chemical industry.

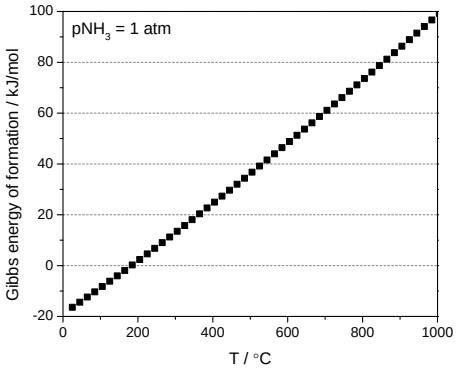

Figure 1.2: Gibbs free energy of formation for $p_{NH_3} = 1$ atm as a function of temperature.

Ammonia meets almost all the US DOE 2015 requirements for hydrogen storage materials.[10] The main issue is its toxicity: gaseous ammonia is poisonous, with an exposure limit of 50 ppm according to the US Occupational Safety and Health Administration regulations.[9] Higher concentrations can be harmful or even fatal, and health effects of long-term exposure to low concentrations are not well known.[9] Nonetheless, years of use in the chemical industry show that this chemical can be handled safely on a large scale. One possible way to address the toxicity issue is to store ammonia in solids, such as metal amine salts,[11] ammonium carbonate and urea.

1.4 The Haber-Bosch process

The main production process for ammonia is the Haber-Bosch catalytic process, which was developed at the beginning of the 20th century and earned one of its inventors, Fritz Haber, the Nobel prize for chemistry in 1918.

The formation reaction of ammonia from its constituents is the following:

$$\frac{1}{2}N_2(g) + \frac{3}{2}H_2(g) \rightarrow NH_3(g) \tag{1.1}$$

The reaction is endothermic ($\Delta_f H^\circ = 45.9$ kJ/mol)[12] and is accompanied by a decrease in volume because of the decrease in number of moles of gas (from 2 to 1). The Gibbs free energy of formation $\Delta_f G$ is plotted in Figure 1.2 as a function of temperature for $p_{NH_3} = 1$ atm.

The reaction proceeds by breaking the nitrogen bond and subsequent protonation of each nitrogen atom.[13] This dissociative mechanism is the reason why the reaction, despite being thermodynamically spontaneous at low temperature ($\Delta_f G$ is negative below ≈ 180 °C at 1 atm) does not take place at room temperature. The triple bond N≡N is one of the strongest

bonds in nature, with a dissociation energy of 945 kJ/mol at 298 K,[12] and to break it both high temperatures (300-500 °C) and appropriate catalysts are necessary: triply promoted iron-based catalysts or promoted ruthenium catalysts are typically used.[14]

However, at high temperatures the reaction is no longer spontaneous at atmospheric pressure. In order to shift the equilibrium and obtain an acceptable ammonia conversion (nowadays around 15 %) it is necessary to use high pressures (200-350 bar). The produced ammonia is then separated by condensation and the unconverted synthesis gas is recycled under pressure, allowing to use all the reactants and thus making the process economically feasible.

Concerning the starting chemicals, nitrogen is extracted from air, with extensive purification needed since ppm levels of oxygen would poison the catalysts.[15,16] Hydrogen is mainly produced from methane by steam reforming and water gas shift reaction;[17] the conversion of methane to ammonia has a energy efficiency of about 60-65 %.[10] Production of 1 ton of NH_3 requires on average 36.6 GJ[18] and generates 1.87 tons of CO_2:[15] considering the massive quantities of NH_3 produced, it is easy to understand how the process is a major contributor to fossil fuel utilisation and greenhouse gases emission.

The technical and economical complexity of the Haber-Bosch process (high temperatures, high pressures, gas recycling systems, high capital costs, etc.) make the ammonia production economically feasible only in large scale chemical plants, with production capabilities of thousands of tons of ammonia per day.[19]

One possible alternative process that is still at an early research stage is electrochemical synthesis of ammonia, which is presented in the next section.

1.5 Electrochemical synthesis of ammonia

The purpose of electrochemical synthesis of ammonia is to carry out ammonia synthesis from nitrogen and hydrogen (or water) via an electrochemical cell, using electrical energy to power the process. Ideally such a process would permit to convert sustainable electricity (such as the one produced by wind energy) into ammonia, which can be used either as a synthetic fuel or as a chemical.

An electrochemical cell basically consists of three parts: electrolyte, anode and cathode. The electrolyte is an ion conductor that separates the electrodes and permits the transport of ions from one electrode to the other. At the anode and cathode the oxidation and reduction reactions take place, respectively. The electrodes are connected via an external electrical circuit that allows transport of electrons from one electrode to the other, closing the circuit.

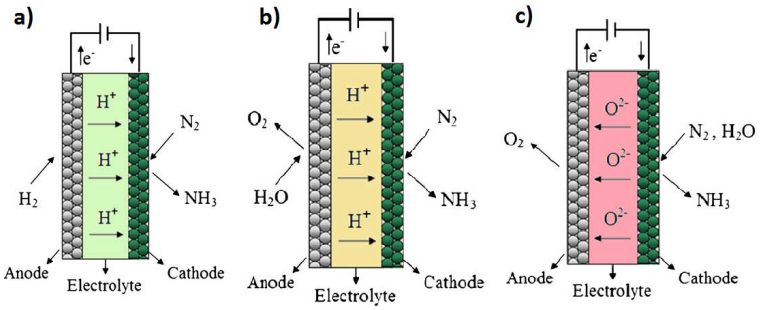

Figure 1.3: Schematic of an electrochemical cell for ammonia synthesis: a) proton conducting electrolyte, using H_2 and N_2 b) proton conducting electrolyte, using H_2O and N_2, c) oxide-ion conducting electrolyte, using H_2O and N_2. Reproduced from Amar *et al.*[7]

The overall chemical reaction taking place in the cell (in the case of ammonia synthesis, Reaction 1.1) is split into two electrode reactions, each taking place at one of the electrodes. The exact form of the electrode reactions depends on the electrolyte (whether it is a proton or oxide ion conductor) and on the source of protons (hydrogen or water): Figure 1.3a-c provides an overview of the different cases.

For a cell based on a proton conducting electrolyte the electrode reactions are:[20]

$$Anode: \quad \frac{3}{2}H_2 \rightarrow 3H^+ + 3e^- \; or \; \frac{3}{2}H_2O \rightarrow 3H^+ + \frac{3}{4}O_2 + 3e^- \tag{1.2}$$

$$Cathode: \quad \frac{1}{2}N_2 + 3H^+ + 3e^- \rightarrow NH_3 \tag{1.3}$$

The two possible anode reactions correspond to the cells shown in Figure 1.3a and 1.3b respectively.

For a cell based on an oxide-ion conducting electrolyte (Figure 1.3c) the electrode reactions are instead:[21]

$$Anode: \quad \frac{3}{2}O^{2-} \rightarrow \frac{3}{4}O_2 + 3e^- \tag{1.4}$$

$$Cathode: \quad \frac{3}{2}H_2O + \frac{1}{2}N_2 + 3e^- \rightarrow \frac{3}{2}O^{2-} + NH_3 \tag{1.5}$$

A number of studies using different combinations of electrolytes and electrode materials have been carried out by a number of research groups and have been recently summarized in the first review on electrochemical synthesis of ammonia.[7]

The studies can be roughly divided in two categories, depending on the operating temperature range of the electrochemical cell: low temperature (T < 100 °C) and high temperature (400 °C < T < 750 °C).

1.5.1 Low temperature (T < 100 °C)

Kordali *et al.*[22] use a cell with a KOH solution as electrolyte (and Nafion as separation membrane), Pt anode and Ru/C cathode to produce ammonia (maximum formation rate $r \approx 2{\cdot}10^{-11}$ mol s^{-1} cm^{-2} at 90 °C) from hydrogen and nitrogen with a 0.2-1 % faradaic efficiency (i.e. the percentage of hydrogen transported through the electrolyte used for ammonia synthesis).

Other groups use instead proton exchange membranes as electrolytes, such as sulfonated polysulfone (SPSF) membranes,[23] Nafion membranes[23–25] or NH^{4+} substituted Nafion membranes.[15] Xu *et al.*[25] report a maximum ammonia formation rate of $1.13{\cdot}10^{-8}$ mol s^{-1} cm^{-2} at 80 °C with an applied voltage of 2 V, using a Nafion membrane, a NiO-$Ce_{0.8}Sm_{0.2}O_{2-\delta}$ anode and a $SmFe_{0.7}Cu_{0.1}Ni_{0.2}O_3$ cathode and hydrogen and nitrogen as reactants. High faradaic efficiencies (up to 90 %) are reported, differently from what is reported by the other authors testing ammonia synthesis at low temperature.[15,22]

According to Lan, Irvine and Tao,[15] ammonia (a weak base) likely reacts with an acidic membrane such as Nafion, leading to a decrease in proton conductivity.[15] Therefore they propose the use of a Nafion membrane converted from H^+ form to NH^{4+} form by exposing the cell to a flow of ammonia solution. Using Pt/C electrodes they report for the first time the synthesis of ammonia from air and water at room temperature and atmospheric pressure ($r = 1.14{\cdot}10^{-9}$ mol s^{-1} cm^{-2}), with a faradaic efficiency below 1 %. The low faradaic efficiency is according to the authors due to Pt not being the best catalyst for nitrogen reduction. The use of air as nitrogen source is remarkable since replacing pure nitrogen with air could allow to simplify the system: however it has been reported elsewhere that oxygen would poison the catalyst,[16] despite the fact that the authors do not report significant changes in faradaic efficiency using pure N_2 or air as nitrogen source.[15]

It is worth pointing out that the voltage required to drive the reaction differs depending on the reactants of choice and on the experimental conditions (Figure 1.4). At low temperature ammonia formation from nitrogen and hydrogen is spontaneous, therefore the minimum required voltage is actually negative (i.e. it should not be necessary to apply a voltage). In reality an applied voltage is necessary to overcome the electrode overpotentials and the ohmic losses in the electrolyte occurring when a finite current passes through the cell (these contributions are not accounted for in Figure 1.4). If instead water is used as source of hydrogen, an applied voltage is required to drive the reaction.

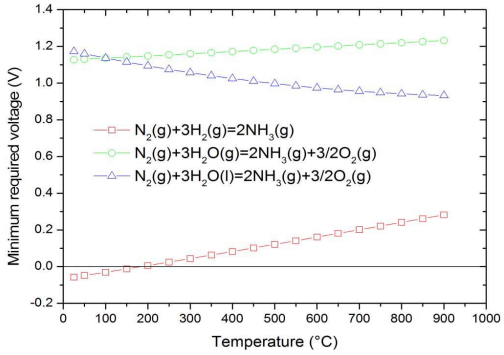

Figure 1.4: Minimum applied voltage necessary for electrochemical synthesis of ammonia from N_2 and H_2 or H_2O at 1 bar. Reproduced from Lan *et al.*[15]

1.5.2 High temperature (400 °C < T < 750 °C)

Solid state proton or oxide-ion conductors are used as electrolytes in the electrochemical synthesis of ammonia at high temperature. The process has been intensively studied by Marnellos, Stoukides *et al.*[20,21,26–28] using both proton and oxide-ion conductors. Skodra and Stoukides[21] synthesize ammonia from steam and nitrogen at 450-700 °C using an industrial Ru catalyst, supported on Ag or Pd, as cathode and $SrCe_{0.95}Yb_{0.05}O_{3-\delta}$ (proton conductor) or $ZrY_{0.92}Y_{0.08}O_{2-\delta}$ (oxide-ion conductor) as electrolyte. For both the cells they report ammonia formation rates in the order of 10^{-12}-10^{-11} mol s^{-1} cm^{-2}, with faradaic efficiencies that can be estimated to be about 0.01 %. This is different from what is reported by Marnellos and Stoukides[20] and Marnellos, Zisekas and Stoukides[26] that present faradaic efficiencies of 90 % using H_2 and N_2 in a cell with $SrCe_{0.95}Yb_{0.05}O_{3-\delta}$ electrolyte and Pd electrodes.

In all these studies the ionic currents (i.e. the rates of ion transport through the electrolyte) are of the same order of magnitude, but the ammonia formation rates are circa 3 orders of magnitude lower in the work by Skodra and Stoukides.[21] From the data and the experimental information reported by Marnellos, Zisekas and Stoukides[26] it is possible to estimate that the NH_3 concentration in the gases should be circa 50 ppm. When the ammonia formation rate is 3 order of magnitude lower, the NH_3 concentration should be less than 1 ppm. The ammonia concentrations obtained are thus extremely low.

One of the main drawbacks of synthesis of ammonia at high temperature is that it may decompose thermally right after synthesis. One possible way to address the issue can be to design the reactor in such a way that the smallest possible region of it is operating at high temperature.[21,26]

Liu *et al.*[29] report ammonia formation rates of 2-7·10^{-9} mol s^{-1} cm^{-2} at 400-800 °C using $Ce_{0.8}M_{0.2}O_{2-\delta}$ (M = La, Y, Gd, Sm) as electrolyte and Ag-Pd electrodes, claiming faradaic efficiencies higher than 100 %. However, this should not possible in the setup used by the authors, since (excluding leaks) all the hydrogen available for ammonia formation is supplied via the electrolyte as protons.

A number of works by another research group, using Ag-Pd electrodes on doped barium cerates electrolytes at 400-600 °C, report ammonia formation rates in the 1-5·10^{-9} mol s^{-1} cm^{-2} range[30–38] and faradaic efficiencies of about 40-50 %.

Amar *et al.*[39,40] use composite carbonate-oxide composite electrolytes at 400-450 °C. The maximum ammonia formation rate reported is 5.39·10^{-9} mol s^{-1} cm^{-2} at 450 °C, with a $La_{0.6}Sr_{0.4}Fe_{0.8}Cu_{0.2}O_{3-\delta}$ - $Ce_{0.8}Sm_{0.2}O_{2-\delta}$ composite cathode, NiO-$Ce_{0.8}Sm_{0.2}O_{2-\delta}$ anode and composite $Ce_{0.8}Sm_{0.2}O_{2-\delta}$-$Li_2CO_3$ - Na_2CO_3-K_2CO_3 electrolyte.

A completely different concept of cell for electrochemical synthesis of ammonia has been proposed by Murakami *et al.*[41–47] In this cell the mobile ion is N^{3-}, that is contained in a molten salt electrolyte (LiCl-KCl-CsCl) at 300-400 °C and is formed at the anode by reducing nitrogen gas. The nitride ions either react with hydrogen at the anode,[41,47] or with a hydrogen-containing chemical (water,[43,47] HCl,[42] H_2S[45]) to produce ammonia. Ammonia formation rates of circa 10^{-8} mol s^{-1} cm^{-2} are obtained.[43,46] A similar cell concept has also been patented in the USA by Denvir *et al.*[48,49] on behalf of Lynntech Inc.

1.5.3 Main challenges for the development of electrochemical synthesis of ammonia

The overview of the literature presented in Sections 1.5.1 and 1.5.2 shows how the research on electrochemical synthesis of ammonia is still at an early stage and faces considerable challenges. Ammonia has been produced electrochemically, but the formation rates obtained are not of technical interest.

It is, therefore, necessary to increase ammonia formation rates, both by using higher current densities and improving the efficiency of the process. In order to do so it is pivotal to minimize the electrolyte resistance, by increasing the electrolyte conductivity and/or decreasing its thickness, particularly for the solid-state ionic conductors used at high temperature. In general, a low operating temperature is to be preferred to avoid thermal decomposition of ammonia.

In order to ensure high faradaic efficiencies, hydrogen evolution at the cathode must be minimized. Therefore it is imperative to use electrocatalysts favoring the nitrogen reduction reaction over hydrogen evolution. So far, a number of noble metal catalysts have been used, such as Pd, Pt and Ru,[15,21,26] however these metals are not the optimal choice. Any fur-

ther work should take into account the results of the Density Functional Theory (DFT) screening studies aimed at identifying suitable electrocatalysts.[13,16,50–52] It must also be pointed out that oxygen and water may poison the cathode catalysts,[16] therefore the cathode should operate at low p_{H_2O} and p_{O_2}. In that respect, it would be suitable to use an electrolyte able to provide proton conductivity in dry conditions (i.e. at very low water partial pressures).

1.6 Objective and outline of the thesis

The objective of the present thesis is to develop a proof-of-concept electrochemical cell for synthesis of ammonia from nitrogen and hydrogen, operating within the temperature range 25 - 500 °C and using an electrolyte having proton conductivity in dry atmosphere ($p_{H_2O} < 0.001$ atm): in order to develop such a cell, it is necessary to identify and test suitable electrolytes and electrocatalysts.

In Part I a number of possible electrolytes are considered, with the aim of finding an electrolyte with proton conductivity in dry atmosphere ($p_{H_2O} < 0.001$ atm) high enough (i.e. $\sigma > 10^{-4}$ S/cm) to allow testing of electrocatalysts.

Since low temperatures permit to avoid thermal decomposition of ammonia, the investigation is started with a candidate that offers a possibility for use as electrolyte at room temperature. Chapter 2 studies iron oxyhydroxide / iron oxide materials fabricated from FeOOH nanoparticles (ferroxanes) and their conductivity is investigated at 25-40 °C over a wide range of water partial pressures.

Chapters 3, 4 and 5 cover instead an extensive investigation of acceptor-doped pyrosphosphates and phosphates (MeP_2O_7, with Me = Ti, Zr, Ce, Sn, Si), which have potential as intermediate proton conductors. The work leading to this part of the research has been equally shared between the author of the present thesis, Dr. J. Hallinder and Dr. C. Chatzichristodoulou in the framework of the CASE (Catalysis for Sustainable Energy) project.

Chapter 3 studies the conductivity and thermal stability of Y-doped Si, Sn, Zr and Ce pyrophosphates, and their degradation over time is investigated to assess their potential as electrolytes.

Chapter 4 investigates the effect of sintering temperature on the conductivity of Y-doped TiP_2O_7, in particular to assess how the phosphorus content influences the conductivity.

Chapter 5 focuses on Ce phosphate compounds, which have promising conductivities. Y and Gd doping are considered, together with a composite with KH_2PO_4. The thermal evolution and the long term conductivity of the compounds are investigated.

Chapter 6 provides a short literature survey of high-temperature solid

state proton conductors and a semi-quantitative study of defect concentrations and partial conductivities in Y-doped $BaZrO_3$-$BaCeO_3$ solid solutions.

Chapter 7 compares the different materials considered and explains the reason behind the choice of electrolyte to use in the second part of the thesis.

In Part II of the thesis the most promising electrolyte is used to fabricate symmetrical cells and test electrocatalysts suggested by DFT calculations carried out by coworkers within the CASE project.[13,52]

Chapter 8 reports a study on composite Fe-BCZY26 electrodes. Iron is chosen as possible candidate since it is the standard Haber-Bosch catalyst.

Chapter 9 presents a detailed impedance spectroscopy study of composite Mo-BCZY electrodes. Molybdenum is, according to DFT calculations, the best possible candidate for electrochemical synthesis of ammonia. Its potential is assessed and the kinetics of the reaction at the electrode are studied.

Finally, the main conclusions of this work and the outlook are presented in Chapter 10.

Part I

Electrolytes

The aim of Part I of the thesis is to identify an electrolyte with a proton conductivity in dry atmosphere (i.e. $p_{H_2O} < 0.001$ atm) higher than 10^{-4} S/cm. This minimum requirement is due to the need of having acceptable proton conductivity to be able to test electrocatalysts on a proton conducting cell.

A number of materials expected to be conductive in the temperature range 25-500 °C are considered as possible electrolyte.

Based on experimental results and literature data, the electrolyte candidates are compared and one material is chosen for fabricating electrochemical cells to test electrocatalysts.

Chapter 2

Ferroxanes-derived materials[1]

Since low temperatures permit to avoid thermal decomposition of ammonia, the first candidate offers a possibility for use as electrolyte at room temperature. Iron oxyhydroxide / iron oxide materials are fabricated from FeOOH nanoparticles (ferroxanes) and their conductivity is investigated at 25-40 °C over a wide range of water partial pressures.

Abstract

Carboxylic-acid-stabilised γ-FeOOH particles (ferroxanes) are synthesized using a precipitation from acqueous solution, and a following reaction with acetic acid. The materials produced with these powders are investigated by XRD, SEM, nitrogen adsorption-desorption and impedance spectroscopy. Conductivity of both sintered and unsintered materials decreases strongly with a decrease in water partial pressure in the atmosphere during the test. The highest conductivity ($7 \cdot 10^{-3}$ S/cm) is measured in air (p_{H_2O} = 0.037 atm) at room temperature on sintered material. The conductivity values are compared with other works in the literature and the dependence of conductivity on surface area and pore size is discussed. It is suggested that both unsintered and sintered materials act as proton conductors at room temperature under moderate humidity conditions.

2.1 Introduction

There is nowadays a deep interest in the development of fuel cells and electrolyzers based on proton conducting electrolytes. Such devices span from

[1]Published as: A. Lapina, P. Holtappels, M. Mogensen, "Conductivity at Low Humidity of Materials Derived from Ferroxane Particles", *International Journal of Electrochemistry*, vol. 2012, Article ID 930537

proton exchange membrane fuel cells (PEMFCs) to proton conducting ceramic fuel cells (PCFCs). In all these cells the functional behavior of the electrolyte is strongly dependent on the humidity of the atmosphere in which it operates: in particular Nafion membranes used in PEMFCs require high relative humidity to retain high proton conductivity.[53] In order to simplify the fuel cell system it is convenient to use an electrolyte stable in low humidity conditions, and whose proton conductivity is independent of humidity. Moreover some applications, such as electrochemical synthesis of ammonia,[7,16] could require the electrochemical system to work in low humidity conditions.

During the last decade materials derived from carboxylic-acid-stabilized γ-FeOOH nanoparticles (ferroxanes) have been investigated as proton conductors by Tsui, Rose, Wiesner *et al.*[54–56] These studies report conductivities up to $2.65 \cdot 10^{-2}$ S/cm at room temperature[54] and for some of the materials investigated the conductivity is reported to be almost independent of the relative humidity in the range 30–100% at room temperature (equivalent to p_{H_2O} = 0.0096–0.032 atm). These materials are therefore interesting candidates as proton conducting electrolytes.

The model proposed for the conduction mechanism[54,57] suggests two main mechanisms for proton conduction, both at the surface of the material: conduction by hydroxyl groups in a chemisorbed water layer and conduction in a physisorbed water layer.

In low humidity conditions, the physisorbed layer is absent and only a chemisorbed layer (that gets formed on first contact with water vapor) is present; this layer is reported not to be affected by changes in humidity, but to be removable if the temperature is increased.[54] The conduction takes place by proton hopping between the hydroxyl groups.

At higher humidity layers of physisorbed water cover the surface and protons combine with water molecules forming H_3O^+, then hop to the neighbor water molecules in the layer: this process is known as Grotthuss chain reaction.[54]

In a recent work Guo and Bernard[58] studied by DFT calculations the possibility of having proton transfer between OH groups on the side of the Fe octahedra sheets in the layered structure of lepidocrocite (γ-FeOOH). Such a process is reported to have a moderate energy barrier, and is theoretically independent of the hydration conditions. However, the conductivity of the material is expected to be extremely anisotropic since the proton conduction takes place only parallel to the layers.

In this chapter, I measure the conductivity of unsintered and sintered material produced from ferroxanes powders. I study it in a range of low humidities at 25 °C and 40 °C.

2.2 Experimental

2.2.1 Synthesis

The lepidocrocite (γ-FeOOH) and ferroxane powders are prepared by a synthesis procedure based on what is reported in the literature.[54,56,57] The synthesis procedure is shown in Figure 2.1 and described hereunder.

A NaOH aqueous solution (0.2 M) is added to a $FeCl_2{\cdot}4H_2O$ solution (0.12 M) under stirring, keeping a ratio $[FeCl_2{\cdot}4H_2O]/[NaOH]=0.6$, which is reported to favor the formation of pure lepidocrocite.[56,59] This produces a suspension having a dark green colour, which is stirred at room temperature for 12–20 hours, until it turns orange in colour. The suspension is centrifugated for 1–2 hours at 4000 rpm (Sigma 2-16 centrifuge) to separate the lepidocrocite particles from the liquid and the NaCl contained in it. The lepidocrocite particles obtained by centrifugation are dried at 90 °C and then dissolved again in distilled water, together with pure acetic acid (CH_3COOH), keeping a ratio [Fe/AA]=1.5. The dispersion is again stirred at room temperature for 12–20 hours and centrifugated for 1–2 hours at 4000 rpm. The reactions taking place have been described by Rose *et al.*[56]

The obtained ferroxane powders are dried at 90 °C, manually ground and pressed into pellets (diameter 8 mm, thickness 0.9–1.2 mm) by uniaxial pressing (600 GPa). While half of the pellets are not sintered (i.e. "green" pellets), half of them undergo sintering in air (4 hours at 300 °C or 500 °C, 1 °C/min heating and cooling rates).

XRD analysis of powders and both green and sintered pellets is carried out using a STOE X-Ray diffractometer (Cu K-α radiation, acceleration voltage 40 kV, filament current 30 mA). The materials are imaged with a scanning electron microscope (Zeiss SUPRA SEM). The samples are attached to a metal sample holder using carbon tape and coated with a thin layer of carbon using a sputter coater.

2.2.2 Nitrogen adsorption-desorption

Surface area and pore size distribution are measured by nitrogen adsorption-desorption using an Authosorb-1MP instrument (Quantachrome Instruments, Germany). Manually grinded samples are degassed at 120 °C for 10 hours prior to adsorption/desorption. Samples of circa 0.1 g are measured using nitrogen as adsorbate gas. The isotherms obtained are used to calculate the surface area and the pore size distribution.

2.2.3 Electrochemical testing

Both unsintered ("green") and sintered pellets are tested, using the same electrodes on both faces of each pellet. Two different kinds of electrodes are used. Disks of carbon paper loaded with Pt nanoparticles (IRD Fuel Cells,

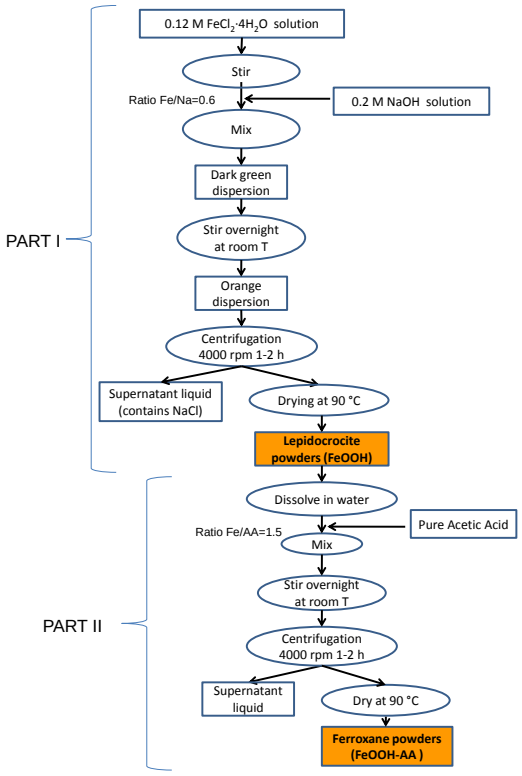

Figure 2.1: Flow chart for the ferroxane powders synthesis procedure

Denmark) are put in contact with both the faces of the pellet to act as electrodes. Gold electrodes (about 500 nm thick) are deposited by plasma sputtering with a deposition rate of 27 nm/min. The electrical connections to the electrodes are ensured by pressing a Pt mesh on them.

Electrochemical measurements are conducted at room temperature (24–30 °C) or at 40 °C, under a constant flow (50 ml/min) of air. The gas is either dry (i.e. non humidified, $p_{H_2O} \approx 0.001$ atm) or humidified by bubbling through a water bottle held at 12 °C ($p_{H_2O} = 0.014$ atm) or 28 °C ($p_{H_2O} = 0.037$ atm). The measurements reported in this work are carried out once the system has reached equilibrium: depending on the parameter changed (temperature, p_{H_2O}), up to 50 hours can be necessary to reach it.

Two-points impedance spectroscopy is performed using a Solartron 1260 Frequency Response Analyzer (Solartron Analytical, UK). Impedance spectra are recorded in the frequency range 980 kHz – 1.23 Hz applying a sinusoidal signal with an amplitude of 0.2 V, and are analyzed with commercial softwares ZView (Scribner Associates, USA) and ZSimpWin (EChem Software, USA).

The conductivity σ of the material is calculated with the following equation:

$$\sigma = \frac{t}{R \cdot A} \tag{2.1}$$

where t is the thickness of the tested pellet, A is the area of the cross section of the pellet (0.5 cm^2) and R is the electrolyte resistance.

2.3 Results

2.3.1 X-ray diffractometry

The XRD patterns for lepidocrocite particles and ferroxane particles, i.e. before and after exposure to acetic acid, are reported in Figure 2.2. In both cases the only phase detected is lepidocrocite (γ-FeOOH, PDF number 0044-1415), proving that the crystallographic structure of the powders remains unchanged upon exposure to acetic acid.

Sintering at 300 °C induces a phase transformation in the material, which becomes maghemite (γ-Fe_2O_3, PDF number 0025-1402), as shown in Figure 2.3a: the peak at $2\theta = 44.2°$ is due to the sample holder.

Since in this study I am interested in making a comparison with the studies carried out by other groups on hematite,[54,60,61] I sinter the material at higher temperature to obtain hematite. According to DTA measurements by Ye *et al.*[62] the phase transition temperature between nanocrystalline maghemite and hematite is between 440 °C and 550 °C. In this work sintering at 500 °C gives single-phase hematite (α-Fe_2O_3, PDF number 033-0664), as shown in Figure 2.3b.

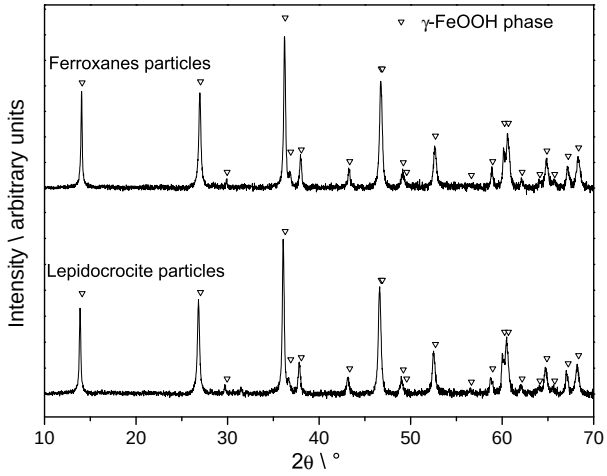

Figure 2.2: XRD diffractograms of lepidocrocite particles and ferroxane particles. The identical patterns show that the crystallographic structure of the powders remains unchanged upon exposure to acetic acid.

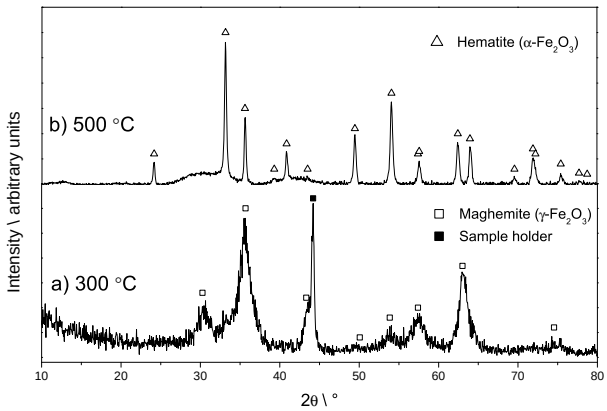

Figure 2.3: XRD diffractograms of pellets sintered for 4 hours at: a) 300 °C, b) 500 °C. The peak at $2\theta = 44.2°$ is due to the sample holder.

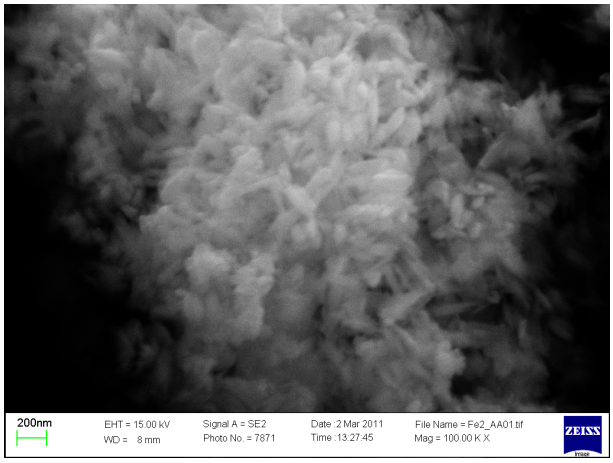

Figure 2.4: SEM image of ferroxane particles.

2.3.2 Nitrogen adsorption-desorption

The ferroxanes, maghemite and hematite powders have surface areas of 55 m^2/g, 103 m^2/g and 22 m^2/g respectively. The surface area doubles upon sintering at 300 °C, but decreases dramatically if the sintering is carried out at 500 °C.

Pore size distribution measurements show that all the powders have a very large average pore size, above 200 nm. Pores with size in the 2-20 nm range are present in the ferroxanes particles and in greater quantity in the maghemite particles, but they are absent in the hematite particles.

2.3.3 SEM imaging

A SEM image of the ferroxanes powder is reported in Figure 2.4: the particles have an elongated shape, with a length of about 300 nm and a width of 100-150 nm, and exhibit significant agglomeration. The cross sections of a green pellet (i.e. produced pressing the powders shown in Figure 2.4) and of a pellet sintered at 300 °C are shown in Figure 2.5.

2.3.4 Electrochemical testing

To describe the impedance spectra measured at moderate humidity I propose the equivalent circuit $R(C(R_1(WR_W)))(R_{el}Q_{el})$, presented in Figure 2.6 together with an example of impedance spectrum.

In this circuit C is assumed to be the geometrical capacitance of the system, W the infinite Warburg impedance element describing the diffusion of charge carriers in the water in the pores of the material, R_W the resistance to the charge carriers movement along the physisorbed/chemisorbed layer of water on the particles, and R_{el} and Q_{el} respectively the resistance and

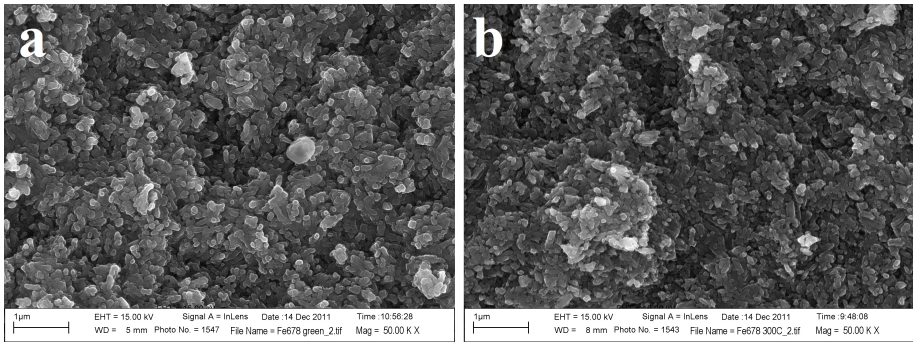

Figure 2.5: SEM image of a cross section (fracture) of (a) green pellet and (b) pellet sintered at 300 °C, both not tested electrochemically.

the constant phase element associated with the electrode process.[63] Such a model, with two conduction mechanisms and an additional electrode mechanism, is in general agreement with the conduction mechanisms proposed so far for these materials. At higher humidities the resistance of the electrolyte processes decreases significantly and the impedance spectrum is dominated by the electrode contribution. At low humidity instead the electrolyte resistance increases and only one electrolyte process can be identified in the spectrum, while the electrode response is negligible.

The present data do not permit a deeper evaluation of the single contributions to the impedance of the material, therefore in the following only the total resistance of the electrolyte is considered to calculate its conductivity.

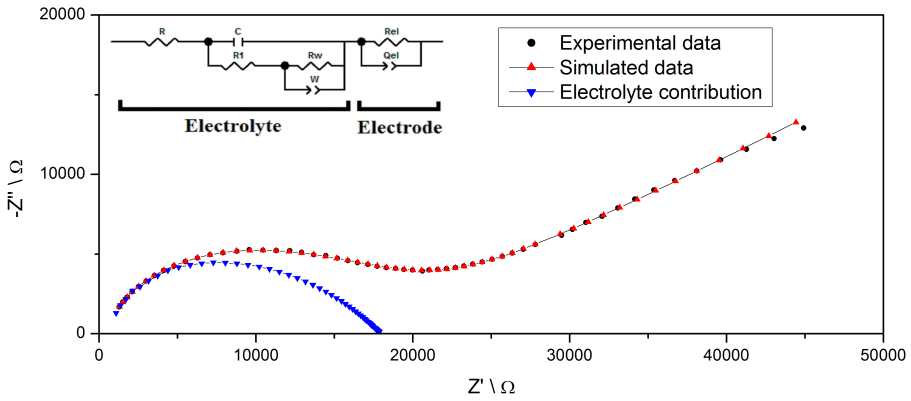

Figure 2.6: Nyquist plot for material sintered at 300 °C and tested at 40 °C in air, p_{H_2O} = 0.037 atm, using C-Pt electrodes. The "Simulated data" curve shows the results of the fitting using the equivalent circuit represented, while the "Electrolyte contribution" curve shows the contribution of the first part of the circuit.

Conductivity versus p_{H_2O} at room temperature and at 40 °C is reported in Figures 2.7 and 2.8 respectively. At both the temperatures the conduc-

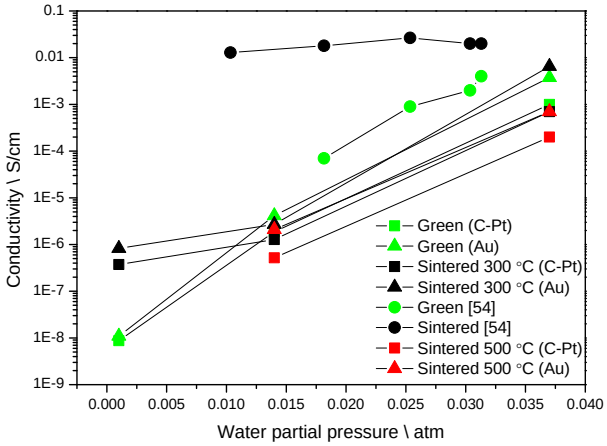

Figure 2.7: Conductivity versus water partial pressure, for materials tested in air at room temperature.

tivity of all the materials decreases of orders of magnitude upon reducing water partial pressure. At $p_{H_2O} = 0.037$ atm green material and material sintered at 300 °C (maghemite) have about the same conductivity, while it is about one order of magnitude lower for the material sintered at 500 °C (hematite). At lower humidities the material sintered at 300 °C shows the highest conductivity: this is particularly evident in Figure 2.8. The general trend in conductivity at low humidities is $\sigma_{300°C} > \sigma_{green} > \sigma_{500°C}$. The conductivity of the material sintered at 500 °C at $p_{H_2O} = 0.001$ atm is not reported in Figures 2.7 and 2.8 because it is too low to be measured.

Concerning the effect of temperature, a comparison of Figures 2.7 and 2.8 shows that conductivities measured at $p_{H_2O} = 0.037$ atm are significantly lower at 40 °C than at room temperature.

2.4 Discussion

2.4.1 Crystallographic structure

The powders have the crystallographic structure of lepidocrocite (γ-FeOOH) both before and after the treatment with acetic acid, which is consistent with previous literature reports.[56] After sintering at 300 °C maghemite (γ-Fe_2O_3) is obtained instead of hematite (α-Fe_2O_3) as reported by Rose *et al.*[56] In this work, sintering at 500 °C was necessary to obtain pure hematite.

In the present work the ferroxane powders are used to fabricate pellets by uniaxial pressing, while other authors fabricate unsupported[54,55] and glass fibers supported[64] membranes by drying a suspension of particles. The green pellets and the hematite pellets in this work have therefore the same crystallographic structure as the material reported in other works, but the

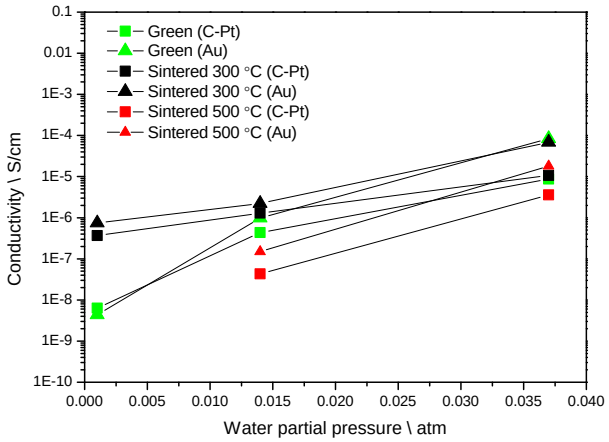

Figure 2.8: Conductivity versus water partial pressure, for materials tested in air at 40 °C.

microstructure is different because of the different fabrication procedure. A not-pressed thin membrane is expected to have a lower density than my material.

2.4.2 Conductivity

The conductivity of the green material presented in this work shows the same trend versus humidity as the one presented by Tsui *et al.*,[54] but with values 1-2 orders of magnitude lower. Also the sintered materials show a decrease in conductivity with a decrease in humidity, while Tsui *et al.*[54] report almost constant conductivities down to 30 % relative humidity.

Such differences can be explained taking into account the surface area and the pore size of the particles in the two studies. The values of surface areas in this work are quite similar to the ones reported by Tsui, and follow the same trend: sintering at 300 °C increases surface area, while sintering at higher temperatures causes a decrease. On the contrary, the average pore size is very different: while it is above 200 nm in the present work for all the powders, Tsui reports values in the 10-40 nm range.

These results support the hypothesis, suggested by Colomer and Anderson,[65] that the effect of pore size on the proton conductivity is more important than the effect of the surface area.

It has been suggested[54] that both macroporosity (pore sizes > 50 nm) and microporosity (pore sizes < 2 nm) can be detrimental to proton conductivity, while a mesoporous structure (2 nm $<$ pore sizes $<$ 50 nm) is the best option to maximize the proton conductivity of iron oxide membranes. Hereunder I compare my results with other works reporting different surface areas and pore sizes to gather evidence to support this hypothesis.

Colomer and Zenzinger[60] studied hematite membranes having high sur-

face areas (130-240 m^2/g) but very small average pore size (2-4 nm) and conductivities of about 10^{-6}-10^{-7} S/cm at 30 % relative humidity (circa $p_{H_2O} = 0.01$ atm). Water uptake studies show that the surface of the material adsorbs or desorbs water depending on the relative humidity of the environment, and the conductivity of the materials decreases with decreasing relative humidity. The temperature dependence of the conductivity (measured at constant relative humidity) suggests that the protons migrate by Grotthuss mechanism. The low values of proton conductivity are probably due to changes in proton mobility and concentration due to structure of pore water,[66] which depends on the material and on the size of the pores. In very small pores it is likely that a higher fraction of the water in the pore is affected by the pore wall (the average pore in these materials has a diameter only about 10 times the diameter of a water molecule).

If instead the average pore size is two orders of magnitude larger (pore size > 200 nm), as in this work, at high humidities the pores are filled by physisorbed layers of water, but at lower humidities the physisorbed water is not retained by the structure and conductivity decreases dramatically. Also upon heating at 40 °C with $p_{H_2O} = 0.037$ atm the physisorbed water in the large pores is partially removed and thus the conductivity decreases 1-2 orders of magnitude. The values of conductivity are of the same order of magnitude as the ones presented by Colomer and Zenzinger.[60]

The sintered materials produced by Tsui *et al.*,[54] having an average pore size of 10-40 nm, exhibit instead much higher conductivities ($\approx 10^{-2}$ S/cm) than the materials with pores one order of magnitude bigger or smaller in size. The fact that the conductivity of the sintered material only slightly decreases in the range 30-100% relative humidity suggests that physisorbed water is immobilized in the mesopores of the material and retained by the material at least down to 30 % relative humidity.

So far I have shown how the overall conductivity values of my oxide materials (ferroxanes, maghemite, hematite) fit into the general picture of the data available in literature. However there are significant differences in conductivity among them, in particular in the very low humidity region (that has not been investigated by others so far) and in my opinion also these aspects can be explained taking into account the surface area and pore size data.

In general, the material sintered at 300 °C exhibits the highest conductivity at all humidity values, both at 25 °C and 40 °C. At $p_{H_2O} = 0.014$ atm and $p_{H_2O} = 0.037$ atm the green material has slightly lower conductivity values, and the material sintered at 500 °C has values one order of magnitude lower. At higher values of surface area correspond higher proton conductivities.

On top of that, there is a difference in pore size distribution among the materials. While all of them have average pore sizes above 200 nm the material sintered at 300 °C has a small amount of porosity in the 2-20

nm pore size range, and the green material has a slightly smaller amount. Porosity of this size is instead totally absent in the material sintered at 500 °C.

This small amount of mesoporosity could account for the very strong difference in conductivity among the three materials at $p_{H_2O} = 0.001$ atm, in particular the extremely low conductivity of the material sintered at 500 °C. While the water in macropores totally desorbs in these conditions, mesopores would be able to retain some of the water and thus ensure a conduction path for the protons. Tsui *et al.*[54] report that a chemisorbed layer of water gets formed on the oxide materials upon exposure to water vapor and that such a layer cannot be removed exposing the material to a dry atmosphere. My very low conductivity values at $p_{H_2O} = 0.001$ atm show that either the contribution of the chemisorbed layer to the proton conductivity is very low or that this layer is removed by continuously flushing the material with dry gas.

The same authors explain the lower conductivity of the green material compared to the sintered one suggesting that the carboxylic groups present at the surface of the particles (introduced by the reaction between lepidocrocite and acetic acid during the synthesis) hinder the mobility of the protons within the hydroxyl groups.[54,57] Since the carboxylic groups are removed upon sintering, their hindering effect would affect only the green material. However this mechanism would not explain the much lower conductivity of the material sintered at 500 °C. Moreover, the presence of carboxylic groups could at the same time hinder the proton conductivity but also improve the adsorption of water, because of the higher acidity of the carboxylic group compared to the hydroxyl group. In general, it is likely that the effect of the presence of carboxylic groups at the surface on the proton conductivity is dependent on the size of the pores where the adsorption takes place.

An additional conduction mechanism has been suggested for lepidocrocite by Guo *et al.*,[58] based on computational studies. The proton transfer would occur between OH groups on the side of the Fe octahedra sheets in the layered structure of lepidocrocite. Such a process is theoretically independent of the hydration conditions, therefore might be of interest in low humidity conditions. However it would take place only parallel to the layers forming the lepidocrocite structure, thus causing the protonic conductivity of the material to be highly anisotropic. My materials are fabricated pressing randomly oriented lepidocrocite particles, thus only a fraction of them is expected to be oriented perpendicular to the electrodes during the test. Any contribution of this process to the total proton conductivity would be extremely low.

2.5 Conclusions

Ferroxane powders are synthesized using a precipitation from acqueous solution, and a following reaction with acetic acid. The materials produced with these powders are electrochemically tested in the lowest humidity conditions reported so far in the literature.

Both green and sintered materials exhibit a strong dependence of conductivity on humidity, which I attribute to the presence of macropores (> 200 nm) that do not hinder water desorption. The analysis of presented data and the comparison with previous literature reports suggests that surface area and in particular pore size are the factors determining the proton conductivity of iron oxides materials. The very low conductivity values measured at $p_{H_2O} = 0.001$ atm suggest that either the chemisorbed water layer has a very low proton conductivity or it is removed by exposing the material to dry gas.

Heating up the material from room temperature to 40 °C causes a reduction of conductivity at high humidity values, likely due to the desorption of physisorbed water from the macropores.

The materials have relatively high conductivity (up to $7 \cdot 10^{-3}$ S/cm) and could be applied as proton conductor for room temperature, moderate humidity applications. Tailoring of the pore size to obtain mesoporosity is expected to improve the proton conductivity of the material at low humidities.

Chapter 3

Y-doped Si, Sn, Zr and Ce pyrophosphates

The ferroxanes-derived materials presented in Chapter 2 are not suitable for the present application because water is needed to have proton conductivity. Another class of potential intermediate-temperature proton conductors is pyrophosphates: the study of these materials is started with a conductivity and stability study of four different compositions.

Abstract

Four yttrium doped pyrophosphates with different host cations have been synthesized using different stoichiometry of phosphor to metal. The phase evolution and thermal stability have been characterized using powder XRD, thermal gravimetry and mass spectrometry. The identity of the host cation is found to affect the phosphor to metal ratio necessary to achieve single phase powders. The electrical conductivity has been investigated at a number of temperatures and varying partial pressures of H_2O, (ranging from $p_{H_2O} < 0.001$ atm to 0.20 atm) in reducing and oxidizing gas mixtures. The conductivity of $Si_{0.9}Y_{0.1}(P_2O_7)_{1-\delta}$, $Zr_{0.9}Y_{0.1}(P_2O_7)_{1-\delta}$ and $Ce_{0.9}Y_{0.1}(P_2O_7)_{1-\delta}$ is $5{\cdot}10^{-3}$, $1.2{\cdot}10^{-3}$ and $3{\cdot}10^{-2}$ S/cm, respectively, at 190 °C and $p_{H_2O} = 0.20$ atm. $Sn_{0.9}Y_{0.1}(P_2O_7)_{1-\delta}$ has a conductivity of $2{\cdot}10^{-3}$ S/cm at 150 °C. A long term degradation measurement (1100 hours at 155 °C) is conducted for $Sn_{0.9}Y_{0.1}(P_2O_7)_{1-\delta}$ and $Zr_{0.9}Y_{0.1}(P_2O_7)_{1-\delta}$ at alternating humidity. $Sn_{0.9}Y_{0.1}(P_2O_7)_{1-\delta}$ shows constant conductivity at $p_{H_2O} = 0.2$ atm while $Zr_{0.9}Y_{0.1}(P_2O_7)_{1-\delta}$ degrades with time.

3.1 Introduction

Fuel cells and electrolyzers operating at intermediate temperatures (200 - 400 °C) can potentially have several advantages over their high temperature

(600 - 1000 °C) and low temperature (< 100 °C) counterparts. Low temperature PEM cells are due to their low operation temperature limited to the use of precious metal catalysts. Fuel cells and electrolyzers operating at intermediate temperatures (200 - 400 °C) can potentially have increased catalytic activity with non-noble metal catalysts, enabling a decrease in material cost compared to low temperature cells.[2] High temperature solid oxide cells, operating at 600 - 1000 °C, often suffer from cation diffusion and formation of insulating layers at interfaces, coarsening of catalysts and rapid degradation of sealings and interconnects.

Operation at intermediate temperatures requires new proton conducting electrolyte materials. One group of intermediate temperature proton conductors that has attracted extensive interest over the last years are pyrophosphates, MeP_2O_7, where Me = tetravalent cation. A large number of pyrophosphates based on different tetravalent host cations and doped with trivalent or divalent cations have been synthesized and characterized,[67–70] with In- doped tin pyrophosphate being the most studied composition.[68,71] Nagao *et al.*[68] report a conductivity value of 0.2 S/cm for $Sn_{0.9}In_{0.1}P_2O_7$ at 200 °C in air ($p_{H_2O} \approx 0.0075$ atm).

Acceptor doping, i.e. doping with a lower valent cation, is often reported to increase the conductivity of pyrophosphates, but the conductivity mechanism is still not understood. Different mechanisms are proposed, but more data are needed in order to fully understand the conduction mechanisms.[72] Indium, aluminum, magnesium, yttrium, scandium and gallium are a few examples of acceptor dopants. Genzaki *et al.*[73] and Nagao *et al.*[68] report that doped SnP_2O_7 goes through a maximum in conductivity at a doping level of 10 mol % when doped with Mg and In, respectively, while Scott *et al.*[74] report that a doping level of 20 mol % gives the highest conductivity when SnP_2O_7 is doped with antimony. Ionic transference numbers above 0.8 are reported by several authors. For example Nagao *et al.*[68] report ionic transference numbers above 0.9 for SnP_2O_7 and Wang[75] measures the ionic transference number to be 0.95 in wet H_2 (for $Sn_{0.94}Sc_{0.06}P_2O_7$).

The phase composition is dependent on the choice of cation, synthesis method and thermal treatment history. For example CeP_2O_7 is reported to decompose already at 400-500 °C,[69,76] while SnP_2O_7 and ZrP_2O_7 are reported to be stable up to temperatures above 1000 °C.[77,78] There is a large discrepancy of reported conductivities, for example Nagao *et al.*[68,79] report a conductivity value of 0.2 S/cm for $Sn_{0.9}In_{0.1}P_2O_7$ whereas Einsla *et al.*[80] report $5.5 \cdot 10^{-3}$ S/cm for nominally the same compound, but prepared following a different synthesis procedure. Also, the phosphor to metal ratio has been shown to affect the conductivity greatly.[68,81] Studies by Wang *et al.*[81] and Nagao *et al.*[68] show that an over-stoichiometry of phosphor compared to the stoichiometric value (2) is beneficial from a conductivity point of view. Jin *et al.*[67] report that the conductivity is dependent on the choice of host cation in the order of $Zr^{4+} < Ge^{4+} < Si^{4+} < Ce^{4+} < Ti^{4+} <$

Sn^{4+}.

This study comprises an effort to clarify the influence of the host cation on the conductivity and phase composition. Four compounds doped with 10 mol % yttrium, namely $Si_{0.9}Y_{0.1}(P_2O_7)_{1-\delta}$, $Sn_{0.9}Y_{0.1}(P_2O_7)_{1-\delta}$, $Zr_{0.9}Y_{0.1}(P_2O_7)_{1-\delta}$ and $Ce_{0.9}Y_{0.1}(P_2O_7)_{1-\delta}$ are synthesized and carefully characterized with respect to phase evolution and conductivity. Yttrium is chosen as the dopant because it is three valent (3+) making it suitable as a dopant. Also, its size is in between the size of the host cations (cerium, zirconium, tin and silicon), increasing the probability of being incorporated into all four pyrophosphates.

3.2 Experimental

3.2.1 Synthesis

$Si_{0.9}Y_{0.1}(P_2O_7)_{1-\delta}$, $Sn_{0.9}Y_{0.1}(P_2O_7)_{1-\delta}$, $Zr_{0.9}Y_{0.1}(P_2O_7)_{1-\delta}$ and $Ce_{0.9}Y_{0.1}(P_2O_7)_{1-\delta}$, are synthesized by mixing the respective metal oxides: SiO_2 (99.5 %, Alfa Aesar), SnO_2 (99.9 %, Alfa Aesar), ZrO_2 (> 99 % Sigma Aldrich) and CeO_2 (99.9 %, Sigma Aldrich), the dopant Y_2O_3 (99.9 %, Johnson Matthey) and phosphoric acid (85 % H_3PO_4 in H_2O w/w, Sigma Aldrich). Oxides, dopant and H_3PO_4 are added in the molar ratio: 0.9:0.1:2.6 respectively. The mixed reactants are magnetically stirred and heated on a hot-plate (set temperature = 300 °C) until a high viscosity slurry is formed. The materials are then heat treated in a hot chamber (200 °C) over night, a small quantity of each powder is taken out and annealed at 380, 590, 790 °C for 6 h and 980 °C for 12 h. The as-synthesized powders (except $Si_{0.9}Y_{0.1}(P_2O_7)_{1-\delta}$) are then mixed with additional H_3PO_4 giving a phosphor to metal ratio (P/Metal ratio) of 3.1, also 10 - 20 ml H_2O is added to the mixtures before they are additionally stirred on a hot plate (200 - 300 °C for 0.5-2.5 h) and further heat treated at 200 °C (overnight). The prepared materials are then annealed at 380, 590, 790 and 980 °C in air for 3h at each temperature using a ramp rate of 180 °C/hour. All annealing steps are performed with the powders placed in alumina crucibles with an alumina lid placed on top. The four materials from the initial synthesis are abbreviated as: SiY10, SnY10, ZrY10 and CeY10 and the re-synthesized batches are abbreviated as SnY10+P, ZrY10+P and CeY10+P.

3.2.2 Morphology, crystal structure and thermal stability

The crystal structure of the synthesized and annealed materials is analyzed using powder X-Ray diffraction, PXRD (Bruker D8 Advance diffractometer with Cu Kα radiation and a PSD LynxEye detector). All X-Ray diffractograms are recorded between 10 - 80° 2θ with a step size of 0.02°. EVA 13.0.0.3 is used for analysis of X-Ray diffractograms.

Thermal gravimetric analysis (Netzsch STA 409CD, TGA) and gas analysis measurements (mass spectrometry, Omnistar GSD301) on the outlet gas stream are performed on all materials. The temperature is increased stepwise (using a ramp rate of 2 °C/min) from room temperature up to 900 °C, including hold times at 100, 150, 200, 250, 300, 500, 700 and 900 °C. The hold time is 60 minutes at each temperature plateau except at 150 °C where the hold time is 300 minutes including atmosphere changes: air to N_2, to CO_2, to 9% H_2 in N_2 and back to air. Approximately 100 mg of each material is used for the measurements.

3.2.3 Conductivity

Disc shaped symmetrical cells, i.e. cells with two identical electrodes, are prepared by pressing ground powder of each compound using a uniaxial press (300 MPa in pressure), the mould used has a diameter of 8 mm. Commercially available PEM CCB (catalyst coated backing) electrodes from IRD A/S with 0.56 mg Pt cm^{-2} are used as electrodes. These Pt- carbon papers are placed on both sides of the electrolyte. One annealing temperature of each material is tested, namely the one that gives the least amount of secondary phases: SiY10 annealed at 980 °C, SnY10+P annealed at 590 °C, ZrY10+P annealed at 980 °C and CeY10+P annealed at 380 °C. The electrical conductivity of the materials is measured using a single atmosphere setup. The setup is constructed so that diluted H_2 in N_2 (maximum 9% H_2), N_2, air and O_2 and various humidities (< 0.001 - 0.2 atm H_2O) can be used and mixed at temperatures ranging from room temperature up to 850 °C. Four samples can be tested in each test. A Solartron 1260 frequency response analyzer and a Gamry Instruments, Reference 600 Potentiostat/ Galvanostat/ ZRA are used for electrochemical impedance spectroscopy (EIS) measurements. EIS measurements are carried out using an AC signal with an amplitude of 20 mV over a frequency range of 1 MHz down to 1 Hz. Data analysis is carried out using ZSimpWin 3.21 and Zview 3.0a. Three electrochemical tests are performed by varying the temperature, humidity, and gas composition. The first two tests are performance tests. In these tests the temperature, humidity and gas composition are changed several times. The third test is a long term stability test conducted at a constant temperature (155 °C). The humidity is changed three times between dry ($p_{H_2O} < 0.001$ atm) and humid ($p_{H_2O} = 0.20$ atm) conditions, respectively.

3.3 Results

3.3.1 Crystal structure and thermal stability

3.3.1.1 X-Ray diffraction measurements

X-Ray diffraction measurements carried out on SiY10 after synthesis and annealing at 380 °C show a complex mix of several crystal structures. Annealing at 790 °C and 980 °C results in a three phase system where all three phases are SiP_2O_7, but with different crystal structures, Table 3.1. SiY10 is the only material showing only the desired phase composition after the first synthesis, using a P/Metal ratio of 2.6.

ZrY10 shows residual ZrO_2 after all annealing temperatures, the intensity of the oxide peaks decreases for ZrY10+P compared to ZrY10, i.e. after addition of phosphoric acid (P/Metal ratio = 3.1), but does not disappear completely. ZrY10+P annealed at 980 °C shows the least amount of residual ZrO_2.

SnY10 shows peaks of oxide, SnO_2, without any significant difference in oxide content for the two samples, SnY10 and SnY10+P, after heat treatment at the higher temperatures (790 and 980 °C). SnY10 shows a decrease in oxide content for higher annealing temperature while the oxide content for SnY10+P decreases when it is annealed at 590 °C compared to 380 °C and stays almost constant after annealing at temperatures higher than 590 °C. The main phase is SnP_2O_7 after annealing at 590 °C, but there is still a significant amount of SnO_2 left in the sample.

The cerium pyrophosphates show a more severe decomposition upon high temperature treatment than the other materials. CeY10 shows a significant amount of residual CeO_2 in the as-synthesized powder, but the CeO_2 content decreases after annealing at 380 °C. Annealing at higher temperatures results in a stepwise decomposition of the compound resulting in a two phase system consisting of $Ce(PO_3)_3$ and $CePO_4$ as a secondary phase after annealing at 980 °C. CeY10+P, P/Metal ratio = 3.1, shows less residual oxides compared to CeY10 after annealing at 380 °C giving an almost phase pure CeP_2O_7 structure. Also, CeY10+P decomposes into $Ce(PO_3)_3$ as the main phase and a small amount of $CePO_4$ after annealing at 980 °C.

Table 3.1 summarizes the phase evolution with respect to crystal structures and their corresponding space groups for SiY10, SnY10+P, ZrY10+P and CeY10+P, the dominating phase is the first one named in each cell and compounds with a maximum peak intensity lower than 10% of the dominating phase are put in parenthesis. Figure 3.1 shows one X-Ray diffractogram for each compound, namely; SiY10 annealed at 980 °C, SnY10+P annealed at 590 °C, ZrY10+P annealed at 980 °C and CeY10+P annealed at 380 °C. CeY10+P (annealed at 380 °C) and SnY10+P (annealed at 590 °C) show two and one unknown peak, respectively. The presented diffractograms belong to the sample that show the least amount of secondary phases and are

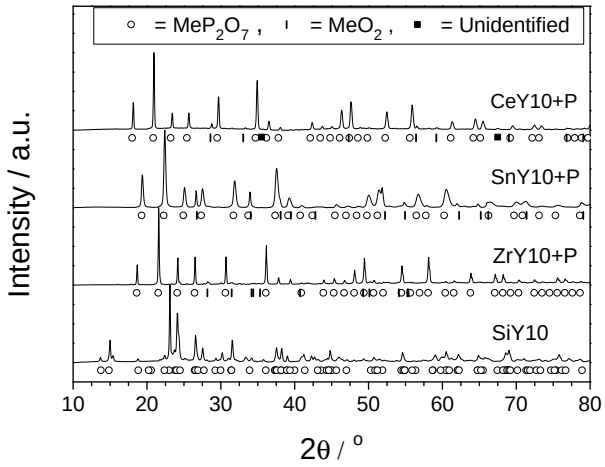

Figure 3.1: XRD patterns for CeY10+P (annealed at 380 °C), SnY10+P (annealed at 590 °C), ZrY10+P (annealed at 980 °C) and SiY10 (annealed at 980 °C). The step size is 0.02°. Open circles = respective MeP_2O_7, standing bars = respective metal oxide (MeO_2), black squares = unknown peaks.

later used for conductivity measurements (presented in Section 3.3.2).

Table 3.1: Crystal structures and space groups retrieved from X-Ray diffraction measurements after annealing at different temperatures. The compound that has the highest intensity is the one mentioned first in each cell and compounds showing only a small contribution are written in a parenthesis. H = Hexagonal, C = Cubic, M = Monoclinic, O = Orthorhombic and T = Tetragonal unit cells.

Material	Annealing temperature			
	380 °C	**590 °C**	**790 °C**	**980 °C**
$Si_{0.9}Y_{0.1}(P_2O_7)_{1-\delta}$ SiY10	SiP_2O_7 (H: $P6_3$, M: $P2_1/n$, C: Pa-3) + residuals from as - synthesized	SiP_2O_7 (H: $P6_3$, M: $P2_1/n$, C: Pa-3) + residuals from as - synthesized	SiP_2O_7 (H: $P6_3$, M: $P2_1/n$, C: Pa-3)	SiP_2O_7 (H: $P6_3$, M: $P2_1/n$, C: Pa-3)
$Sn_{0.9}Y_{0.1}(P_2O_7)_{1-\delta}$ SnY10+P	SnP_2O_7 (C: Pa-3) SnO_2 (T: $P4_2/mnm$)	SnP_2O_7 (C: Pa-3) SnO_2 (T: $P4_2/mnm$)	SnP_2O_7 (C: Pa-3) SnO_2 (T: $P4_2/mnm$)	SnP_2O_7 (C: Pa-3) SnO_2 (T: $P4_2/mnm$)
$Zr_{0.9}Y_{0.1}(P_2O_7)_{1-\delta}$ ZrY10+P	ZrP_2O_7 (C: Pa-3) ZrO_2 (M: $P2_1/a$) $ZrO(PO_4)_2$ (O: Cmca)	ZrP_2O_7 (C: Pa-3) ZrO_2 (M: $P2_1/a$)	ZrP_2O_7 (C: Pa-3) ZrO_2 (M: $P2_1/a$)	ZrP_2O_7 (C: Pa-3) (ZrO_2 (M: $P2_1/a$))
$Ce_{0.9}Y_{0.1}(P_2O_7)_{1-\delta}$ CeY10+P	CeP_2O_7 (C: Pa-3) (CeO_2 (C: Fm-3m))	CeP_2O_7 (C: Pa-3) $Ce(PO_3)_4$ (O: Pbcn) (CeO_2 (C: Fm-3m))	CeP_2O_7 (C: Pa-3) $Ce(PO_3)_4$ (O: Pbcn) (CeO_2 (C: Fm-3m))	$Ce(PO_3)_3$ (O: $C222_1$) ($CePO_4$ (M: $P2_1/n$))

3.3.1.2 Thermogravimetry and mass spectrometry measurements

Weight loss curves retrieved by thermogravimetric measurements, TGA, of SiY10, SnY10+P, ZrY10+P and CeY10+P are presented in Figure 3.2. Weight loss occurs in several steps for all materials as also the temperature is increased in steps. All materials reach a stable plateau at 900 °C and no changes in weight are recorded during cooling of the samples. SiY10, SnY10+P and ZrY10+P show similar trends in their weight loss curves. Namely, weight losses are observed at all temperature steps, but with different relative amounts. A difference in relative weight loss is expected due to their difference in molecular weight as well as their difference in hydrophilicity. SiY10, ZrY10+P, SnY10+P and to some extent CeY10+P absorb water from the surrounding air when left outside the gas tight containers used for storage. CeY10+P shows two major weight losses in the TG-measurement; these occur between 350 - 450 °C and 800 - 900 °C and correspond to 2.8 and 6.4 wt % respectively. The total weight loss for CeY10+P relative to the starting mass is measured to be 10.9 wt % and 43.5, 26.2 and 11.2 wt % for SiY10, ZrY10+P and SnY10+P, respectively.

Mass spectrometric measurements of the outlet gas flow from the TG measurement record water losses, molecular weight of 18.016 u, from all materials up to approximately 500 °C. The large mass loss that occurs from 25 - 150 °C (the initial 180 minutes of the experiment) is attributed to loss of water and used as a calibration for the MS. Mass losses occurring at temperatures above 150 °C can then be correlated to the results from the MS. Figure 3.3 presents a comparison between the measured mass loss (TG) and the H_2O signal from the MS. Mass losses occurring up to 500 °C can be attributed to loss of water and mass losses at temperatures above 500 °C are due to loss of other compounds.

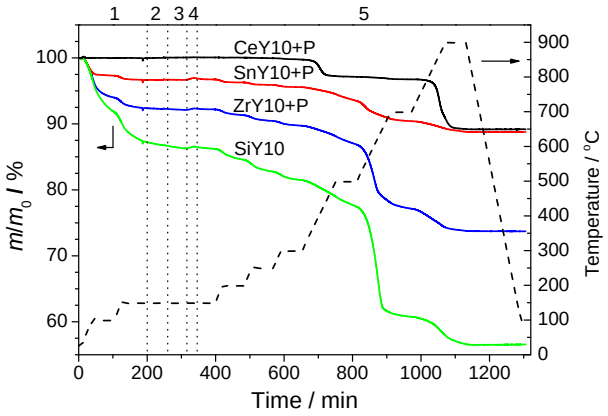

Figure 3.2: TGA measurements performed on the four different materials. Samples: a) CeY10+P, b) SnY10+P, c) ZrY10+P and d) SiY10. Atmospheres: 1) Air, 2) CO_2, 3) 9% H_2 in N_2, 4) N_2 and 5) Air. Dashed line: temperature profile.

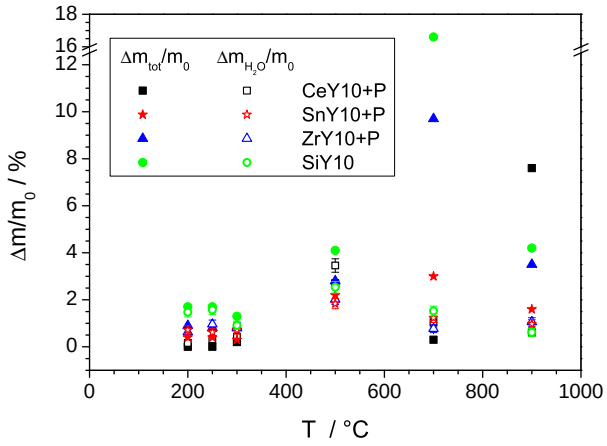

Figure 3.3: Total relative mass loss and losses associated with dehydration for CeY10+P, SnY10+P, ZrY10+P and SiY10. Closed markers = total relative mass loss at each temperature step and open markers = recorded relative mass loss of water at each temperature step.

3.3.2 Electrical conductivity

The conductivity is strongly dependent on the humidity for all four materials; Figure 3.4 compares the conductivity in dry and wet gas (9% H_2 in N_2). The conductivity increases 3-6 orders of magnitude when the surrounding atmosphere is changed from dry ($p_{H_2O} < 0.001$ atm) to wet ($p_{H_2O} = 0.20$ atm). Data presented in Figure 3.4 are not complete for SnY10+P (annealed at 590 °C) since this material is measured in a different test, and the data cannot be directly compared to the data for the other three materials, which are measured in the same experiment and under identical circumstances. SiY10 (annealed at 980 °C), ZrY10+P (annealed at 980 °C) and CeY10+P (annealed at 380 °C) all show a conductivity maximum around 190 °C when measured in 20 % H_2O and 7% H_2 balanced with N_2. Their conductivity maximum is $5{\cdot}10^{-3}$, $1.2{\cdot}10^{-3}$ and $30{\cdot}10^{-3}$ S/cm, respectively.

Figure 3.4 also shows how the conductivity of SiY10, ZrY10+P and CeY10+P changes during the first thermal cycle (100 - 300 - 100 °C) at $p_{H_2O} = 0.20$ atm, compare open single markers with the initial results performed at 105 °C. The thermal cycle is 24 hours in total. The conductivity of SiY10 is increased by a factor of 14 during the first thermal cycle, while ZrY10+P shows the same conductivity and CeY10+P shows a minor decrease in conductivity. This test includes a total of 6 thermal cycles (100 - 300 - 100 °C), 3 humidity cycles ($p_{H_2O} < 0.001$ - 0.20 - < 0.001 atm) and several redox cycles (9% H_2 in N_2, air and N_2). The conductivity for CeY10+P, SiY10 and ZrY10+P decreases by 1, 2 and 1 order of magnitude, respectively, comparing the initial with the final conductivities measured at

105 °C in 20% H_2O, 7% H_2 balanced with N_2.

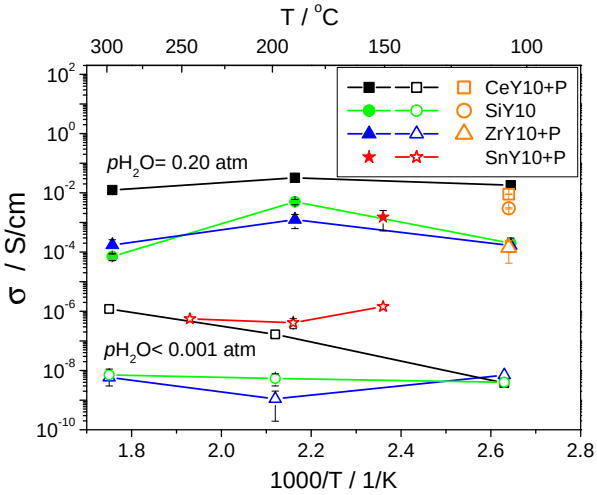

Figure 3.4: Arrhenius plot showing the conductivity of SnY10+P (stars), CeY10+P (squares), SiY10 (circles) and ZrY10+P (triangles) at $p_{H_2O} < 0.001$ atm (open markers) and $p_{H_2O} = 0.20$ atm (closed markers, first measurement cycle). Gas: 9% H_2 in N_2. Open orange markers correspond to the measured conductivities when the temperature is decreased back to starting conditions (T = 105 °C, $p_{H_2O} = 0.20$ atm).

The p_{H_2O} and p_{O_2} dependency for SnY10+P and CeY10+P is further examined. Figure 3.5 shows the dependency on p_{H_2O}, including p_{H_2O} values from approximately 0.001 atm up to 0.20 atm of steam in air. CeY10+P is seen to depend on the humidity following $\sigma \propto p_{H_2O}^{1.02}$ while the p_{H_2O} dependency for SnY10+P follows $\sigma \propto p_{H_2O}^{0.69}$. The conductivity dependence on p_{O_2} is measured for CeY10+P and SnY10+P in three different partial pressures of oxygen, ranging from 10^{-53} (theoretically calculated p_{O_2} for a 9% H_2 in N_2 ($p_{H_2O} = 0.001$ atm)) to 0.21 atm, see Figure 3.6. The conductivity of SnY10+P changes from $1.4 \cdot 10^{-6}$ to $2 \cdot 10^{-6}$ and up to $1.2 \cdot 10^{-5}$ S/cm when the p_{O_2} is changed from 10^{-53} to 10^{-4} and further up to 0.21 atm for measurements carried out in dry gases ($p_{H_2O} < 0.001$ atm). It should be noted that the true p_{O_2} is certainly not as low as the theoretical value of 10^{-53} atm. Anyhow, a deviation from the theoretical value will not drastically affect the observed trends, shown in Figure 3.6. The corresponding values for CeY10+P are $12 \cdot 10^{-6}$ to $11 \cdot 10^{-6}$ and further up to $15.5 \cdot 10^{-6}$ S/cm. No p_{O_2} dependence is seen for SnY10+P when measurements are performed in humidified gases, the conductivity is $1.5 \cdot 10^{-3}$, $1.2 \cdot 10^{-3}$ and $1.3 \cdot 10^{-3}$ S/cm at the three gas mixtures after humidification to 0.20 atm of H_2O.

A long term conductivity test is performed for SnY10+P and ZrY10+P to study the long term stability under relevant conditions. The test is carried out at 155 ± 1 °C, the atmosphere is changed between $p_{H_2O} = 0.001$ atm

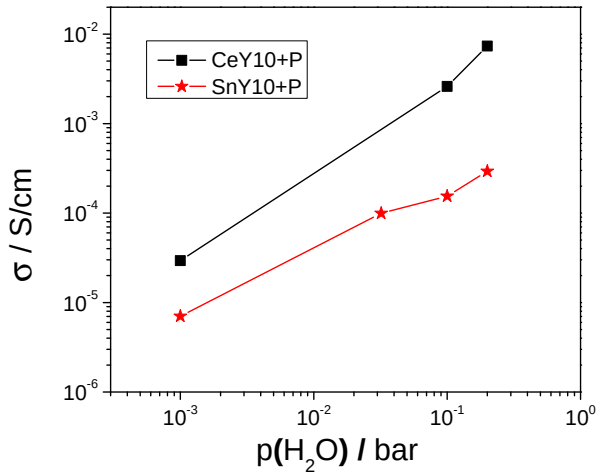

Figure 3.5: Conductivity of CeY10+P (squares) and SnY10+P (stars) as a function of p_{H_2O}. Measurements are performed in air (with different p_{H_2O}) at a temperature of 190 °C.

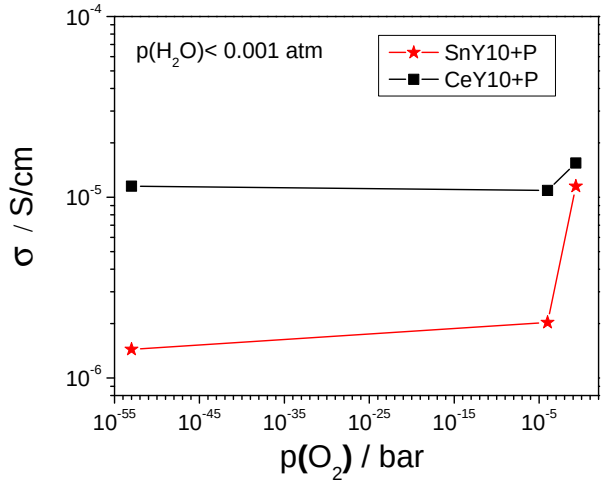

Figure 3.6: Conductivity of CeY10+P (squares) and SnY10+P (stars) as a function of p_{O_2}. Measurements are performed at 150 °C and with a $p_{H_2O} < 0.001$ atm. (Be aware that the value of 10^{-53} atm is the theoretical value for 9% H_2 + N_2 ($p_{H_2O} = 0.001$ atm), and the true value is most likely several orders of magnitude higher)

and p_{H_2O} = 0.2 atm in nitrogen, giving three hydration- dehydration cycles, see Figure 3.7. The conductivity of ZrY10+P can only be measured at the higher humidity, and the conductivity is $3{\cdot}10^{-5}$ - $4{\cdot}10^{-5}$ S/cm at the start of all three hydration cycles (p_{H_2O} = 0.20 atm), but is decreasing with time in the second and third cycle. The conductivity is stabilized after a drop of 1 order of magnitude occurring in the third cycle (between 790–1040 h from start). The conductivity of SnY10+P is stable for all three hydration cycles (p_{H_2O} = 0.20 atm), $1.8{\cdot}10^{-4}$ - $2{\cdot}10^{-4}$ S/cm, as well as under the long dehydration cycle carried out 340–790 hours from start, where the conductivity is $4{\cdot}10^{-6}$ - $6{\cdot}10^{-6}$ S/cm.

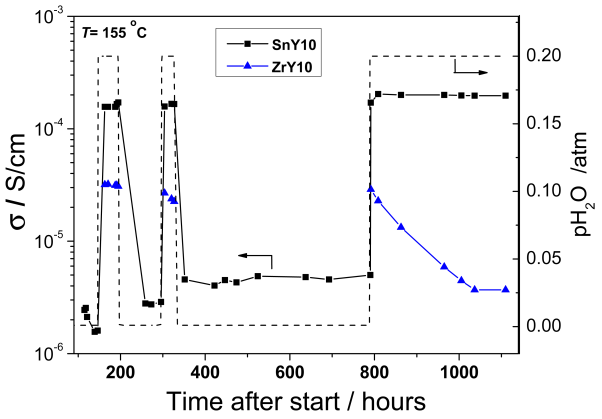

Figure 3.7: Conductivity versus time for SnY10+P (squares) and ZrY10+P (triangles). The p_{H_2O} is alternated between < 0.001 atm and 0.20 atm in N_2 and the temperature is kept at 155 °C.

3.3.3 Post mortem phase analysis

The crystal structure for each material is investigated after electrochemical testing and a detailed comparison of their crystal structures before and after these tests is presented in Table 3.2. Figure 3.8 presents post mortem X-Ray diffractograms for SiY10 and CeY10+P after the performance test and for SnY10+P and ZrY10+P after the long term stability test. SiY10 shows a clear amorphous background as well as crystalline peaks from its pyrophosphate structures, but most peaks can not be indexed. No phase changes are observed for ZrY10+P and SnY10+P after the performance or the long term test, see Table 3.2 and Figure 3.8. CeY10+P shows a multiphase composition after the performance test, containing $CePO_4$, $Ce(PO_3)_4$, CeP_2O_7 and a number of peaks not possible to index to any known compounds, see Table 3.2.

Table 3.2: Composition, crystal structures and space groups for each material retrieved from X-Ray diffraction measurements before and after electrochemical testing. The compound that has the highest intensity is the one denoted as the first phase at each material and annealing temperature. H = Hexagonal, C = Cubic, M = Monoclinic and T = Tetragonal unit cells

Material	Before test	After performance test	After long term stability test
$Si_{0.9}Y_{0.1}(P_2O_7)_{1-\delta}$ SiY10	SiP_2O_7 (H: P63, M: $P2_1/n$, C: Pa-3)	Amorphous background with residual pyrophosphate peaks and unidentified peaks Pt (C: Fm-3m)	Not included in this test
$Sn_{0.9}Y_{0.1}(P_2O_7)_{1-\delta}$ SnY10+P	SnP_2O_7 (C: Pa-3) SnO_2 (T: $P4_2/mnm$)	SnP_2O_7 (C: Pa-3) SnO_2 ($P2_1/a$)	SnP_2O_7 (C: Pa-3) SnO_2 (T: $P4_2/mnm$)
$Zr_{0.9}Y_{0.1}(P_2O_7)_{1-\delta}$ ZrY10+P	ZrP_2O_7 (C: Pa-3) ZrO_2 (M: $P2_1/a$)	ZrP_2O_7 (C: Pa-3) ZrO_2 (M: $P2_1/a$)	ZrP_2O_7 (C: Pa-3) ZrO_2 (M: $P2_1/a$)
$Ce_{0.9}Y_{0.1}(P_2O_7)_{1-\delta}$ CeY10+P	CeP_2O_7 (C: Pa-3) CeO_2 (C: Fm-3m)	$CePO_4$ (M:$P2_1/n$) $Ce(PO_3)_4$ (O: Pbcn) $Ce(PO_3)_3$ (O: $C222_1$) + unidentified peaks	Not included in this test

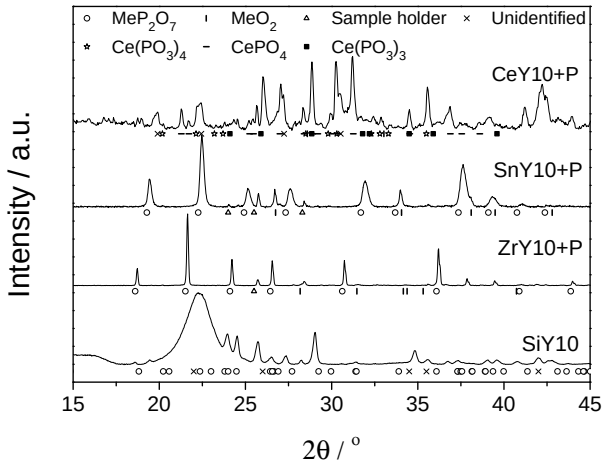

Figure 3.8: XRD patterns for a) SiY10 after performance test, b) SnY10+P and c) ZrY10+P after long term test and d) CeY10+P, measured after the initial performance test.

3.4 Discussion

3.4.1 Thermal stability

The crystal structure and phase purity are examined using PXRD on as-synthesized samples and samples annealed at different temperatures. SiY10 consists of three crystal structures; hexagonal-, monoclinic-, and cubic SiP_2O_7, after annealing at 790 and 980 °C, see Table 3.1 and Figure 3.1. This is in good agreement with earlier results from Makart[82] who also shows a three phase system of SiP_2O_7. Poojary *et al.*[83] found that hexagonal SiP_2O_7 is stable up to temperatures between 900- 1000 °C using high temperature PXRD. The materials prepared in this study also exhibit a high thermal stability and all three crystal structures are stable up to the maximum treatment temperature (980 °C). Anyhow, the SiY10 sample is seen to decompose into an amorphous and a crystalline composite during the electrochemical test which is conducted at much lower temperatures than the ones used for annealing. Some crystalline peaks match the initial pyrophosphate compounds, but most peaks are unknown and it is not possible to index them with any relevant compound in the used database. Low temperature decomposition of SiP_2O_7 has not been reported elsewhere and the reason remains unclear. Matsui *et al.*[84,85] report X-Ray diffractograms before and after heat treatment to 220 °C for a CsH_2PO_4:SiP_2O_7 composite electrolyte without any apparent decomposition of SiP_2O_7.

Tin pyrophosphate synthesized with a P/Metal ratio of 2.6 and 3.1 contains similar amounts of residual SnO_2 after annealing at 590 °C or above.

SnP_2O_7 is found to be the main phase having a cubic crystal structure, Figure 3.1, just as reported by Gover *et al.*[86] Lan *et al.*[78] report a more complex crystal structure of Sc- doped SnP_2O_7, namely a 3 3 3 super lattice of either cubic or orthorhombic nature. Gover *et al.*[86] report SnP_2O_7 to be stable up to 950 °C, which is the highest temperature in their study. Lan *et al.*[78] report that Sc- doped SnP_2O_7 starts to form a secondary phase of $ScPO_4$ when heated at 1100 °C or above. These results are in agreement with findings in this study where $Sn_{0.9}Y_{0.1}(P_2O_7)_{1-\delta}$ is stable at the maximum annealing temperature, 980 °C. No phase change is observed for SnY10+P after either of the two conductivity tests.

X-Ray diffraction measurements of ZrY10 synthesized with a P/Metal ratio of 2.6 show more pronounced residual peaks of ZrO_2 compared to ZrY10+P synthesized with higher P:Metal ratio (3.1:1). XRD measurements show that the formed ZrP_2O_7 phase has a cubic structure, in good agreement with Teranishi *et al.*[87] who form a cubic $Zr_{1-x}Y_xP_2O_7$ by reacting yttria stabilized zirconia with phosphoric acid. Also, Nalini *et al.*[77] show cubic structures for both un-doped ZrP_2O_7 and ZrP_2O_7 doped with 2 mol % of La, Sc or Y. Nalini *et al.* report that ZrP_2O_7 synthesized with a 2:1 stoichiometry of phosphor and zirconium is stable up 1100 °C after which it decomposes into $Zr_3(PO_4)_4$ and $Zr_2O(PO_4)_2$ by loss of P_2O_5 when treated at higher temperatures. This study showed that ZrY10 and ZrY10+P are at least stable up to the maximum treatment temperature, i.e. 980 °C, see Table 3.1. ZrY10+P does not show any phase changes after any of the two conductivity tests, just like SnY10+P, see Table 3.2.

The Ce- pyrophosphates show, just as the zirconium samples, a decrease in residual oxides when the P/Metal ratio is increased from 2.6 to 3.1. CeY10+P shows an almost single phase cubic structure, after annealing at 380 °C, see Figure 3.1. It is therefore fair to assume that addition of extra phosphoric acid makes it possible for the reaction to proceed towards full conversion of the starting oxides into pyrophosphate. Treatment at higher temperatures results in a partial decomposition into $Ce(PO_3)_4$ after treatment at 590 and 790 °C, see Reaction 3.1, and into $Ce(PO_3)_3$ and $CePO_4$ after treatment at 980 °C. Several studies report that Ce- pyrophosphates decompose at relatively low temperature.[69,76,88] These studies describe formation of the same decomposition products as in this study, but discrepancies are found in onset temperatures and decomposition mechanisms. The reason for the reported differences is probably related to differences in the synthesis procedure, P/Metal ratios used during synthesis and the thermal treatment history of the materials. CeY10+P shows an amorphous background and $CePO_4$, $Ce(PO_3)_4$ and $Ce(PO_3)_3$ phases after the conductivity test. The reason for the decomposition of these materials is unknown but the amorphous background can be an effect of the samples hygroscopic nature, giving rise to absorption of H_2O from the surrounding air. As mentioned above, $CePO_4$ is a decomposition product of CeP_2O_7 that has been seen in

several studies,[76,89] including this. Nevertheless, decomposition of CeP_2O_7 has not been reported to occur at these low temperatures in previous studies.

SiY10, SnY10+P and ZrY10+P all show a hygroscopic nature when left in ambient air. This makes it fair to attribute the initial weight loss, seen in Figure 3.2, to evaporation of absorbed water. The loss of water occurring between 150 - 500 °C can also be attributed to absorbed water as well as water formed by decomposition of excess phosphoric acid. Phosphoric acid is known to decompose, as the temperature exceeds 158 °C, into $H_4P_2O_7$, HPO_3 and P_2O_5, with all steps having H_2O as one of the products. The weight loss occurring at temperatures above 500 °C is not related to loss of water and is therefore attributed to loss of phosphor oxides. The weight loss of CeY10+P occurring between 300 - 400 °C can be explained by Reaction 3.1:

$$Ce_{0.9}Y_{0.1}P_2O_7 + 2H_3PO_4 \rightarrow Ce_{0.9}Y_{0.1}(PO_3)_4 + 3H_2O \qquad (3.1)$$

Reaction 3.1 is supported by the earlier discussed XRD results and would result in a total weight loss of 10.7 wt % if all pyrophosphate reacts with H_3PO_4 forming a tetra phosphite structure, but the stoichiometry of H_3PO_4 to metal (Ce + Y) used for the synthesis of CeY10+P allows for a maximum theoretical weight loss of 2.9 wt%. This correlates well with the measured weight loss of 2.8 wt%, see Figure 3.2. The $Ce_{0.9}Y_{0.1}(PO_3)_3$ and $Ce_{0.9}Y_{0.1}PO_4$ that is found to be formed after annealing at temperatures above 790 °C, Table 3.1, can be formed by evaporation of phosphorous pentoxide, P_2O_5, from $Ce_{0.9}Y_{0.1}(PO_3)_4$ and $Ce_{0.9}Y_{0.1}(PO_3)_3$, respectively. More detailed results on the thermal stability and phase evolution of CeY10+P have been reported by Chatzichristodoulou *et al.*[90]

3.4.2 Electrical conductivity

SiY10, ZrY10+P and CeY10+P reach conductivity values of $5{\cdot}10^{-3}$, $1.2{\cdot}10^{-3}$ and $30{\cdot}10^{-3}$ S/cm at 190 °C in 20% H_2O and 7% H_2 balanced with nitrogen (Figure 3.4). All three samples exhibit a maximum conductivity at 190 °C when measured at $p_{H_2O} = 0.2$ atm, this phenomenon is in good agreement with studies performed by Nagao *et al.*[68] and Shirai *et al.*[91] Values reported in this study are well comparable with the best conductivities reported in earlier studies using the same cations but with different or no dopants. Matsui *et al.* report that un-doped SiP_2O_7 has a conductivity of a few mS/cm at 200 °C when measured in 30% H_2O and air.[85] ZrP_2O_7 compounds have been reported to have conductivities of approximately 10^{-3} S/cm at 130 °C,[91] and $1.5{\cdot}10^{-2}$ S/cm at 100 - 200 °C when the pyrophosphate is covered by a phosphor rich shell,[92] but also lower values, in the order of 10^{-6} S/cm, have been reported.[93] Both Le *et al.*[76] and Sun *et al.*[69] have reported that the conductivity of CeP_2O_7 is in the same range as in this study. Nagao *et al.*[68] have reported that In-doped SnP_2O_7 reaches a conductivity of 0.2

S/cm at 200 °C measured in air with 0.75% H_2O. The conductivity for the SnY10+P tested in this study is more than two orders of magnitude lower than the values reported by Nagao *et al.*[68] The large discrepancy of reported conductivities is most probably, as mentioned earlier in this discussion, due to differences in the synthesis method, phosphor content and thermal history of the samples.

The conductivity of CeY10+P and SnY10+P is measured under several different humidities and it shows almost linear p_{H_2O} dependence, Figure 3.5. Many studies have shown that the pyrophosphates have a higher conductivity in humidified atmospheres, but only Nalini *et al.*[77] have performed measurements in a wide range of p_{H_2O}. That study presents p_{H_2O} dependencies of 1/3 which is significantly lower than values found in this study. One large difference in the studies is that Nalini *et al.* have prepared stoichiometric pyrophosphates while this study is performed on samples with an over-stoichiometry of phosphoric acid. Phosphoric acid is known to be hydrophilic and that might increase the sensitivity towards water partial pressure. The CeY10+P sample, sintered at 380 °C, shows a stronger p_{H_2O} dependency than SnY10+P, sintered at 590 °C. This result is in good agreement with the discussion that the phosphor content affects the p_{H_2O} dependency. The P/Metal ratio is most probably lower in SnY10+P than CeY10+P, due to their different thermal history. There are several reports showing that pyrophosphates tend to form a continuous phosphor rich phase at the surface of the pyrophosphate particles.[92,94] For example Park *et al.*[94] report that tin pyrophosphate synthesized below 800 °C has an outer shell of a phosphor rich phase. Also, Shirai *et al.*[92] report of a highly conducting shell for $0.9TiO_2{\cdot}0.05In_2O_3{\cdot}1.3P_2O_5$ samples sintered at 500 - 600 °C. CeY10+P and SnY10+P are sintered at temperatures below 600 °C and it is therefore fair to believe that their relatively high conductivities originate from such a core-shell structure giving a high conducting phase in the grain boundaries.

The conductivity of SnY10+P increases as the p_{O_2} is increased in dry atmosphere, see Figure 3.6, but no conductivity dependence on p_{O_2} is seen at high p_{H_2O}; this in turn indicates that the SnY10+P sample exhibits *p*-type conductivity at high partial pressures of oxygen. Also, Nagao *et al.*[68] report that the conductivity of SnP_2O_7 is dependent on p_{O_2} and show that the conductivity increases as p_{O_2} is increased from 0.1 to 1.0 atm for gases having a low p_{H_2O} (p_{H_2O} = 0.0008 atm). They also show that the conductivity is independent of p_{O_2} as the p_{H_2O} is increased to 0.12 atm.[68] These results are in good agreement with the results presented for SnY10+P in this study. CeY10+P does not exhibit the same clear increase in conductivity, but the small increase that can be seen in Figure 3.6 can possibly indicate a small electronic contribution to its total conductivity.

The conductivity of SnY10+P increases slightly in the first short humidity cycles but is then stable throughout the rest of the long term stability

test, see Figure 3.7. ZrY10+P shows poor long term stability, the conductivity decreases one order of magnitude in the last high humidity cycle before it starts to stabilize towards the end of the measurement. The reason for this decrease in conductivity is unclear, especially since the crystal structure is unchanged before and after the test (compare: Table 3.1 and 3.2 as well as Figure 3.1 and 3.8).

3.5 Conclusions and outlook

The crystal structure and phase purity of $Si_{0.9}Y_{0.1}(P_2O_7)_{1-\delta}$, $Sn_{0.9}Y_{0.1}(P_2O_7)_{1-\delta}$, $Zr_{0.9}Y_{0.1}(P_2O_7)_{1-\delta}$ and $Ce_{0.9}Y_{0.1}(P_2O_7)_{1-\delta}$ have been investigated by varying the annealing temperature and the phosphor to metal ratio (P/Metal ratio of 2.6 and 3.1). SiY10 is found to be completely formed into three pyrophosphate structures after heat treatment at 790 °C for 6 h, whereas SnY10, ZrY10 and CeY10 synthesized with a P/Metal ratio of 2.6 show residual starting chemicals (oxides) in the material regardless of the sintering temperature. The amount of residual oxides decreases for ZrY10+P and CeY10+P after addition of extra phosphoric acid, while it remains constant for the tin pyrophosphate. CeY10+P shows a lower thermal stability than the other three materials. Phases and stability data obtained in this study are in good agreement with what has been found in earlier studies.

CeY10+P shows promising initial conductivities, but also poor phase stability which makes it hard at this point to evaluate possible applications and industrial relevance of the material. There is a need for long term conductivity studies in order to measure how the phase change affects its conductivity. SnY10+P is a material worth investigating further, since it exhibits stable conductivity, seen in an 1100 hours long conductivity test, relatively high conductivity ($2{\cdot}10^{-3}$ S/cm at 150 °C) and high thermal stability. A drawback with SnY10+P is that *p*-type conductivity is induced when the surrounding atmosphere is oxidizing (i.e. air). The relatively high conductivity of SnY10+P and CeY10+P is likely to originate from the formation of a phosphor rich phase in the grain boundaries. $Si_{0.9}Y_{0.1}(P_2O_7)_{1-\delta}$ decomposes during conductivity measurements and $Zr_{0.9}Y_{0.1}(P_2O_7)_{1-\delta}$ has a poor stability in terms of conductivity even though it keeps the same crystal structure throughout the conductivity test.

This study clearly shows that the thermal stability of pyrophosphates is largely affected by the host cations. This forms a requirement that the synthesis procedure and the annealing temperature of different pyrophosphates must be individually controlled with respect to the choice of host cation. The required differences in synthesis and heat treatment make it hard to evaluate how the choice of host cation influences the conductivity of pyrophosphates.

Chapter 4

Y-doped TiP_2O_7 [1]

Chapter 3 shows that all the four compositions studied have low conductivities in dry atmosphere. According to the sequence given in Section 3.1 titanium pyrophosphates should have the second highest conductivity after tin pyrophosphates. Therefore Y-doped TiP_2O_7 is the next viable candidate: in this chapter its conductivity is studied systematically, to investigate the effect of sintering temperature and phosphorus content.

Abstract

Y-doped TiP_2O_7 has been synthesized and sintered at different temperatures between 370 and 970 °C. Yttrium doping is limited by the low solubility of yttrium in TiP_2O_7. The conductivity is studied systematically as a function of sintering temperature, p_{H_2O}, p_{O_2} and temperature (100-400 °C). Loss of phosphorus upon sintering above 580-600 °C is confirmed by Energy Dispersive Spectroscopy (EDS) and combined thermogravimetry (TG) and mass spectrometry. The conductivity decreases with increasing sintering temperature and decreasing phosphorus content. The highest conductivity is $5.3 \cdot 10^{-4}$ S/cm at 140 °C in wet air (p_{H_2O} = 0.22 atm) after sintering at 370 °C. The conductivity is higher in wet atmospheres than in dry atmospheres. The proton conduction mechanism is discussed and the conductivity is attributed to an amorphous secondary phase that apparently consists mainly of phosphoric acid in the grain boundaries, associated with the presence of excess phosphorus in the samples. A contribution to the conductivity by point defects in the bulk may explain the conductivity trend in dry air and the difference in conductivity between oxidizing and reducing atmospheres at 300-390 °C. Slow loss of phosphorus by evaporation over

[1] The content of this chapter has been published in: A. Lapina, C. Chatzichristodoulou, J. Hallinder, P. Holtappels, and M. Mogensen, "Electrical conductivity of Y-doped TiP_2O_7 between 100-400 °C: effect of sintering temperature and phosphorus content", *Journal of Solid State Electrochemistry*, **18** (1) 39-47 (2014).

time and changes in the distribution of the amorphous phase during testing are suggested as causes of conductivity degradation above 220 °C.

4.1 Introduction

Fuel cells and electrolysers operating at intermediate temperature (200-400 °C) present a number of potential advantages compared to polymer electrolyte membranes fuel cells (PEMFC), operating below 200 °C. The higher temperature improves the electrode kinetics, allows using non-noble metals as catalysts and increases the tolerance to CO.[95] At the same time, the temperature is low enough to avoid many of the issues affecting solid oxide fuel cells (operating above 600 °C), such as catalyst degradation by coarsening, interfacial reactions among components, interconnect oxidation and thermal expansion mismatches.[96,97]

One of the main obstacles toward the development of intermediate temperature fuel cells is the so-called "Norby's gap",[98] i.e. the absence of well-established proton conducting electrolytes with a conductivity above 10^{-2} S/cm in the temperature range 200-400 °C.

The pyrophosphate class of materials (MeP_2O_7, with Me being a tetravalent cation) has drawn interest since the publication by Hibino *et al.*[68] reporting proton conductivities up to $4.7{\cdot}10^{-2}$ S/cm for SnP_2O_7 at 250 °C in unhumidified air. The conductivity in unhumidified air is dependent on the choice of the cation and increases in the order Zr < Ge < Si < Ce < Ti < Sn.[67,68] Acceptor doping further increases the conductivity up to 0.2 S/cm for $Sn_{0.9}In_{0.1}P_2O_7$ at 200 °C in unhumidified air (p_{H_2O} = 0.0075 atm).

However, the conduction mechanism in this class of materials is not clear and conductivities reported in the literature often differ by orders of magnitude: a number of reports show that the transport properties are heavily influenced by the synthesis route and the thermal history of the samples.[68,99–101]

Two conduction mechanisms have been suggested so far for the proton conductivity of pyrophosphates: point defects in the bulk of the material[67,102–104] and amorphous, conducting secondary phases at the grain boundaries.[92,101,105,106] According to the first mechanism[67,68,102,103] the proton conductivity is due to bulk conduction and protons are incorporated in the material. The second mechanism, proposed by Shirai *et al.*,[92,101] suggests instead a core-shell type electrolyte, consisting of a non-conductive pyrophosphate particles (the "core") covered with a highly conductive amorphous layer containing phosphate ions (the "shell").

TiP_2O_7 has, according to Nagao *et al.*,[68] the second highest conductivity among undoped pyrophosphates, reaching a value of $4.6{\cdot}10^{-2}$ S/cm at 250 °C in unhumidified air (p_{H_2O} = 0.0075 atm). Similarly high conductivities for TiP_2O_7 are reported by other authors[92,101,106] using other synthesis routes

and high phosphorus/metal ratios. The conductivity appears to decrease with increasing sintering temperature.[92,101] Nalini *et al.*[103,104] synthesize TiP_2O_7 (undoped or Al, Sc, Fe doped) with the same route as Nagao *et al.*,[68] and examine its conductivity at 500-900 °C after sintering at 1000 °C. They report much lower conductivities for undoped TiP_2O_7 , i.e. circa $1.5 \cdot 10^{-5}$ S/cm and $2.5 \cdot 10^{-6}$ S/cm at 500 °C in dry and wet oxygen respectively. A clear H/D isotope effect proves that the conductivity is mainly protonic, and acceptor doping is reported to have a negligible effect on conductivity.

The differences in synthesis techniques and heat treatments among the different studies make a direct comparison among them difficult: in particular the only works studying the effect of sintering temperature on the conductivity[92,101] use synthesis routes different from the most common one for this class of materials.[67,68,102,103]

In order to help clarify the conductivity mechanism in TiP_2O_7, the material is synthesized, using yttrium as a dopant. The material is sintered at different temperatures. The conductivity is studied systematically as a function of sintering temperature, p_{H_2O}, p_{O_2} and testing temperature (100-400 °C), and correlated to the amount of phosphorus present in the samples (estimated by EDS and TG with the support of mass spectrometry).

4.2 Experimental

4.2.1 Synthesis procedure

TiO_2 powders (Sigma Aldrich; 99.8 %) and Y_2O_3 (Johnson Matthey; 99.90 %) are separately ball milled to reduce agglomeration and then mixed in a beaker according to the ratio Ti:Y = 0.9:0.1. Phosphoric acid (85 % H_3PO_4 in H_2O w/w, Sigma Aldrich) is added to get a P/(Ti+Y) ratio = 2.6, which is reported to be optimal to obtain phase-pure material using this synthesis route.[100] The mixture is stirred on a hot plate (set temperature = 300 °C) until a high viscosity paste is formed. The paste is dried in an oven at 200 °C for two days and manually ground to obtain powders.

As synthesized powders are used to produce pellets (with a diameter of 8 mm and a thickness of 1-1.2 mm) by uniaxial pressing (5400 kg cm^{-2}), which are then sintered at 370, 600, 650, 970 °C (± ca. 2 °C) for 3 hours in alumina crucibles covered with an alumina cap. The alumina cap is used to minimize the loss of phosphorus.[100] The sintered samples are from now on referred to as Ti370, Ti600, Ti650 and Ti970 respectively. The as synthesized material is referred to as Ti_as_synth.

4.2.2 Characterization

XRD measurements are performed in air using a Bruker D8 X-Ray Diffractometer (Bruker-Siemens, Germany), using Cu Kα radiation, with acceler-

ation voltage 40 kV and a filament current of 40 mA. SEM imaging and EDS analysis are performed with a TM-3000 microscope (Hitachi, Japan) equipped with Bruker EDS detector, using 15 kV as accelerating voltage. The relative density of the materials is estimated from the mass and geometrical dimensions of the pellets, using 3.052 g/cm^3 as theoretical density.[107]

Thermogravimetry (TG) is carried out using a Netzsch STA 409CD instrument, with an Omnistar GSD301 mass spectrometer connected at the gas outlet via a tube heated to 150 °C. The temperature is increased stepwise from room temperature to 100, 150, 200, 250, 300, 500, 700 and 900 °C in air with a heating rate of 2 °C/min. The atmosphere is switched from air to N_2, CO_2, 9 % H_2 in N_2, and back to air during a 5 h long hold at 150 °C.

4.2.3 Conductivity

Commercially available PEM CCB (catalyst coated backing) electrodes from IRD A/S with 0.56 mg Pt cm^{-2} are used as electrodes on both faces of the pellets. The material is tested by two-point impedance spectroscopy using a Solartron 1260 (Solartron Analytical, UK). The applied signal has an amplitude of 50 mV and impedance spectra are recorded in the frequency range 1 MHz - 1Hz.

During testing the material is exposed to a constant flux of gas (air, 9 % H_2 - 91 % N_2), either dry (gases from the gas system, estimated p_{H_2O} < 0.001 atm) or humidified (p_{H_2O} = 0.038 or 0.22 atm). A humidity cycle is carried out at each temperature investigated. The gas is humidified by bubbling through a water bottle at controlled temperature prior to entering the experimental setup.

4.3 Results

4.3.1 Characterization

XRD patterns in Figure 4.1 show the phase evolution of the material with increasing sintering temperature. TiP_2O_7 phase (PDF 38-1468) is present in the as-synthesized material and after sintering at all temperatures. The peaks of the TiP_2O_7 phase are duplicated in Ti_as_synth and Ti370, suggesting the presence of at least two crystal structures with slightly different unit cell dimensions. After sintering above 600 °C only one set of TiP_2O_7 peaks is visible in the patterns.

Ti_as_synth contains a detectable amount of $YH_2P_3O_{10}$ (PDF 52-1747) and other second phases which could not be indexed. After sintering at 370 °C, Ti370 contains only TiP_2O_7 and $YH_2P_3O_{10}$. After sintering at 600 °C or higher temperature, TiP_2O_7 and $Y(PO_3)_3$ (PDF 42-0501) are detected instead.

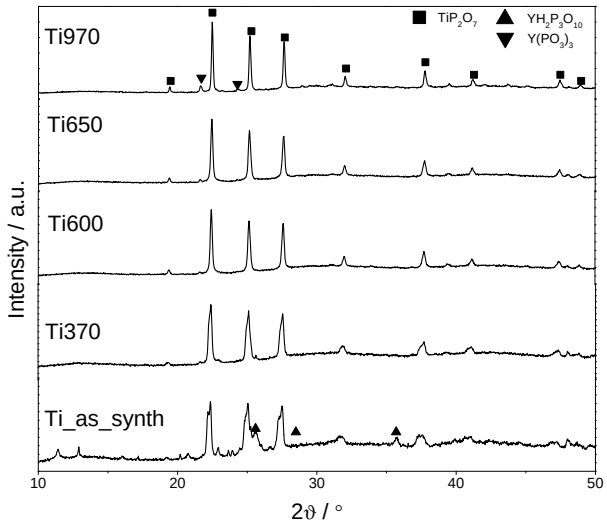

Figure 4.1: XRD patterns of as synthesized and sintered samples. The number in the sample name indicates the sintering temperature.

The XRD patterns of the sintered samples after electrochemical testing are presented in Figure 4.2. A single set of TiP_2O_7 peaks is visible for all the samples, and $YH_2P_3O_{10}$ is the only secondary phase detected. Platinum peaks are due to platinum nanoparticles (contained in the electrodes) left on the material after testing.

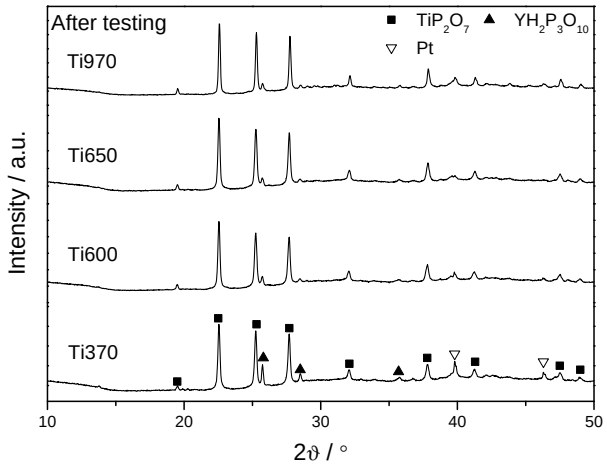

Figure 4.2: XRD patterns of sintered pellets, after electrochemical testing. The number in the sample name indicates the sintering temperature.

The relative density of the material before testing, estimated by the geometrical dimensions and mass of the pellets, is in the 55-65 % range for all the samples.

Figure 4.3 shows a polished cross section of a SEM micrograph of Ti370. The element distribution is studied by EDS analysis and confirms the presence of yttrium-rich regions (i.e. the bright regions in the micrographs, where Y/(Ti+Y) = 0.3 ± 0.1), which according to the XRD measurements we assign to $YH_2P_3O_{10}$ or $Y(PO_3)_3$ depending on the sintering temperature. The Y/(Ti+Y) ratio in the rest of the material (0.03 ± 0.01) is below the one for nominal doping (i.e. 0.1, corresponding to 10 mol %) for all the samples. Accurate quantification of low concentrations of Y is problematic because of the overlapping between phosphorus and yttrium peaks in the EDS spectra.

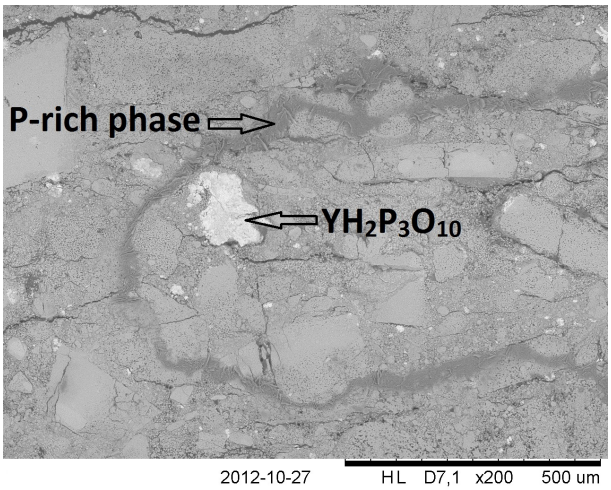

Figure 4.3: SEM micrograph of a polished cross section of Ti370. Notice the presence of the $YH_2P_3O_{10}$ and of the phosphorus rich-region. Cracks are due to sample preparation.

The P/(Ti+Y) ratio is higher in the Y-rich areas than in the rest of the material (Figure 4.5): this trend reflects the difference in P/Metal ratio between $YH_2P_3O_{10}$ or $Y(PO_3)_3$ (P/Y=3) and TiP_2O_7 (P/Ti=2).

The P/(Ti+Y) ratio decreases with increasing sintering temperature, showing that phosphorus is lost during sintering of the material. The significant uncertainty in the determined ratio values is due to the inhomogeneity of the materials.

The TG measurement reported in Figure 4.5 shows a mass loss of 11.4 wt % upon heating in air from room temperature to 900 °C. The material exhibits a mass loss of 1.5 wt % up to 100 °C, and the total mass loss at 300 °C is 2.87 wt %. The amount of water released when heating the samples beyond 200 °C is estimated by in-line mass spectrometry. Under the assumption that all the mass loss taking place below 150 °C is due to water, the mass loss taking place between 300 °C and 900 °C is shown to

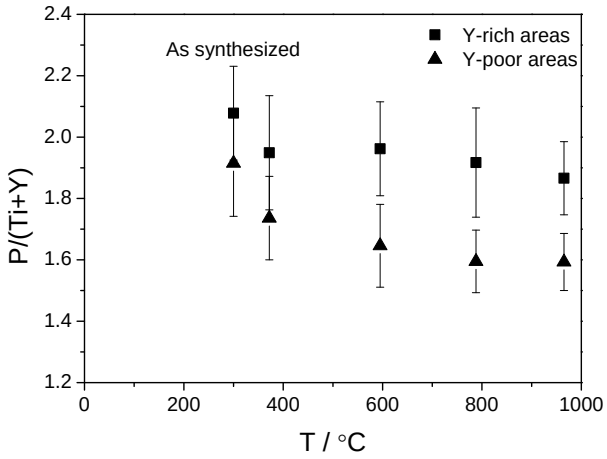

Figure 4.4: P/(Ti+Y) ratios for Y-rich and Y-poor areas in as synthesized material and pellets sintered at different temperatures.

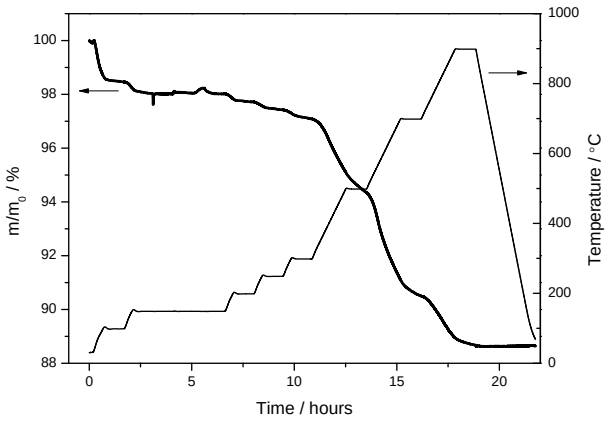

Figure 4.5: Mass relative to original mass m_0 and temperature profile for TG measurement.

be due to loss of both water and phosphorus oxide (Figure 4.6).

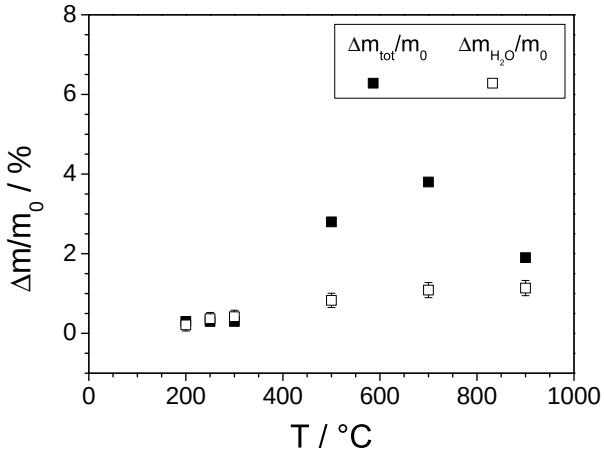

Figure 4.6: Total mass loss (Δm_{tot}) and mass loss associated with dehydration (Δm_{H_2O}) relative to the original mass m_0, at each temperature step.

4.3.2 Conductivity

The conductivity of all the materials increases upon switching from dry to wet atmosphere at 140 °C, as shown in Figure 4.7. The conductivity of Ti370, Ti600 and Ti650 increases by 1-3 orders of magnitude in less than 10 hours when changing the atmosphere from dry air to air with p_{H_2O} = 0.038 atm, reaching $3.2{\cdot}10^{-5}$, $1.8{\cdot}10^{-5}$ and $1.3{\cdot}10^{-5}$ S/cm respectively; the conductivity of Ti970 ($5{\cdot}10^{-9}$ S/cm) is instead almost unaffected by exposure to air with p_{H_2O} = 0.038 atm. Further increasing the p_{H_2O} to 0.22 atm improves the conductivity of all the materials: after about 60 hours of exposure to air or H_2/N_2 with p_{H_2O} = 0.22 atm the conductivity of Ti970 increases by three orders of magnitude ($3{\cdot}10^{-5}$ S/cm) and becomes only slightly lower than that of Ti600 and Ti650 ($5{\cdot}10^{-5}$ and $3.8{\cdot}10^{-5}$ S/cm), which increases only 2-3 times. The highest conductivity measured in this study is $5.3{\cdot}10^{-4}$ S/cm for Ti370 at 140 °C in air with p_{H_2O} = 0.22 atm. Upon switching back to dry air, the conductivity decreases by 1-2 orders of magnitude, but is 1-2 orders of magnitude higher than it is in dry air prior to the humidity cycling. The conductivity for the different samples always follows this trend: $\sigma_{Ti370} > \sigma_{Ti600} > \sigma_{Ti650} > \sigma_{Ti970}$.

The increase in conductivity upon exposure to wet atmosphere is less pronounced at 220 °C than at 140 °C (as can be seen comparing Figures 4.7 and 4.8). All the materials, including Ti970, show the same behavior upon changes of p_{H_2O}. The conductivity decreases over time for all the materials, in particular at high p_{H_2O}: it decreases by ca. one order of magnitude within 60 hours in air or H_2/N_2 with p_{H_2O} = 0.22 atm, from $5.3{\cdot}10^{-5}$ to $7.5{\cdot}10^{-6}$

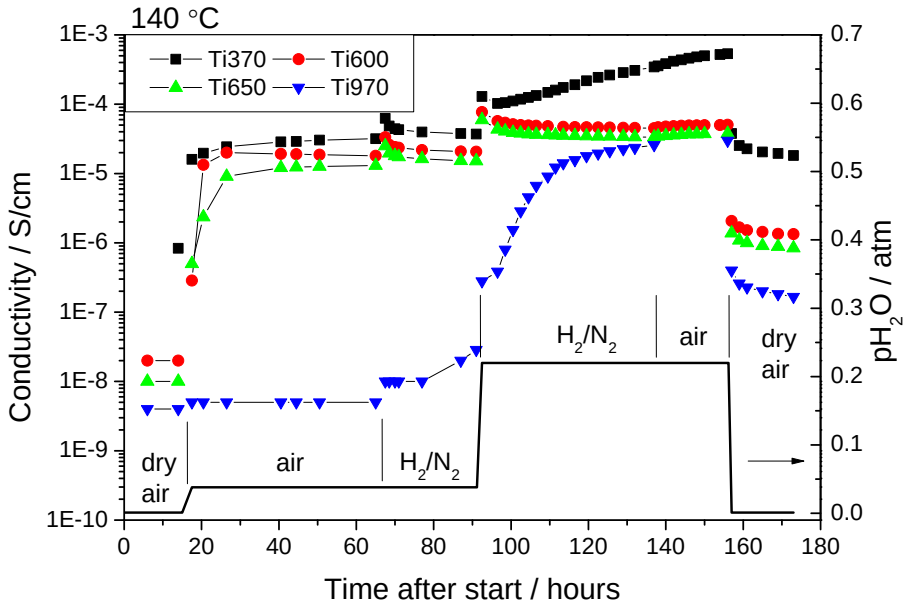

Figure 4.7: Conductivity of Ti370, Ti600C, Ti650, Ti970 as a function of time at 140 °C in air and H_2/N_2 under varying p_{H_2O}.

S/cm for Ti370.

In both Figures 4.7 and 4.8 the conductivity increases suddenly upon switching from air to H_2/N_2 with p_{H_2O} = 0.038 atm (at 64 and 206 hours after start respectively). This is due to the formation of water by the reaction of oxygen and hydrogen in the two gas mixtures: p_{H_2O} is thus higher than 0.038 atm right after the switch. This is a transitory effect and as is shown in Figures 4.7 and 4.8, the conductivity in H_2/N_2 decreases over time and reaches a value close to the one before the atmosphere switch. At 140 °C and 220 °C the conductivity in wet atmosphere (p_{H_2O} = 0.038 or 0.22 atm) is approximately the same both in oxidizing (air) and reducing (H_2/N_2) atmosphere.

The conductivity in dry air (after the humidity cycle at each temperature) is presented in Figure 4.9, together with conductivity values extrapolated from the data recorded at 500-1000 °C by Nalini *et al.*[103] for undoped TiP_2O_7 in dry O_2. The conductivity increases with increasing temperature in the range 220-390 °C: Ti600, Ti650 and Ti970 have similar values, while Ti370 has a higher conductivity. Conductivity values at 140 °C are 1-2 orders of magnitude higher than at 220-390 °C for all the samples.

Figures 4.10 and 4.11 provide an overview of the trends in conductivity for each sample in wet atmosphere (p_{H_2O} = 0.038 or 0.22 atm), both oxidizing (air) and reducing (H_2/N_2). The conductivity in wet air decreases with increasing temperature for all the samples: the increase in conductivity with increasing p_{H_2O} is more important at 140-220 °C than at 220-390 °C,

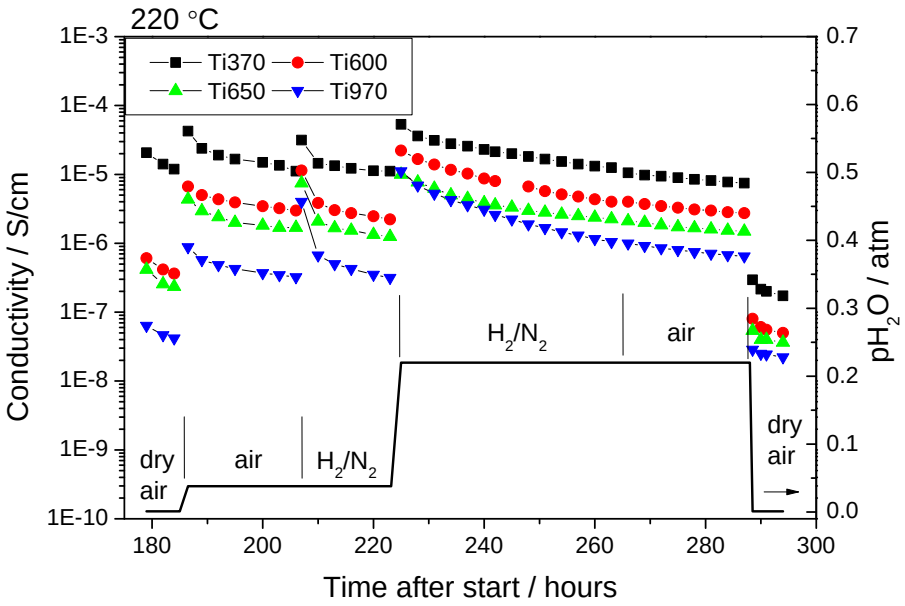

Figure 4.8: Conductivity of Ti370, Ti600C, Ti650, Ti970 as a function of time at 220 °C in different atmospheres and at different humidity.

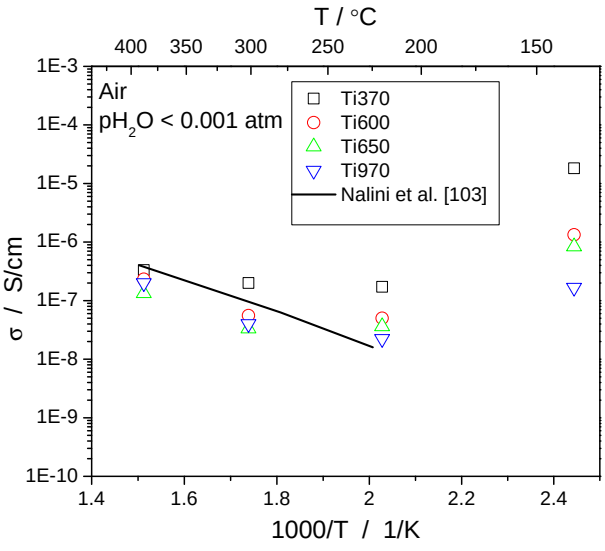

Figure 4.9: Conductivity in dry air as a function of temperature, measured after the hydration/dehydration cycle at each temperature (see Figures 4.7 and 4.8), and conductivity extrapolated from data by Nalini *et al.*[103] for TiP_2O_7 in dry O_2.

as can be seen comparing Figure 4.10a and Figure 4.11a. The conductivity values for Ti600, Ti650 and Ti970 are similar in all the conditions except at 140 °C with p_{H_2O} = 0.038 atm.

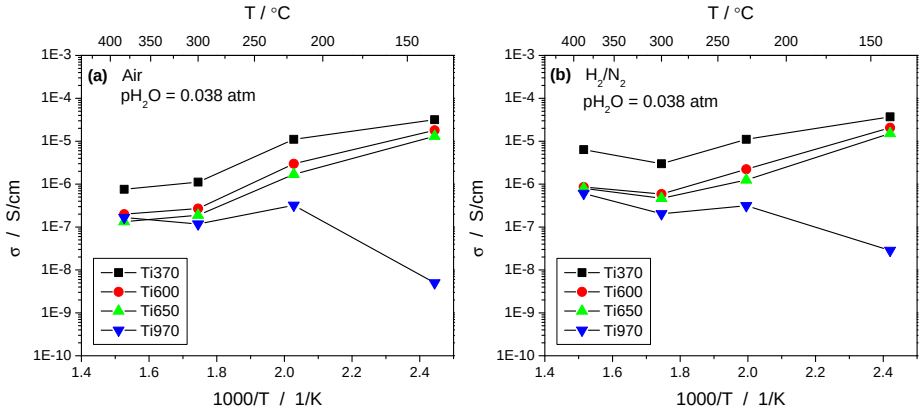

Figure 4.10: Conductivity as a function of temperature in: (a) air, p_{H_2O} = 0.038 atm, (b) H_2/N_2, p_{H_2O} = 0.038 atm.

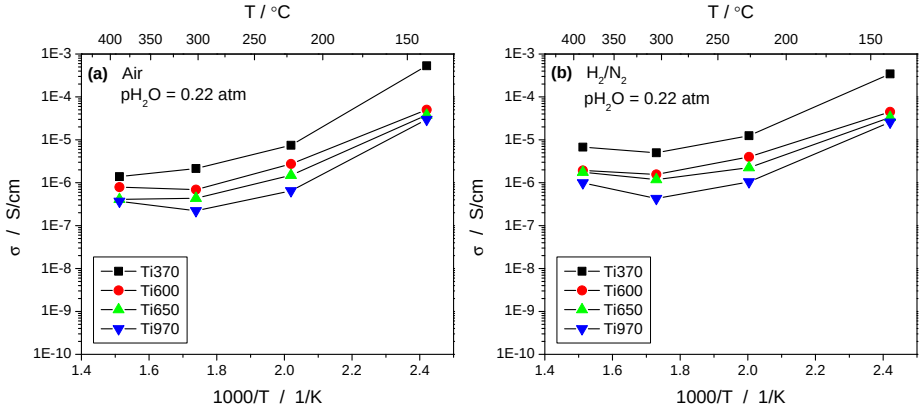

Figure 4.11: Conductivity as a function of temperature in: (a) air, p_{H_2O} = 0.22 atm, (b) H_2/N_2, p_{H_2O} = 0.22 atm.

At 140 °C and 220 °C the conductivity does not change switching from air to H_2/N_2 with the same p_{H_2O} (see Figures 4.7 and 4.8), while at 280-390 °C conductivity in wet H_2/N_2 is higher than in wet air.

4.4 Discussion

4.4.1 Composition and phase relations

The thermal dehydration and decomposition of phosphoric acid (H_3PO_4) has been studied by various authors.[108–110] Upon heating at 200-300 °C H_3PO_4

dehydrates and is gradually converted into pyrophosphoric acid ($H_4P_2O_7$), metaphosphoric acid ($(HPO_3)_n$) or polyphosphoric acid ($H_{n+2}P_nO_{3n+1}$).[108,109] Huang *et al.*[110] report that 85 wt % H_3PO_4 steadily loses mass due to dehydration upon heating at 400-500 °C. The phosphoric acid decomposes to form P_2O_5, that sublimates above 300 °C[110] and vaporizes at about 580-600 °C.[109,110]

Based on this evidence, we assume that only water is lost below 150 °C in the TG measurement (Figure 4.5). The 1.5 wt % loss below 100 °C is due to the loss of absorbed water, and then the phosphoric acid dehydrates above 200 °C. Mass spectrometry measurements confirm that other species than water are lost at 600 °C and above: therefore the 8.5 wt % loss between 300 °C and 900 °C is attributed to both dehydration of pyro-, meta- and poli-phosphoric acids and loss of P_2O_5 from excess phosphorus.

XRD and EDS measurements (Figures 4.1 and 4.4) indicate that most of the yttrium in the material is not incorporated in the TiP_2O_7 structure, but is rather present as $YH_2P_3O_{10}$ (in Ti_as_synth and Ti370) or $Y(PO_3)_3$ (Ti600, Ti650, Ti970). The concentration of yttrium outside the yttrium-rich areas is low (Y/(Ti+Y) = 0.03 ± 0.01) and does not change with increasing sintering temperature, suggesting this is due to low solubility of yttrium in TiP_2O_7 and not due to diffusion limitations.

Upon sintering above 600 °C (Figure 4.1) $YH_2P_3O_{10}$ dehydrates to form $Y(PO_3)_3$:

$$YH_2P_3O_{10} \rightarrow Y(PO_3)_3 + H_2O \tag{4.1}$$

During testing in humid atmosphere, the opposite reaction takes place and $YH_2P_3O_{10}$ is formed in all the samples (Figure 4.2).

The P/(Ti+Y) ratio estimated by EDS on Ti_as_synth (1.9 ± 0.17 for the Y-poor areas) is much lower than the 2.6 ratio used in the starting chemicals. This is apparently in disagreement with the literature reports previously discussed and our findings, that indicate no significant phosphorus loss below 300 °C.[108–110] However it must be pointed out that the accuracy of the absolute values of the P/(Ti+Y) ratio determined by EDS may be compromised by the absence of reference calibration materials. The XRD measurements show that TiP_2O_7 phase is present in all the materials after sintering, therefore a ratio P/(Ti+Y) of at least 2 should be expected in order for the material to keep this structure.

We suggest that while the trend of values in Figure 4.4 accurately represents the decrease in phosphorus content with increasing sintering temperature, the absolute value of the stoichiometry may suffer a systematic error.

The TiP_2O_7 structure has a cubic unit cell in space group Pa 3 and is built up by TiO_6 octahedra and PO_4 tetrahedra sharing corners in a 3D network.[107] The duplication of peaks in Ti_as_synth and Ti372 suggests

the presence of at least two TiP_2O_7 structures with slightly different cell dimension, which could be due to local differences in phosphorus content in the samples. The secondary phases detected in Ti_as_synth (Figure 4.1) that cannot be indexed are probably related to the presence of excess phosphoric acid. EDS measurements (Figure 4.4) confirm that the phosphorus content in Ti_as_synth is higher than in the sintered samples.

The peak duplication is removed after sintering at 600 °C, suggesting that only one structure is formed. Upon sintering at 600, 650 and 970 °C the material keeps the same crystal structure (Figure 4.1), but as stated before the phosphorus content decreases (Figure 4.4): we suggest that all the mass losses recorded in the TG measurement should be attributed to loss of water and phosphorus from the excess phosphoric acid. This is supported by Harrison and Hummel,[111] who report that samples prepared with a ratio P/Ti = 4 lose P_2O_5 upon heating above 500 °C and have a stoichiometric composition (TiP_2O_7) after heating at 1000-1200 °C. Decomposition of the TiP_2O_7 structure itself takes place beyond the sintering temperature range used in this study, in fact above 1150 °C according to Bamberger and Begun[112] and above 1400 °C according to Harrison and Hummel.[111]

Therefore it is suggested that while all the samples have the same crystal structure (TiP_2O_7 plus $YH_2P_3O_{10}$) during the test, the amount of excess phosphorus decreases with increasing sintering temperature.

4.4.2 Conductivity relation to structure and composition

The conductivity increases dramatically upon exposure to wet atmosphere at all temperatures and it decreases with increasing sintering temperature ($\sigma_{Ti370} > \sigma_{Ti600} > \sigma_{Ti650} > \sigma_{Ti970}$). The phosphorus content in the material decreases as well with increasing temperature, as found by EDS measurements (Figure 4.4) and supported by TG and mass spectrometry measurements (Figures 4.5 and 4.6). This suggests that a decrease in phosphorus content causes a decrease in conductivity.

The amount of phosphorus is reported to be of paramount importance for both the proton conduction mechanisms suggested in the literature (point defects in the bulk of the material[67,68,102–104] and amorphous secondary phases at the grain boundaries[92,101,105,106]). Nagao *et al.*[68] report a decrease in conductivity of two orders of magnitude because of a 15 % phosphorus deficiency in $Sn_{0.9}In_{0.1}P_2O_7$ and attribute it to distortion and disorder induced into the crystal structure by the phosphorus deficiency. Shirai *et al.*[92] and Nalini *et al.*[103] state instead that sintering at high temperatures decreases the conductivity by removing the excess phosphoric acid from the grain boundaries.

As discussed in Section 4.4.1, heat treatment in dry air up to 300 °C causes the excess phosphoric acid in the material to dehydrate forming other compounds, such as $H_4P_2O_7$, $(HPO_3)_n$, $H_{n+2}P_nO_{3n+1}$ and P_2O_5. It is sug-

gested that the conductivity increases when testing in wet atmosphere because such compounds rehydrate forming a more conducting phase at the grain boundaries, probably H_3PO_4, for example according to the reaction:

$$P_2O_5 + 3H_2O \rightarrow 2H_3PO_4 \tag{4.2}$$

Ti370 contains more excess phosphoric acid than samples sintered at 600 °C or above (where P_2O_5 vaporization starts[109,110]), thus it is expected to absorb the most water from the atmosphere and possess the largest volume fraction of fast proton conducting phase at the grain boundaries.

The sample sintered at 970 °C, i.e. Ti970, contains less excess phosphorus compared to samples sintered at lower temperature. During the initial stage of the test (between 20 and 160 hours in Figure 4.7) the conductivity of the material increases slowly over time in wet atmosphere and it becomes comparable with Ti650 and Ti970 after ca. 40 hours at $p_{H_2O} = 0.22$ atm (Figure 4.7). It is here suggested that the amorphous phase formed at the grain boundaries is mobile and thus its distribution may change over time. The conducting phase has to reach a certain degree of percolation for the conductivity to increase significantly from the value in dry atmosphere, and it is here suggested that a higher degree of reorganization of the conducting phase is necessary for Ti970 compared to the other samples, since it contains a smaller volume fraction of fast proton conducting phase.

The presence of yttrium hydrogen phosphate phase is not responsible for the different conductivity of the samples. In fact, as shown in Figure 4.2, $YH_2P_3O_{10}$ is present in all the samples after testing, most likely formed upon exposure to wet atmosphere. Moreover, Figure 4.3 shows that because of its small volume fraction, it does not form a percolating network that can contribute to the overall conductivity.

While the conductivity in humid atmosphere at 140 °C increases or stays constant over time, all the materials experience a significant decrease in conductivity at 220 °C, in particular at high humidity. This decrease can be due to microstructural changes in the material, such as redistribution of the fast proton conducting phase over time. Moreover, it is here suggested that this could be due also to evaporation of phosphorus (from H_3PO_4) over time. Small losses of phosphorus occur at 120-180 °C in high temperature PEM fuel cells[113] and the fraction of phosphorus in the vapor above highly concentrated phosphoric acids increases steeply with temperature in the 200-400 °C range.[114] This process may be of limited importance during fast heat treatments in stationary atmosphere (such as the sintering) but relevant in the conditions of this conductivity test (circa 500 hours in flowing gas). Loss of phosphorus in wet atmosphere has recently been presented as a possible cause of degradation for In-doped SnP_2O_7.[115]

The conductivity decreases with increasing temperature for all samples when tested in wet atmosphere. At higher temperature the charge carriers

have higher mobility, but their concentration is expected to decrease because of thermally induced dehydration. Additionally, the degradation processes suggested can occur more rapidly at higher temperatures. The fraction of phosphorus in the vapor increases with temperature, therefore a bigger loss is expected. If the fast conducting phase is H_3PO_4 then its viscosity should decrease at higher temperature, accelerating redistribution processes.

This trend with temperature suggests that the conduction mechanism in wet atmosphere is mainly due to a highly conducting phase at the grain boundaries of the material, since conduction by point defects in the bulk is expected to be a thermally activated process.

In dry atmosphere the conductivity for Ti600, Ti650 and Ti970 increases with the temperature in the 220-390 °C range (Figure 4.9) and its values are similar to what is obtained by extrapolation of the conductivity data presented by Nalini *et al.*[103] to lower temperature for undoped TiP_2O_7 (sintered at 1000 °C) in dry O_2. Thus it is possible that a contribution from a bulk conducting process is present, but it is overshadowed by the grain boundary mechanism in wet atmosphere at 140-220 °C. A bulk conduction process could also account for the different p_{O_2} dependence of the conductivity at 140-220 °C and 300-390 °C. At 140-220 °C the conductivity in wet atmosphere does not change between air and H_2/N_2 (as seen in Figures 4.7 and 4.8), while at 300-390 °C the conductivity increases 2-8 times upon the switch from air to H_2/N_2. This behavior could be due to an electronic contribution to the conductivity, not visible at lower temperature because the grain boundary conduction of protons is dominating.

4.4.3 Conclusions

TiP_2O_7 has been synthesized and sintered at different temperatures. Yttrium doping is limited by the low solubility of yttrium in TiP_2O_7. TG and EDS measurements confirm the loss of phosphorus upon sintering at temperatures above 580-600 °C and this is correlated with the trend in proton conductivity of the samples.

The highest conductivity measured in this study is $5.3 \cdot 10^{-4}$ S/cm at 140 °C in wet air (p_{H_2O} = 0.22 atm), for a sample sintered at 370 °C. The conductivity heavily depends on p_{H_2O} and decreases with increasing temperature in wet atmosphere. The conductivity at 140-220 °C is attributed to amorphous secondary phases at the grain boundaries, associated with the presence of excess phosphorus in the samples. The contribution to conduction by point defects in the bulk becomes apparent in dry air at 300-390 °C and can account for the difference in conductivity between oxidizing and reducing atmospheres under these conditions. The lower conductivity of samples sintered at 600 °C or above is due to lower excess phosphorus content. Loss of phosphorus due to evaporation and changes in the distribution of the amorphous phase over time are suggested as causes of conductivity

degradation above 220 °C.

Chapter 5

Cerium phosphates[1]

The results presented in Chapter 4 show that also the conductivity of Ti pyrophosphate in dry atmosphere is too low. The next composition worth considering is Ce pyrophosphate / phosphate, that showed promising conductivity in Chapter 3 despite phase stability issues. In this chapter the thermal evolution and the long term conductivity of Ce phosphates are studied.

Abstract

The thermal evolution of the phase composition of CeP_2O_7 and $Ce(PO_3)_4$ with 10 mol % Y and Gd doping, respectively, is examined by in-situ powder X-Ray diffraction and thermogravimetry with in-line mass spectroscopy. The phase composition depends critically on the P to metal ratio, the annealing temperature, humidity and time. CeP_2O_7 and $Ce(PO_3)_4$ are completely decomposed to $CePO_4$ following a 1100 h long conductivity test at 155 °C. The conductivity of 10 mol % Gd doped $Ce(PO_3)_4$ (synthesized with P/(Ce+Gd) = 5.0) reaches a value of $6.4{\cdot}10^{-2}$ S/cm at 150 °C under wet conditions (p_{H_2O} = 0.2 atm). The conductivity of 10 mol % Y doped CeP_2O_7 (synthesized with P/(Ce+Y) = 3.1) is $1.9{\cdot}10^{-2}$ S/cm under the same conditions. Long term conductivity measurements are reported here for the first time and the effect of repeated hydration-dehydration cycles on the conductivity is examined. Exsolution of P_mO_n and increase of the highly hygroscopic amorphous secondary phase significantly affects the conducting properties. KH_2PO_4 is observed to re-crystallize and form amorphous potassium phosphate at temperatures above 100 °C in the CeY10+P:KH_2PO_4 composite (with excess H_3PO_4) resulting in a conductivity value of $2.6{\cdot}10^{-2}$

[1]Published as: C. Chatzichristodoulou, J. Hallinder, A. Lapina, P. Holtappels, and M. Mogensen, "Phase composition and long-term conductivity of acceptor doped $Ce(PO_3)_4$ and CeP_2O_7 with variable P/metal ratio and of CeP_2O_7-KH_2PO_4", *Journal of The Electrochemical Society*, **160** (8) F798-F805 (2013)

S/cm at 150 °C and $p_{H_2O} = 0.2$ atm.

5.1 Introduction

Fuel cells, electrolyzers and other electrochemical devices operating at intermediate temperatures (ca. 200 °C) have several advantages compared to their low temperature (< 100 °C) counterparts. These include improved electrode kinetics (enabling the use of non-noble metal catalysts), reduced CO poisoning, easier water management, as well as enabling the use/production of hydrocarbon fuels, e.g. methanol, ethanol and dimethylether. Intermediate temperature operation holds certain advantages also in comparison to high temperature operation (> 600 °C), such as reduced corrosion and reactivity/interdiffusion among components, minimized degradation due to catalyst coarsening, in addition to the potential for production of synthetic fuels.

In order to materialize these potential advantages, intermediate temperature proton conducting electrolytes are required. The materials group of pyrophosphates, MeP_2O_7 with Me being a 4-valent cation, has attracted considerable attention during the last decade, since the discovery of high proton conductivity in SnP_2O_7 at intermediate temperatures.[116] The conductivity of MeP_2O_7 at 200 °C and $p_{H_2O} \approx 0.001$ atm shows an increasing tendency in the order Zr < Ge < Si < Ce < Ti < Sn.[67–69,76,77,93,117] Acceptor doping results in increased conductivity, that goes through a maximum at 5 mol % Al,[100] 6 mol % Sc,[75] 9 mol % Ga,[118] 10 mol % In[68] or Mg,[73] and 20 mol % Sb.[74]

Ionic transference numbers above 0.8 are reported in most cases by concentration cell measurements,[68,69,75,100] the deviation from unity being attributed either to leaks in the experimental setup or to electronic conductivity. Wang *et al.*[75] measure an ionic transference number of about 0.95 for $Sn_{0.94}Sc_{0.06}P_2O_7$ in wet H_2 and show that the protonic and oxide ionic part are 0.8 and 0.15, respectively. On the other hand, Nalini *et al.*[77] find negligible oxide ionic contribution in wet O_2 for 2 mol % Y-doped ZrP_2O_7. Therefore, aside from the general agreement that pyrophosphates are mainly ionic conductors, and predominantly protonic, the exact contribution of each charge carrier and its dependence on the O_2 and H_2O partial pressures remain unknown.

Furthermore, despite the numerous publications dealing with the conductivity of pyrophosphates and polyphosphates, it is still disputed whether the proton conductivity is associated with point defects incorporated in the bulk of the materials or with the presence of amorphous secondary phases residing at the grain boundaries. A number of studies have shown that the transport properties of pyrophosphates are very sensitive to the synthesis method and thermal history of the samples,[68,76,81,100,101] which affect the

P content and the phase composition of the investigated powders. Nevertheless, a detailed examination of the phase and composition development with temperature, humidity and over extended time periods is often lacking, which may be the reason behind the large differences in the transport properties reported by different groups.

In general, the higher the H_3PO_4 to metal ratio used in the synthesis the higher the conductivity of the resulting samples.[68,81,100] Also, higher annealing temperatures generally result in reduced P content in the samples and reduced conductivities.[77,91,101,103] The most commonly followed synthesis route involves the use of excess H_3PO_4 in the starting mixture, a tactic that entails the risk of forming a P-rich shell around the pyrophosphate particles that will influence the transport properties. The conductivity is then usually measured in the temperature range 100-300 °C and found to undergo a maximum at around 150-200 °C. A monotonically thermally activated behavior has been observed by Nalini *et al.*[77,103] in the temperature range 300-1000 °C for undoped and acceptor doped ZrP_2O_7 and TiP_2O_7.

A number of Ce-based phosphates are known to form and their transport properties have been investigated to some extent. $CePO_4$, which can be substituted with up to 1-2 mol % Sr, is known to be a mixed protonic-electronic conductor, with a proton conductivity of about 10^{-5} S/cm at 500 °C in 4.2 % H_2O.[119] The p-type electronic conductivity of Sr doped $CePO_4$ has a value of about 10^{-3} S/cm under similar conditions.[119] The conductivity of CeP_2O_7 and $Ce(PO_3)_4$ doped with 1 mol % Gd has been investigated by Onoda *et al.*[88,120] in the temperature range 400 to 650 °C, yielding a value of about 10^{-6} S/cm at 400 °C in air with 4.2 % H_2O. Significantly higher conductivity values were reported recently for undoped and 10 mol % Mg doped CeP_2O_7, reaching a value of $4{\cdot}10^{-2}$ S/cm at 200 °C in air with 11.4 % H_2O.[69,76] More recently, Singh *et al.*[121] reported maximum conductivity values of $3.6{\cdot}10^{-6}$ S/cm at 400 °C in dry air and $2.1{\cdot}10^{-4}$ S/cm at 175 °C in air with 6 % H_2O for undoped CeP_2O_7. Somewhat higher values were reported upon Sr doping, with the composition containing 10 mol % Sr showing a maximum conductivity of $4.3{\cdot}10^{-6}$ S/cm at 430 °C in dry air and $6.3{\cdot}10^{-3}$ S/cm at 90 °C in air with 12 % H_2O.[122]

In an effort to resolve these discrepancies, we synthesize CeP_2O_7 and $Ce(PO_3)_4$ with 10 mol % Y or Gd doping, and carefully investigate the thermal evolution of their phase composition by in-situ powder X-Ray diffraction and thermogravimetry. The conductivity of well characterized powders is measured at various temperatures, and steam and oxygen partial pressures. Long term conductivity measurements are reported here for the first time and the effect of repeated hydration-dehydration cycles on the conductivity is examined. A careful post-mortem analysis of the samples used for the conductivity measurements is also undertaken.

5.2 Experimental

5.2.1 Synthesis

$Ce_{0.9}Y_{0.1}(P_2O_7)_{1-\delta}$ (CeY10) is synthesized by mixing CeO_2 (Aldrich; 99.9 %), Y_2O_3 (Johnson Matthey; 99.9 %) and H_3PO_4 (85 % w/w; Aldrich) at molar ratios of Ce/Y = 9 and P/(Ce+Y) = 2.6 in a glass crucible and heated on a hot plate held at 300 °C while stirring for 1-4 h until a high viscosity slurry is obtained. The slurry is dried overnight at 200 °C. The resulting powder is then distributed in alumina crucibles and calcined at 380, 600, 790 °C for 6 h and 980 °C for 12 h. The P/(Ce+Y) ratio is increased to 3.1 by mixing the as-synthesized CeY10 powder with additional H_3PO_4 (CeY10+P). The resulting powder is calcined at 380, 600, 790 and 980 °C for 3 h. $Ce_{0.9}Gd_{0.1}(PO_3)_{4-\delta}$ (CeGd10) is synthesized by mixing 10 mol % Gd doped ceria (CGO; Rhodia) and H_3PO_4 (85 % w/w; Aldrich) at a P/(Ce+Gd) molar ratio of 5 and following the same procedure as described for CeY10. The resulting powder is then placed in an alumina crucible and heated at 350 and 400 °C for 12 h. A CeY10+P:KH_2PO_4 composite is synthesized by mixing CeY10+P, calcined at 380 °C, with KH_2PO_4 at a molar ratio of (Ce+Y)/K = 4. Powder X-Ray diffraction (PXD) is employed for phase composition determination. A Bruker D8 Advance diffractometer with Cu Kα radiation and a PSD LynxEye detector, equipped with an MRI high temperature stage, is used for the in-situ Powder X-Ray diffraction experiments. Measurements are performed in the temperature range from room temperature to 700 °C in air, and in the 2θ range 10-80° with steps of $\approx 0.02°$. The microstructure of the synthesized powders is examined by scanning electron microscopy (SEM) using a Zeiss Evo 60 microscope.

5.2.2 Thermogravimetry

Thermogravimetric (TG) analysis is performed using a Netzsch STA 409CD instrument, with an Omnistar GSD301 mass spectrometer connected at the gas outlet via tubing heated at 150 °C. The temperature is increased stepwise from room temperature to 100, 150, 200, 250, 300, 500, 700 and 900 °C in dry air at a ramp rate of 2 °C/min. The atmosphere is changed from dry air to dry N_2, dry CO_2, dry 9 % H_2 in N_2, and back to dry air during a 5 h long hold at 150 °C. By "dry" we refer to gas that has not been humidified, and corresponds to a p_{H_2O} of less than 10^{-3} atm. Approximately 100 mg of each powder is used for the measurements.

5.2.3 Conductivity

Disc shaped samples with a diameter of 10 mm are prepared for conductivity measurements by uniaxial pressing of the synthesized powders at a pressure of ≈ 300 MPa. The relative geometric density of the pressed bodies is in the

range 55-65 % for all compositions. Commercially available PEM catalyst coated backing electrodes from IRD A/S with 0.56 mg Pt/cm^2 are used. The conductivity is determined by electrochemical impedance spectroscopy (EIS) using a Solartron 1260 frequency response analyzer. The measurements are carried out with a 20 mV amplitude AC signal over a frequency range of 1 Hz to 1 MHz with 10 points per decade.

5.3 Results

5.3.1 Phase composition

5.3.1.1 CeY10

The phase composition of the as synthesized CeY10 powder, and after calcination at 380 and 790 °C for 6 h and 980 °C for 12 h in air is determined by XRD. As can be seen in Figure 5.1, it consists mainly of CeP_2O_7 (cubic, Pa-3) and CeO_2 (cubic, Fm-3m) phases, which indicates that the reaction between CeO_2, Y_2O_3 and H_3PO_4 is not completed. All Ce containing phases are assumed doped with Y (for CeY10 and CeY10+P) or Gd (for CeGd10) even though this is not explicitly stated or indicated in the chemical formulas. After calcination at 380 °C the amount of CeO_2 is significantly reduced, and CeP_2O_7 is now the main phase. Upon calcination at 790 °C new phases appear, whereas the amount of CeO_2 does not decrease further. CeP_2O_7 remains the main phase at 790 °C, but presence of $Ce(PO_3)_4$ (orthorhombic, Pbcn) is clearly observed in the XRD pattern. A small amount of $Ce(PO_3)_3$ (orthorhombic, $C222_1$) is also identified. $Ce(PO_3)_3$ becomes the main phase after calcination at 980 °C, with $CePO_4$ (monoclinic $P2_1/n$) appearing as the secondary phase. CeP_2O_7, $Ce(PO_3)_4$ or CeO_2 are completely absent.

In order to investigate the influence of the P/(Ce+Y) ratio in the development of the phase composition with calcination temperature, the as synthesized CeY10 powder is mixed with additional H_3PO_4 (85 % w/w), reaching a nominal P/(Ce+Y) ratio of 3.1. The XRD patterns of the CeY10+P powder calcined at 380, 600, 790 and 980 °C in air for 3h are shown in Figure 5.2. It can be seen that the CeY10+P powder calcined at 380 °C contains a smaller amount of CeO_2, as compared to the CeY10 powder calcined at the same temperature, and is almost single phase CeP_2O_7. Calcination at 600 °C results in a two phase mixture of CeP_2O_7 and $Ce(PO_3)_4$. There is almost no change after calcination at 790 °C. The CeY10+P powder calcined at 790 °C contains a larger amount of $Ce(PO_3)_4$ than the CeY10 powder. After calcination at 980 °C the CeY10+P powder is almost single phase $Ce(PO_3)_3$, containing only a minor amount of $CePO_4$.

In-situ XRD is employed in order to determine the temperatures of the observed phase transitions in the Ce-Y-P-O system. XRD patterns of CeY10 powder are recorded in the temperature range 300 to 700 °C in steps of 50

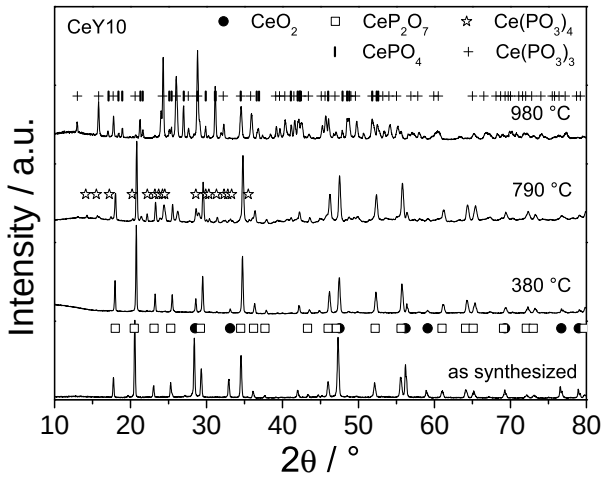

Figure 5.1: XRD patterns of CeY10 powder (P/(Ce+Y) = 2.6) as synthesized and calcined at 380 and 790 °C for 6h and at 980 °C for 12h in air.

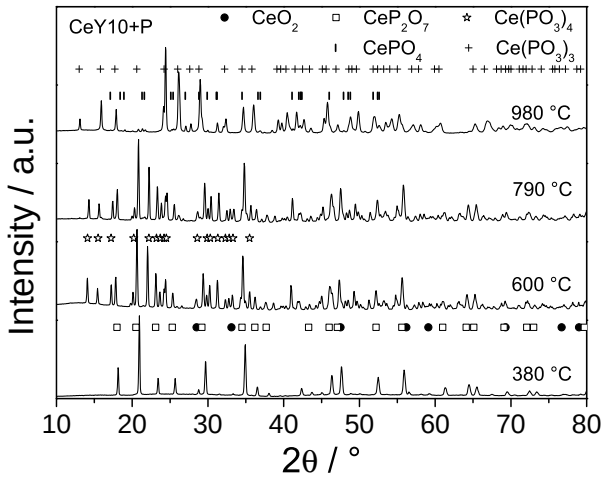

Figure 5.2: XRD patterns of CeY10+P powder (P/(Ce+Y) = 3.1) calcined at 380, 600, 790 and 980 °C in air for 3h.

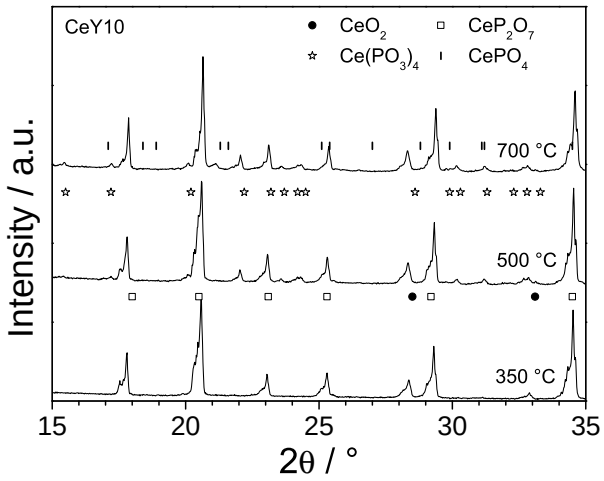

Figure 5.3: In-situ XRD patterns of CeY10 powder recorded at 350, 500 and 700 °C in air.

°C. The in-situ XRD patterns obtained at 350, 500 and 700 °C are presented in Figure 5.3. CeP_2O_7 and unreacted CeO_2 are the only phases observed up to 350 °C. $Ce(PO_3)_4$ appears at 400 °C and its amount increases gradually up to 500 °C. No further change in phase composition is observed until the temperature of 700 °C, where a small amount of $CePO_4$ is also detected.

The phase development with temperature can be associated with the following reaction scheme:

$$CeP_2O_7 + 2\,H_3PO_4 \rightarrow Ce(PO_3)_4 + 3\,H_2O \quad (T \geq 400\,^\circ C) \tag{5.1}$$

$$2\,Ce(PO_3)_4 \rightarrow 2\,Ce(PO_3)_3 + P_2O_5 + \frac{1}{2}\,O_2 \quad (T > 700\,^\circ C) \tag{5.2}$$

$$Ce(PO_3)_3 \rightarrow CePO_4 + P_2O_5 \quad (T > 700\,^\circ C) \tag{5.3}$$

The formation of $Ce(PO_3)_4$ can also take place according to the following reaction:

$$2\,CeP_2O_7 \rightarrow Ce(PO_3)_4 + CeO_2 \tag{5.4}$$

which does not require the presence of excess H_3PO_4. Since the amount of CeO_2 is found to decrease or to remain approximately constant upon increasing calcination temperature, we can conclude that $Ce(PO_3)_4$ forms according to Reaction 5.1. Excess H_3PO_4 is expected in both CeY10 and CeY10+P, either due to incomplete reaction between CeO_2+Y_2O_3 and H_3PO_4, or due to the addition of excess H_3PO_4 during synthesis.

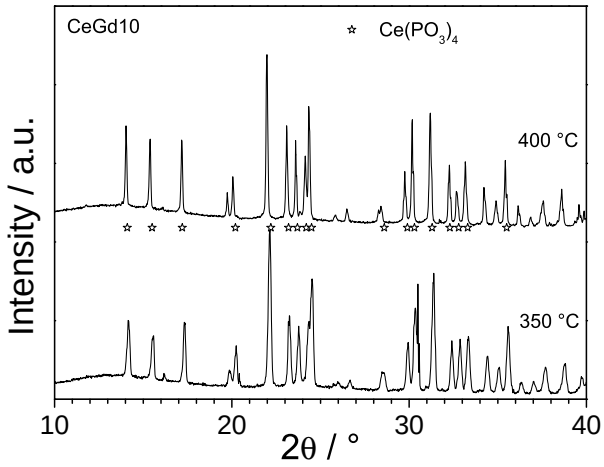

Figure 5.4: XRD patterns of CeGd10 powder calcined at 350 and 400 °C in air for 12h.

5.3.1.2 CeGd10

The XRD patterns of the CeGd10 powder calcined at 350 and 400 °C in air for 12h are shown in Figure 5.4. Regardless of the calcination temperature $Ce(PO_3)_4$ is found as the main phase. Some additional peaks of low intensity are observed in both cases, but can not be identified with any of the known phases in the system. It is worth noting that in the system Ce-Y-P-O, $Ce(PO_3)_4$ is also formed after calcination at or above 400 °C, but CeP_2O_7 is the main phase even after calcination at 790 °C. The reason for this is associated with the higher P content of the CeGd10 powder as compared to that of the Ce-Y-P-O powders.

5.3.1.3 CeY10+P:KH_2PO_4 composite

The temperature dependence of the CeY10+P:KH_2PO_4 composite is investigated by in-situ XRD in the temperature range 100-250 °C in steps of 25 °C. XRD patterns obtained in-situ at 25, 100, 150 and 200 °C are shown in Figure 5.5. The relative intensity of the KH_2PO_4 (200) reflection (tetragonal, I-42d) decreases with increasing temperature, and is completely absent above 200 °C. On the other hand, the intensity of the (112) reflection increases upon heating to 100 °C, decreases upon further heating, and disappears above 200 °C. This indicates that re-crystallization of KH_2PO_4 takes place upon heating to 100 °C. KH_2PO_4 has a melting point of 250 °C. Therefore the disappearance of the KH_2PO_4 diffraction peaks is not associated with melting. It has been proposed that amorphous $KH_5(PO_4)_2$ forms in SiP_2O_7:KH_2PO_4 composites upon heating above ca. 200 °C.[123] Our findings indicate that amorphous potassium phosphate forms also in the CeY10+P:KH_2PO_4 system, but its composition (KH_2PO_4, $KH_5(PO_4)_2$

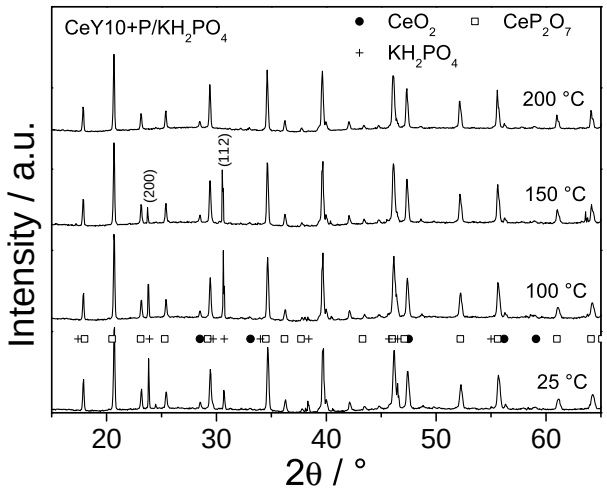

Figure 5.5: In-situ XRD patterns of CeY10+P:KH_2PO_4 composite recorded at 25, 100, 150 and 200 °C in air.

or other) remains unknown. The formation of the amorphous phase takes place at 150-200 °C in the CeY10+P:KH_2PO_4 system. Crystalline KH_2PO_4 or $KH_5(PO_4)_2$ is not observed upon cooling to 25 °C at the end of the experiment.

5.3.2 Thermogravimetry

The mass loss upon heating CeGd10, CeY10+P and CeY10+P:KH_2PO_4 to 100, 150, 200, 250, 300, 500, 700 and 900 °C in dry air is determined by thermogravimetry. As can be seen in Figure 5.6, the mass of CeY10+P remains almost constant up to 300 °C. On the other hand, the mass of CeY10+P:KH_2PO_4 and CeGd10 is reduced in a stepwise manner up to 300 °C. The atmosphere is changed from air to N_2, CO_2, 9 % H_2 in N_2, and back to air during the 5 h long hold at 150 °C, but this does not result in any significant mass change. The amount of H_2O released upon heating the samples is quantified by in-line Mass Spectrometry. As shown in Figure 5.7, the entire mass loss from the samples up to 300 °C is associated with the release of H_2O.

All three compositions lose a significant amount of mass upon heating above 300 °C, reaching a constant value at the isothermal step at 700 °C. From the quantification of the released H_2O, it is seen that compositions CeY10+P and CeY10+P:KH_2PO_4 only lose H_2O up to 700 °C. This is in line with the XRD results and the proposed Reaction 5.1 taking place in the temperature range 350-700 °C. For CeGd10 the amount of released H_2O is significantly less than the total mass loss. The additional mass loss must then be associated with loss of phosphorous oxide. Further mass loss is

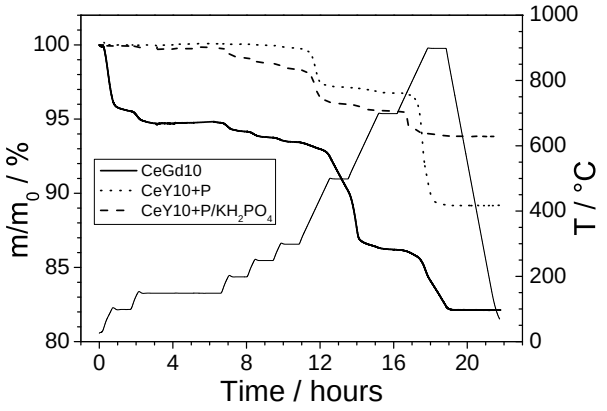

Figure 5.6: Mass of CeGd10, CeY10+P and CeY10+P:KH_2PO_4 relative to their original mass m_0 and corresponding temperature profile.

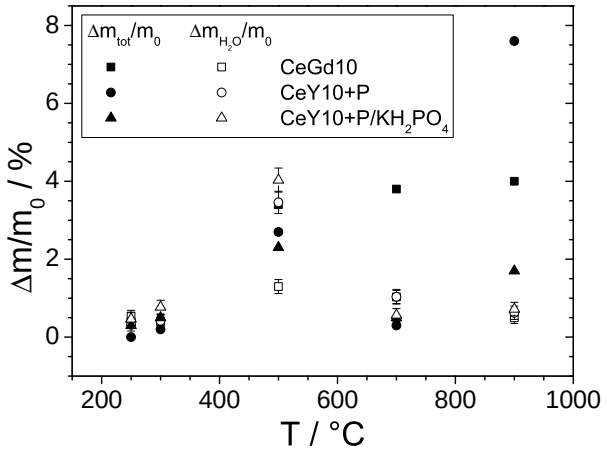

Figure 5.7: Total mass loss and mass loss associated with dehydration of CeGd10, CeY10+P and CeY10+P:KH_2PO_4 relative to their original mass m_0, at each temperature step.

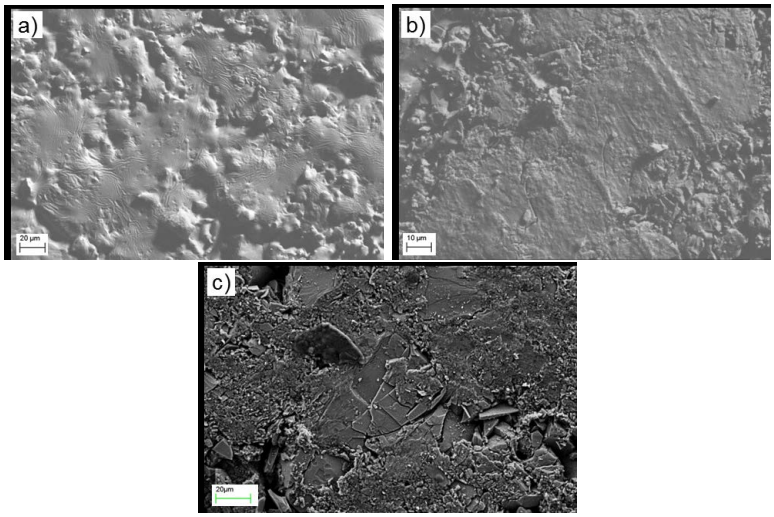

Figure 5.8: Scanning electron micrographs of the surface morphology of pellets pressed from a) as-synthesized CeY10+P, b) CeY10+P annealed at 300 °C, and c) CeGd10 annealed at 400 °C.

observed for all compositions upon heating to 900 °C, associated with loss of phosphorous oxide, in accordance with Reactions 5.2 and 5.3, but also associated with the presence of excess H_3PO_4 in the starting mixture.

5.3.3 Microstructure

SEM images of the surface morphology of pellets pressed from as-synthesized CeY10+P, CeY10+P annealed at 300 °C, and CeGd10 annealed at 400 °C are shown in Figures 5.8a, 5.8b, and 5.8c, respectively. As-synthesized CeY10+P is covered with a layer of viscous fluid as indicated by the rippled appearance of its surface in Figure 5.8a. This is related to the excess H_3PO_4 used in the synthesis procedure resulting in a P-rich amorphous and highly hygroscopic layer covering the surface of the grains. A similar fluid layer is not observed for CeY10+P and CeGd10 annealed at 300 °C and 400 °C, respectively. This must be associated with the dehydration of the P-rich layer upon thermal annealing, as evidenced by the thermogravimetric results.

5.3.4 Conductivity

The conductivity of CeGd10, CeY10+P and CeY10+P:KH_2PO_4 (all having excess H_3PO_4) and its dependence on p_{H_2O} at 100, 150, and 190 °C is shown in Figure 5.9a-c. The relaxation of the conductivity upon changing the p_{H_2O} or p_{O_2} of the atmosphere is plotted as a function of time, in order to i) provide a rough estimate of the time constant of the relaxations, ii)

give an idea of the degree of equilibration, and iii) allow for a comparison of the conductivity achieved under identical conditions after a hydration-dehydration cycle and/or a reduction-oxidation cycle. The CeGd10 powder used for the conductivity measurements has $Ce(PO_3)_4$ as the only crystalline phase, as determined by XRD. On the other hand CeY10+P is calcined at 380 °C for 3 h and consists of CeP_2O_7 as the main crystalline phase and a small amount of CeO_2. A P-rich amorphous secondary phase is also expected to be present in both samples.

As can be seen in Figure 5.9a-c the conductivity of all three samples depends drastically on p_{H_2O}. At 100 °C (Figure 5.9a) it increases by several orders of magnitude when shifting from dry air to air with $p_{H_2O} = 0.1$ atm, reaching $7{\cdot}10^{-3}$, $1.8{\cdot}10^{-4}$ and $5{\cdot}10^{-3}$ S/cm for CeGd10, CeY10+P and CeY10+P:KH_2PO_4 (all having excess H_3PO_4), respectively. It should be noted that by dry air we refer to air that has not been humidified, and corresponds to a p_{H_2O} of less than 10^{-3} atm. Further increasing the humidity to $p_{H_2O} = 0.2$ atm results in only a minor increase in conductivity. After changing the atmosphere to dry air, the conductivity of CeGd10 and CeY10+P decreases by about two orders of magnitude, and that of CeY10+P:KH_2PO_4 by three orders of magnitude. It is observed though that the conductivity under dry conditions is improved by several orders of magnitude, compared to the starting value, after one hydration cycle at 100 °C for all three samples.

The conductivity of all samples increases drastically when shifting from dry to wet air at 150 °C (Figure 5.9b), similar to the situation at 100 °C. The p_{O_2} dependence is rather weak between air and 9 % H_2 in N_2, both under wet and dry conditions. At $p_{H_2O} = 0.2$ atm and $[H_2]/[H_2O] = 0.36$, the conductivity reaches values of $6.4{\cdot}10^{-2}$, $1.9{\cdot}10^{-2}$ and $2.6{\cdot}10^{-2}$ S/cm for CeGd10, CeY10+P and CeY10+P:KH_2PO_4 (all having excess H_3PO_4), respectively. The conductivity values obtained in dry air at 150 °C following the hydration-dehydration and reduction-oxidation cycles are again higher than the original values by about 1 order of magnitude.

A stepwise increase in conductivity is observed at 190 °C in air following the stepwise increase in p_{H_2O} (Figure 5.9c). A significant conductivity increase is found for CeY10+P when shifting from $p_{H_2O} = 0.1$ atm to $p_{H_2O} = 0.2$ atm, which is not observed at 100 °C (Figure 5.9a). The conductivity of CeGd10, CeY10+P and CeY10+P:KH_2PO_4 (all having excess H_3PO_4) reaches values of $3.6{\cdot}10^{-2}$, $7.8{\cdot}10^{-3}$ and $2.4{\cdot}10^{-2}$ S/cm, respectively, at 190 °C in air with $p_{H_2O} = 0.2$ atm. Upon shifting to dry air, the conductivity of CeY10+P remains quite high, $1.3{\cdot}10^{-3}$ S/cm, about 2 orders of magnitude higher than its value prior to the hydration-dehydration cycle. On the other hand, the conductivity of CeGd10 and CeY10+P:KH_2PO_4 decreases by about 2 orders of magnitude and becomes lower than the respective starting value, which is different from the behavior of the samples at 100 and 150 °C.

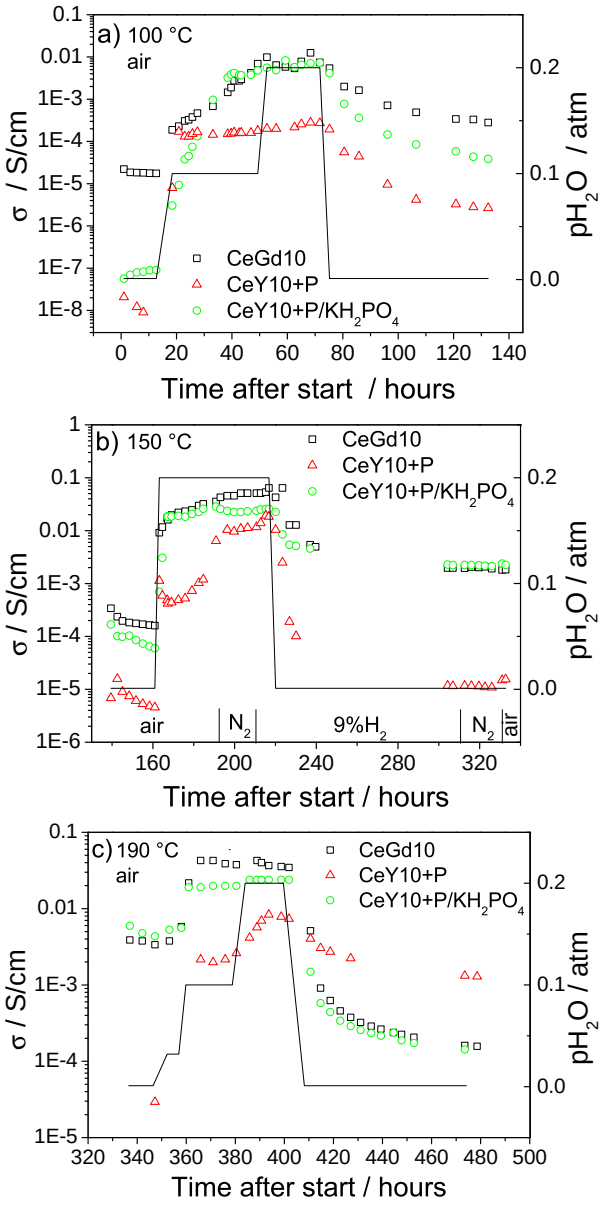

Figure 5.9: Conductivity of CeGd10, CeY10+P and CeY10+P:KH_2PO_4 (all having excess H_3PO_4) as a function of time under varying p_{H_2O} at a) 100, b) 150 and c) 190 °C.

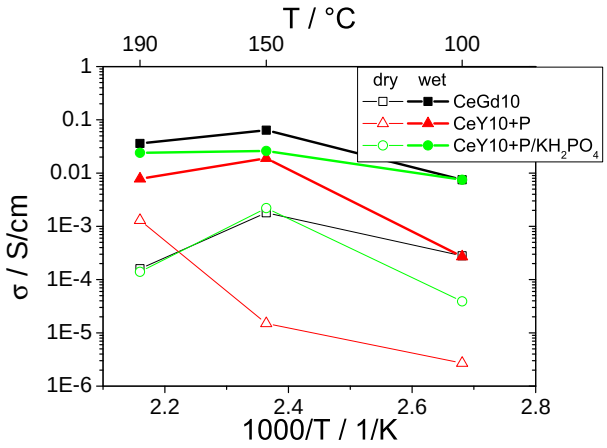

Figure 5.10: Temperature dependence of the conductivity of CeGd10, CeY10+P and CeY10+P:KH_2PO_4 (all having excess H_3PO_4) under dry ($p_{H_2O} < 10^{-3}$ atm) and wet ($p_{H_2O} = 0.2$ atm) conditions.

The temperature dependence of the conductivity of CeGd10, CeY10+P and CeY10+P:KH_2PO_4 (all having excess H_3PO_4) under wet ($p_{H_2O} = 0.2$ atm) and dry ($p_{H_2O} < 10^{-3}$ atm) conditions is shown in Figure 5.10. The conductivity of all samples seems to pass through a broad maximum at around 150 °C under wet conditions. CeGd10 and CeY10+P:KH_2PO_4 follow a similar behavior under dry conditions. CeY10+P on the other hand shows a monotonic increase in conductivity with increasing temperature under dry conditions. It should be noted that the conductivity under dry conditions used in Figure 5.10 corresponds to the value measured at the end of the hydration-dehydration cycle in each case.

In order to better understand the p_{H_2O} dependence of the conductivity and to establish the long term development of the conductivity, a prolonged conductivity measurement is undertaken for CeGd10 and CeY10+P (both having excess H_3PO_4) at 155 °C in N_2 under repeated hydration-dehydration cycles, shown in Figure 5.11. Pronounced p_{H_2O} dependence is again observed for both samples. The conductivity of CeGd10 is about half an order of magnitude lower than what was measured in the experiment presented in Figure 5.9. This may be due to inhomogeneities in the synthesized powder or due to degradation of the stored powder over time, although the powder is found to be single phase $Ce(PO_3)_4$ by XRD. The response of CeGd10 towards hydration is relatively fast compared to its response towards dehydration which is surprisingly slow, lasting over 450 h. The magnitude of the relaxation time for dehydration indicates that the phase composition and microstructure may be changing during the relaxation under dry conditions. This will be further discussed in the following subsection where a post-mortem XRD analysis is presented. It is interesting to note that the relaxation time for

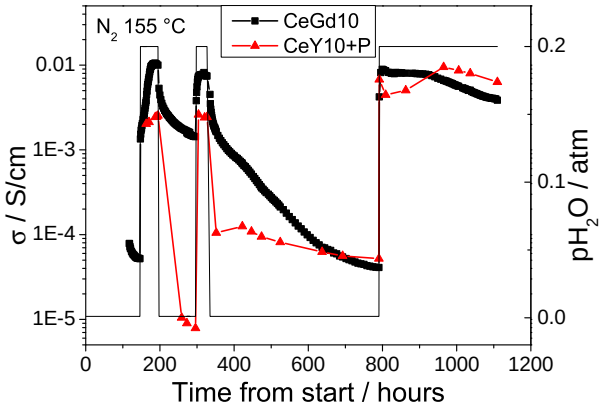

Figure 5.11: Long term conductivity of CeGd10 and CeY10+P (both having excess H_3PO_4) at 155 °C in N_2 under repeated hydration-dehydration cycles.

hydration becomes smaller after every hydration-dehydration cycle. At the end of the second hydration (320 h after start) the conductivity of CeGd10 (with excess H_3PO_4) is 20 % lower than that after the first hydration (190 h after start). When the sample is hydrated for a third time (820 h after start), a similar conductivity is achieved as during the second hydration, and it remains stable under wet conditions for a period of about 100 h. Pronounced decrease in conductivity, amounting to 50 %, is observed during the last 100 h of the measurement though that takes place under wet conditions.

The conductivity of CeY10+P (with excess H_3PO_4) is also significantly lower, by about 1 order of magnitude, than what was measured in the experiment presented in Figure 5.9, although no phase change is witnessed by XRD. The response of CeY10+P towards hydration and dehydration is similarly fast. Although a sluggish decrease in conductivity is observed to take place during the second dehydration of the sample, its value remains almost one order of magnitude higher than that at the end of the first dehydration. A similar improvement is observed in the conductivity of CeY10+P measured during the final hydration as compared to that obtained in the first hydration. Finally, as is the case for CeGd10, the conductivity of CeY10+P is also found to decrease during the last 100 h of the last hydration. Nevertheless, its conductivity value at the end of the experiment remains more than 150 % improved compared to its value at the first or second hydration.

5.3.5 Post mortem analysis

The phase composition of CeY10+P and CeGd10 samples after the long term conductivity measurement presented in Figure 5.11 is examined by XRD. Before testing, CeY10+P consists primarily of CeP_2O_7 along with a small amount of CeO_2, and CeGd10 is pure phase $Ce(PO_3)_4$. As can be seen in Figure 5.12, both samples consist mainly of $CePO_4$ at the end of the

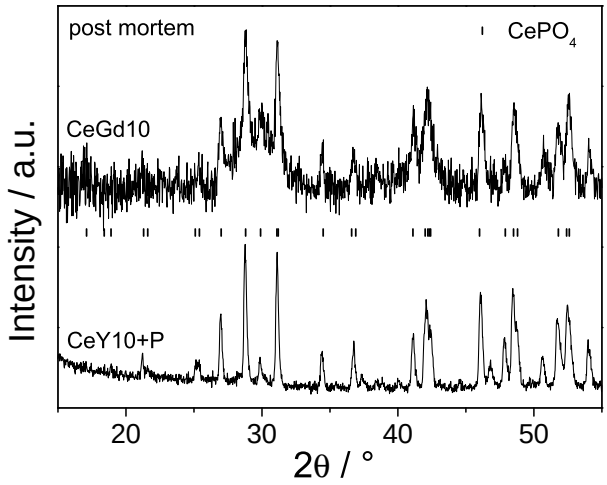

Figure 5.12: XRD patterns of CeY10+P and CeGd10 samples recorded after the long term conductivity measurement presented in Figure 5.11.

long term conductivity experiment. No additional phases can be detected by XRD, but traces of secondary phases hidden in the background noise of the CeGd10 XRD cannot be excluded. The high noise to signal ratio of the XRD pattern of CeGd10 is associated with a very large background signal that is subtracted for reasons of clarity, and most probably related to the presence of an amorphous secondary phase.

CeY10+P and particularly CeGd10 are very hygroscopic after the long term conductivity measurement and form a paste by absorbing steam from the atmosphere. The transformation of CeP_2O_7 and $Ce(PO_3)_4$ to $CePO_4$ is expected to be accompanied by the formation of P_mO_n, which absorbs water to form an aqueous solution. Indeed, mixing the samples with water and stirring yielded very acidic solutions, confirming the formation of an aqueous solution of H_3PO_4.

5.4 Discussion

5.4.1 Phase stability

The phase composition in the Ce-Y-P-O and Ce-Gd-P-O systems is examined at various P/(Ce+Y) or P/(Ce+Gd) ratios and temperatures with ex-situ and in-situ XRD, and by thermogravimetry combined with in-line mass spectrometry. For P/(Ce+Y) ratios of 2.6 to 3.1, CeP_2O_7 is the main phase forming up to 790 °C, whereas $Ce(PO_3)_4$ is the only phase found up to 400 °C for a P/(Ce+Gd) ratio of 5. For P/(Ce+Y) ratios of 2.6 to 3.1, CeP_2O_7 is found to react partly with excess H_3PO_4 forming $Ce(PO_3)_4$ at temperatures above 400 °C. The amount of $Ce(PO_3)_4$ is found to increase

with increasing temperature up to 500 °C, whereas above 700 °C $Ce(PO_3)_4$ is found to decompose to $Ce(PO_3)_3$ and $CePO_4$. According to Sun *et al.*,[69] CeP_2O_7 transforms to $Ce(PO_3)_4$ at 455 °C according to Reaction 5.4. In this study, $Ce(PO_3)_4$ is found to form already at 400 °C, but following Reaction 5.1, which may explain the lower temperature of formation found in this case. Onoda *et al.*[88] also report decomposition of CeP_2O_7 to $Ce(PO_3)_3$ and $CePO_4$ above 825 °C, in agreement with our findings.

Le *et al.*[76] report formation of $Ce(PO_3)_3$ at 450 °C, as well as traces of $Ce(PO_3)_4$ and $CePO_4$. The amount of $Ce(PO_3)_3$ increases upon heating to 750 °C, and becomes the main phase at 900 °C with $CePO_4$ as a secondary phase, at which temperature the starting CeP_2O_7 phase is completely decomposed. White *et al.*[89] study the thermal decomposition of $Ce(HPO_4)_2{\cdot}xH_2O$, which is found to transform to CeP_2O_7 within the temperature range 300-600 °C, and consequently to $Ce(PO_3)_3$ and $CePO_4$ upon annealing at temperatures above 725 °C. These findings are in line with our observation that $Ce(PO_3)_3$ and $CePO_4$ form at temperatures above 700 °C. In our study though, and in the work of Sun *et al.*,[69] CeP_2O_7 is found to transform to $Ce(PO_3)_4$ first, which is not observed by Le *et al.*,[76] by White *et al.*[89] or by Onoda *et al.*[88] The reason for this discrepancy and for the scatter in reported phase transition temperatures is not clear, but it is most probably related to varying P content of the starting powders, annealing times and heating rates, as well as varying rates of P loss during thermal annealing due to varying gas flow rates, amount of starting powder, humidity and means of protecting the powder from P loss.

Tsuhako *et al.*[124] investigate the dependence of the P/Ce ratio on the phase composition at different temperatures. At temperatures below 500 °C, CeP_2O_7 is the main phase for P/Ce = 1 - 4, whereas $Ce(PO_3)_4$ is the main phase for P/Ce > 4 and the sole phase for P/Ce = 6 - 8. At 700 °C, $CePO_4$, CeP_2O_7, $Ce(PO_3)_4$, and CeP_5O_{14} are the compounds predominantly formed at P/Ce ratios of about 1, 2, 2 - 6, and above 10, respectively. Tsuhako *et al.*[124] also observe formation of $Ce(PO_3)_3$ at a temperature of 800 °C or higher. These findings are in line with our work presented here. Masui *et al.*[125] examine the thermal decomposition of amorphous Ce phosphate with P/Ce ratio of 1.5. They report formation of primarily CeP_2O_7 at 500 °C, which transforms to $CePO_4$ upon heating to 900 °C, in agreement with the findings by Tsuhako *et al.*[124]

Drastic phase changes are observed in 10 mol % Y doped CeP_2O_7 and 10 mol % Gd doped $Ce(PO_3)_4$ following long term annealing at 155 °C under varying p_{H_2O}. $CePO_4$ is the only crystalline phase present in either sample after ca. 1100 h of annealing. The samples are very hydrophilic and form a thick paste after being exposed to the humidity of the atmosphere at ambient temperature, indicating the presence of an amorphous P-rich secondary phase. Therefore the phase transition from CeP_2O_7 or $Ce(PO_3)_4$ to $CePO_4$ is not driven by the loss of P from the samples by e.g. evaporation,

since an amorphous P-rich secondary phase is present in the samples after decomposition.

5.4.2 Conductivity

The conductivity of 10 mol % Gd doped $Ce(PO_3)_4$ (CeGd10), containing excess H_3PO_4, is found to reach a value of $6.4 \cdot 10^{-2}$ S/cm at 150 °C under wet conditions (p_{H_2O} = 0.2 atm). This is the highest value ever reported for a Ce based phosphate composite, followed by a value of about $2 \cdot 10^{-2}$ S/cm for undoped CeP_2O_7 under similar conditions,[76] which coincides with the conductivity of 10 mol % Y doped CeP_2O_7 (CeY10+P) measured in this work. A similar value of about 10^{-2} S/cm has been reported by Sun *et al.*[69] for undoped CeP_2O_7 in air with 3.2 % H_2O. The conductivity of CeGd10 is 2-3 times lower than that of 10 mol % In doped SnP_2O_7,[68] the best conducting pyrophosphate reported up to date to the best of our knowledge.

The conductivity of all samples investigated here shows strong p_{H_2O} dependence. For CeGd10 and CeY10+P:KH_2PO_4 it passes through a broad maximum at around 150 °C under wet (p_{H_2O} = 0.2 atm) or dry ($p_{H_2O} < 10^{-3}$ atm) conditions. This is attributed to the thermally activated mobility of the protons combined with a decreasing concentration of charge carriers with increasing temperature (thermally induced dehydration).

CeY10+P on the other hand passes through a maximum under wet conditions, but shows a monotonic increase in conductivity with increasing temperature under dry conditions. This is most probably associated with a phase change from CeP_2O_7 to $CePO_4$, accompanied by the release of P_mO_n and an increase in conductivity, as evidenced by the post mortem analysis of the long term conductivity samples. This may also be the reason for the increased conductivity under dry conditions generally observed after a hydration-dehydration cycle.

Furthermore, it is worth noting that the conductivities of CeGd10 and CeY10+P acquire very similar values, both under dry and wet conditions, after about 600 h of measurement at 155 °C. This is not surprising, since towards the end of the experiment both samples consist of $CePO_4$ and an amorphous hygroscopic phase, presumably hydrated P_mO_n, according to the post mortem analysis. $CePO_4$ is known to possess a conductivity of less than 10^{-6} S/cm in p_{O_2} = 0.01 atm at 155 °C, and to be rather insensitive on p_{H_2O}.[119] This is very different from the behavior of the CeGd10 and CeY10+P samples, the transport properties of which must therefore be attributed to the amorphous hygroscopic phase that is distributed among the $CePO_4$ particles.

The conductivity of both CeGd10 and CeY10+P decreases during the last 100 h of the long term measurement, taking place in p_{H_2O} = 0.2 atm. The reason for this is most probably related to gradual loss of P_mO_n due to

evaporation or slow rearrangement of the glassy phase within the samples. The conductivity of CeGd10 during the first hydration of the long term experiment has its highest value, despite the fact that P_mO_n exsolves from $Ce(PO_3)_4$ and therefore the fraction of the highly conducting amorphous phase at the grain boundaries increases. This indicates that 10 mol % Gd doped $Ce(PO_3)_4$ may indeed possess high proton conductivity. Onoda *et al.*[120] have reported a value of about 10^{-6} S/cm at 400 °C in air with 4.2 % H_2O for the conductivity of $Ce(PO_3)_4$ doped with 1 mol % Gd, but this large difference may be associated with the higher calcination temperature, the higher measuring temperature, lower p_{H_2O}, and lower degree of doping used by Onoda *et al.*[120]

Excess P_mO_n at the grain boundaries has been suggested by various groups[78,91,92,101,126] to be the reason behind the high proton conductivities reported for some pyrophosphates, as this could explain the many orders of magnitude difference in conductivity determined for nominally similar compositions. There is consensus as to the fact that the calcination and sintering temperatures can significantly affect the transport properties due to loss of P.[68,76,81,100,101] Two studies that have attempted to vary and quantify the metal to P ratio by X-Ray fluorescence (XRF),[68,100] suggest that P deficiency can seriously harm the conductivity, whereas P excess has a small influence. For accurate quantification of the XRF signal though, appropriate calibration standards are necessary in order to account for interactions of the X-Rays with the matrix. The details of the quantification procedure are not disclosed in any of these studies, and therefore this conclusion is ambiguous. In fact, it has been shown that the addition of only 0.7 mol % excess H_3PO_4 can increase the conductivity of $Al(H_2PO_4)_3$ by three orders of magnitude.[127] This level of precision cannot be achieved by XRF even if it is most optimally calibrated.

Chen *et al.*[71] do not observe a change in the conductivity of 10 mol % In doped SnP_2O_7 after washing the material with water, which should help remove excess P_mO_n. It is doubtful though whether simple washing can safely be assumed to remove a thin P containing glassy layer if this is well adhered on the grain surface. Another argument favoring the bulk origin of the high conductivity in pyrophosphates is based on the different conductivity value measured in cubic, layered and amorphous SnP_2O_7.[68] These samples are synthesized following different procedures and thermal treatments though, which is known to critically affect performance. In fact much larger differences in conductivity are reported for pyrophosphates having the same nominal composition and crystal structure.

TEM visualization of a SnP_2O_7 powder, prepared by coprecipitation and calcined at a temperature as high as 800 °C, reveals crystalline phosphate particles fully covered with a continuous amorphous shell film.[94] Since powders that show high conductivity are sintered at temperatures below 800 °C, it is reasonable to expect that they also possess a similar amorphous shell.

Combining this critical review of the literature with the experimental results presented here, it is concluded that the high conductivity that is sometimes observed in pyrophosphates is most probably associated with the formation of a core-shell structure, with a highly conducting P-rich glassy shell. Furthermore, our long term conductivity results indicate that P_mO_n tends to exsolve from the structure of 10 mol % Y doped CeP_2O_7 or 10 mol % Gd doped $Ce(PO_3)_4$, further enriching the P_mO_n shell.

The conductivity of the CeY10+P:KH_2PO_4 composite follows a very similar behavior as that reported for SiP_2O_7:KH_2PO_4[123] and shows very similar conductivity values, reaching $2.6{\cdot}10^{-2}$ S/cm at 150 °C in air with 20 % H_2O. The high conductivity is associated with the re-crystallization of KH_2PO_4 and formation of amorphous potassium phosphate at temperatures above 100 °C. Crystalline KH_2PO_4 or $KH_5(PO_4)_2$ is not observed upon cooling to 25 °C at the end of the experiment, as is also the case in the SiP_2O_7:KH_2PO_4 system.[123]

5.5 Conclusions

The phase composition in the Ce-Y-P-O and Ce-Gd-P-O systems depends critically on the P to metal ratio, the annealing temperature, humidity and time. For P/(Ce+Y) ratios of 2.6 to 3.1, CeP_2O_7 is the main phase up to 790 °C. CeP_2O_7 reacts partly with excess H_3PO_4 forming $Ce(PO_3)_4$ at temperatures above 400 °C, whereas above 790 °C $Ce(PO_3)_4$ decomposes to $Ce(PO_3)_3$ and $CePO_4$. For a P/(Ce+Gd) ratio of 5 $Ce(PO_3)_4$ is the only crystalline phase found up to 400 °C. After 1100 h of annealing at 155 °C under varying humidity between $p_{H_2O} < 10^{-3}$ atm and $p_{H_2O} = 0.2$ atm, CeP_2O_7 and $Ce(PO_3)_4$ doped with 10 mol % Y and Gd, respectively, are completely decomposed to $CePO_4$.

The conductivity of 10 mol % Y doped CeP_2O_7 and 10 mol % Gd doped $Ce(PO_3)_4$ with excess H_3PO_4 depends drastically on p_{H_2O} but is rather insensitive on p_{O_2}. A value of $6.4{\cdot}10^{-2}$ S/cm is achieved by 10 mol % Gd doped $Ce(PO_3)_4$ (with excess H_3PO_4) at 150 °C and $p_{H_2O} = 0.2$ atm. Under the same conditions, 10 mol % Y doped CeP_2O_7 (with excess H_3PO_4) reaches a value of $1.9{\cdot}10^{-2}$ S/cm. The conductivity of both samples passes through a broad maximum at around 150 °C. This behavior is indicative of thermally activated proton mobility along with thermally induced dehydration.

The long term stability of the conductivity upon repeated hydration-dehydration cycles is examined here for the first time on pyrophosphates and polyphosphates. Although both 10 mol % Y doped CeP_2O_7 and 10 mol % Gd doped $Ce(PO_3)_4$ are completely decomposed to $CePO_4$ after 1100 h at 155 °C, their conductivities are not drastically modified. It is concluded that exsolution of P_mO_n that takes place along with the phase transformation to $CePO_4$, significantly affects the conductivity of the samples.

KH_2PO_4 is found to re-crystallize and to form amorphous potassium phosphate at temperatures above 100 °C in a composite of 10 mol % Y doped CeP_2O_7:KH_2PO_4 having excess H_3PO_4, resulting in a conductivity value of $2.6 \cdot 10^{-2}$ S/cm at 150 °C and $p_{H_2O} = 0.2$ atm.

Chapter 6

High-temperature solid state proton conductors

The study of pyrophosphates does not provide a clear electrolyte candidate, therefore solid state proton conductors, a well established class of proton conducting materials, are considered. This chapter gives first a general description and then the defect concentrations and partial conductivities of Y-doped $BaCeO_3$-$BaZrO_3$ solid solutions are calculated for different temperatures, p_{H_2O} and chemical compositions.

6.1 Overview

Proton conductivity in oxides at high temperature (T > 500 °C) was first reported in the 1980s by Iwahara *et al.* for Sr and Ba cerates.[128–131] Since then, a great amount of work has been carried out by the scientific community on perovskite-structured cerates and zirconates, and the progress has been presented in a number of reviews.[98,132–136]

Perovskite oxides have the general formula ABO_3, where the A cation (valence 2+) is coordinated with twelve oxygen ions, while the B cation (valence 4+) occupies a six-coordinate site and forms a network of corner-sharing BO_6 octahedra.

Protons are not part of the nominal structure of these materials, but are introduced as defects upon equilibrium with a source gas containing water vapour. When water vapour adsorbs on the material it dissociates and Reaction 6.1 takes place:

$$H_2O_{(g)} + V_O^{\bullet\bullet} + O_O^{\times} \leftrightarrow 2\,OH_O^{\bullet} \tag{6.1}$$

Alternatively the hydroxyl ion $OH_O^{\bullet}$ may be denoted as an interstitial proton $H_i^{\bullet}$. However, it must be pointed out that the proton is not free, but is bound to oxide ions.[137] Since the hydration Reaction 6.1 is exothermic for

doped and undoped cerates and zirconates,[135] the proton uptake is higher at low temperatures.

Undoped perovskites, such as $SrCeO_3$, $SrZrO_3$, $BaCeO_3$, $CaZrO_3$ and $BaZrO_3$, have very low proton concentrations because of the low intrinsic vacancy concentration. Substituting the B cation with a lower valence cation (e.g. Zr^{4+} with Y^{3+}) introduces oxygen vacancies as shown by Reaction 6.2:

$$2\,Zr_{Zr}^{\times} + Y_2O_3 + O_O^{\times} \rightarrow 2\,Y_{Zr}^{'} + V_O^{\bullet\bullet} + 2\,ZrO_2 \tag{6.2}$$

The resulting vacancy concentration is:

$$[V_O^{\bullet\bullet}] = \frac{1}{2}\left[Y_{Zr}^{'}\right] \tag{6.3}$$

The higher concentration of vacancies allows a higher proton concentration, and the the conductivity increases since it is proportional to it.

The movement of the proton within the material occurs by proton hopping between oxygen ions (Grotthuss mechanism).[138] This process occurs in two steps: the rotational movement of the proton around an oxygen ion, and the transfer of the proton to a neighboring oxygen ion.[139]

Over the years a number of elements have been added as dopants (Yb, Y, Sc, Mg, In, Zn, Nd, Sm, Dy, Al, Ga)[128–131,140–142] with doping levels between 5 and 20 %. Iwahara *et al.*[141] report that Y-doping provides the highest total conductivity (see Figure 6.1) in "hydrogen-containing atmosphere", i.e. wet atmosphere in my opinion. It is worth noticing that, as will be illustrated in Section 6.2, on top of proton conductivity these materials have significant oxide ion conductivity above 600 °C.

In general, it is widely accepted in the literature that the best conductivity is obtained for Y-doped $BaCeO_3$, but unfortunately cerates have poor chemical stability. In fact $BaCeO_3$ reacts with CO_2 to form $BaCO_3$ and CeO_2[143] and with high partial pressures of H_2O to form CeO_2 and $Ba(OH)_2$.[144] The reactivity toward CO_2 hinders the use of air as oxidant gas and/or of hydrocarbons as fuel, since CO_2 is present in both of them.[132] Moreover, water is present during fuel cell operations, since it is produced on the cathode side. The instability of $BaCeO_3$ has been attributed to its high basicity, which from another perspective is beneficial since it helps stabilize the protonic defects.[135,145]

Y-doped $BaZrO_3$ (BZY) is instead stable in fuel cell operation conditions, but its total conductivity is about 1 order of magnitude lower than the conductivity of Y-doped $BaCeO_3$.[146] Impedance spectroscopy measurements carried out at operating temperature for proton conducting fuel cells (i.e. above 600 °C) permit to measure only the total conductivity of the electrolyte, but Kreuer investigated the conductivity by impedance spectroscopy below 150 °C, proving that $BaZrO_3$ has a bulk conductivity higher than $BaCeO_3$.[135,147] The low total conductivity measured for polycrystalline

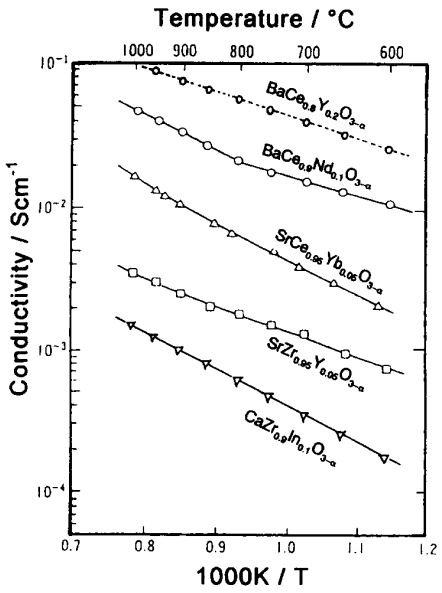

Figure 6.1: Conductivities of different proton conducting perovskites in hydrogen-containing atmosphere. Figure reproduced from Iwahara *et al.*[141]

samples is attributed to a combination of poor sinterability and low grain boundary conductivity of $BaZrO_3$. The poor sinterability hinders the grain growth during sintering, and small grain size implies a large volume fraction of grain boundaries, whose high resistivity reduces the total conductivity of the oxide. The microstructure of the material is therefore of pivotal importance for conductivity: at 600 °C the conductivity of $BaZr_{0.8}Y_{0.2}O_{2.9}$ (BZY20) increases of 1 order of magnitude upon a change in grain size from 500 nm to 1 µm.[132] The sensitivity of conductivity to microstructure (and thus to processing routes) may explain the significant discrepancies among the total conductivities reported in the literature.[146]

In order to obtain high-density $BaZrO_3$ different strategies have been used, such as sintering above 1600 °C[148] or by spark plasma sintering (SPS),[149,150] using ultrafine powders produced by wet chemical routes[132,151,152] and adding sintering aids.[153–156]

However, high sintering temperatures induce BaO vaporisation that leads to a decrease in conductivity: in order to avoid that it is necessary to sinter $BaZrO_3$ in presence of excess barium.[148] Many additives meant as sintering aids, such as TiO_2, MgO, Mo, Al_2O_3, Bi_2O_3 and SnO_2, do not improve densification and decrease the conductivity.[155] ZnO improves the densification but lowers the conductivity, likely because Zn^{2+} ions substitute Zr^{4+} in the lattice acting as proton traps and decreasing the concentration of protons able to migrate.[156] The addition of 1 wt% of NiO permits instead to obtain 98 % dense $BaZr_{0.9}Y_{0.1}O_{3-\delta}$ (BZY10) with an average grain size of 1.3 µm

after reactive sintering at 1500 °C: its conductivity is $1.53 \cdot 10^{-3}$ S/cm at 600 °C in 9 % H_2 in N_2 (p_{H_2O} = 0.015 atm).[153]

Solid solutions of Y-doped $BaCeO_3$ and $BaZrO_3$, i.e. $BaCe_xZr_{1-x-y}Y_yO_{3-\delta}$ (BCZY), have been studied extensively in order to combine good chemical stability with high proton conductivity.[135,153,157,158] As expected, increasing Zr content reduces the conductivity of BCZY[153,157] and increases stability in CO_2,[157] i.e. the solid solutions have intermediate properties. Moreover, adding cerium to $BaZrO_3$ increases its toughness and reduces the degradation upon thermal cycling.[135]

6.2 Conductivity and defect chemistry of Y-doped $BaCeO_3$-$BaZrO_3$ solid solutions (BCZY)

It has been reported in Section 6.1 that BCZY is the most promising proton conducting perovskite for proton conducting fuel cells (PCFCs).

The properties of the material are dependent on the chemical composition of the BCZY solid solutions: both the ratio between Ce and Zr and the level of Y doping affect the concentration and mobility of defects.

The conductivity of BCZY solid solutions is, as expected, intermediate between the conductivities of BCY and BZY. An example is shown in Figure 6.2: the conductivity increases with an increase in Ce content of the material.

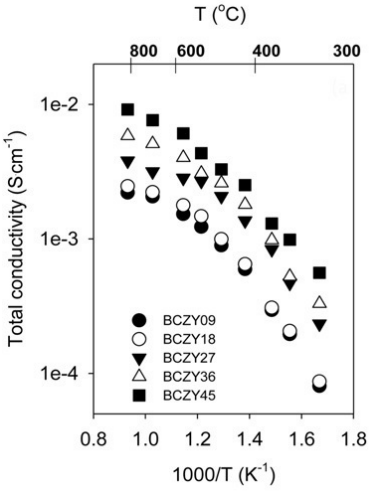

Figure 6.2: Total conductivity of BCZY in 9 % H_2 in N_2 (p_{H_2O} = 0.015 atm) as a function of temperature. Sample compositions: $BaZr_{0.9}Y_{0.1}O_{3-\delta}$ (BCZY09), $BaCe_{0.1}Zr_{0.8}Y_{0.1}O_{3-\delta}$ (BCZY18), $BaCe_{0.2}Zr_{0.7}Y_{0.1}O_{3-\delta}$ (BCZY27), $BaCe_{0.3}Zr_{0.6}Y_{0.1}O_{3-\delta}$ (BCZY36), $BaCe_{0.4}Zr_{0.5}Y_{0.1}O_{3-\delta}$ (BCZY45). Figure reproduced from Ricote *et al.*[153]

The total conductivity of the material is of course the sum of ionic conductivity (protonic and oxygen-ion) and electronic conductivity (p-type and

n-type): the relative importance of each of these contributions is a function of chemical composition, temperature, gas atmosphere, oxygen and water partial pressures.

It is important to know which contributions are significant under the operating conditions of a device, such as a PCFC. In order to calculate the concentration of defects and estimate the conductivity, numerical methods have been used.[159,160]

In the present thesis the concentration of defects and the partial conductivities for $BaCe_{0.2}Zr_{0.6}Y_{0.2}O_{2.9}$ (BCZY26) are calculated at different humidities and temperatures as a function of p_{O_2} with the method described by Poulsen.[159] The calculations are carried out using an Excel spreadsheet developed by Dr. F. W. Poulsen during his time at the Risø National Laboratory for Sustainable Energy.

In order to fully describe the system 10 equations are necessary:

1. Site balance on the A-site of the ABO_3 perovskite:

$$\left[Ba_A^{\times}\right] + \left[V_A^{''}\right] = 1 \tag{6.4}$$

2. Site balance on the B-site. $\left[B_B^{\times}\right]$ is defined as $\left[Zr_B^{\times}\right] + \left[Ce_B^{\times}\right]$, i.e. the total concentration of tetravalent B-site cations (Ce or Zr) is considered, without distinguishing between them:

$$\left[B_B^{\times}\right] + \left[Y_B^{'}\right] + \left[V_B^{''''}\right] = 1 \tag{6.5}$$

3. Site balance on the oxygen site:

$$[V_O^{\bullet\bullet}] + \left[O_O^{\times}\right] + [OH_O^{\bullet}] = 3 \tag{6.6}$$

4. The doping level x is related to the ratio between cations concentrations on the B-site:

$$\frac{\left[B_B^{\times}\right]}{[Y_B^{'}]} = (1-x)/x \tag{6.7}$$

5. The A/B cation ratio z is fixed:

$$A/B\ ratio \equiv \frac{\left[Ba_A^{\times}\right]}{\left(\left[B_B^{\times}\right] + [Y_B^{'}]\right)} = z \tag{6.8}$$

6. Electroneutrality condition (n and p are the concentrations of electrons and holes respectively):

$$2 \cdot \left[V_A^{''}\right] + \left[Y_B^{'}\right] + 4 \cdot \left[V_B^{''''}\right] + n = 2 \cdot [V_O^{\bullet\bullet}] + [OH_O^{\bullet}] + p \tag{6.9}$$

7. The equilibrium of the Schottky reaction (vacancy generation):

$$nil \leftrightarrow 3V_O^{\bullet\bullet} + V_A^{''} + V_B^{''''} \tag{6.10}$$

$$K_s = [V_O^{\bullet\bullet}]^3 \cdot \left[V_A^{''}\right] \cdot \left[V_B^{''''}\right] \tag{6.11}$$

8. The internal electronic equilibrium:

$$K_i = n \cdot p \tag{6.12}$$

9. The equilibrium of the hole formation reaction:

$$\frac{1}{2}\, O_{2(g)} + V_O^{\bullet\bullet} \leftrightarrow O_O^{\times} + 2h^{\bullet} \tag{6.13}$$

$$K_{ox} = \frac{\left[O_O^{\times}\right] \cdot p^2}{p_{O_2}^{1/2} \cdot [V_O^{\bullet\bullet}]} \tag{6.14}$$

10. The equilibrium of the hydration reaction:

$$H_2O_{(g)} + V_O^{\bullet\bullet} + O_O^{\times} \leftrightarrow 2\, OH_O^{\bullet} \tag{6.15}$$

$$K_w = \frac{[OH_O^{\bullet}]^2}{p_{H_2O} \cdot [V_O^{\bullet\bullet}] \cdot \left[O_O^{\times}\right]} \tag{6.16}$$

Theoretically, protons could be incorporated from hydrogen, according to Reaction 6.17:

$$H_{2(g)} + 2\, O_O^{\times} \leftrightarrow 2\, OH_O^{\bullet} + 2e^{'} \tag{6.17}$$

However, Ricote *et al.*[161] ruled out this possibility by studying the proton content of BCZY by Secondary Ion Mass Spectrometry (SIMS) after sintering and after heat treatment in dry or wet H_2 at 600 °C. They report that while BCZY incorporates protons during the sintering in air (water vapour is inevitably present in air), no additional proton loading takes place during the exposure to dry H_2 at 600 °C. This confirms that hydration is described by Reaction 6.15; Reaction 6.17 takes place only if electrodes are present to collect the electrons generated by the reaction (e.g. at the anode of a PCFC).

To calculate all the defect concentrations the doping level x, the A/B ratio z, the four equilibrium constants (K_s, K_i, K_{ox}, K_w) and p_{H_2O} are fixed. To further calculate the partial conductivities, the mobilities are evaluated from values of diffusion coefficients. For the calculations on BCZY26 the

Table 6.1: Input parameters for calculations on BCZY26 at 600 °C and 400 °C.

Description	Symbol	At 600 °C	At 400 °C	Ref.
Doping level	x	0.2	0.2	
A/B ratio	z	1	1	
Eq. constant for vacancy generation	K_s	10^{-20}	10^{-20}	159
Eq. constant for electronic equilibrium	K_i	10^{-11}	10^{-11}	159,163
Eq. constant for hole formation ($atm^{-1/2}$)	K_{ox}	$1.5{\cdot}10^{-5}$	$1.5{\cdot}10^{-5}$	159
Eq. constant for proton formation (atm^{-1})	K_w	3.4	318	162
Mobility of protons ($cm^2{\cdot}s^{-1}{\cdot}V^{-1}$)	m_{OH}	$1.06{\cdot}10^{-5}$	$1.52{\cdot}10^{-6}$	162
Mobility of vacancies ($cm^2{\cdot}s^{-1}{\cdot}V^{-1}$)	m_V	$1.74{\cdot}10^{-7}$	$4.55{\cdot}10^{-9}$	162
Mobility of electrons ($cm^2{\cdot}s^{-1}{\cdot}V^{-1}$)	m_n	$1.06{\cdot}10^{-5}$	$1.52{\cdot}10^{-6}$	
Mobility of holes ($cm^2{\cdot}s^{-1}{\cdot}V^{-1}$)	m_p	$1.06{\cdot}10^{-5}$	$1.52{\cdot}10^{-6}$	

parameters listed in Table 6.1 are used. The value of the equilibrium constant for proton formation is calculated from the enthalpy and entropy of hydration for BCZY26 ($\Delta H^\circ = -111$ kJ·mol^{-1}, $\Delta S^\circ = -117$ J·mol^{-1}·K^{-1}) measured by Coors.[162]

Figure 6.3 shows defect concentrations and partial conductivities at 600 °C calculated for three different water partial pressures (p_{H_2O} = 0.1, 0.01, 0.0001 atm) over a wide range of oxygen partial pressure ($p_{O_2} = 10^{-30}$ - 10^{2} atm).

Decreasing the water partial pressure increases the concentration of oxygen vacancies $[V_O^{\bullet\bullet}]$ and lowers the proton concentration $[OH_O^{\bullet}]$ over all the p_{O_2} range: protons are the main defects present at p_{H_2O} = 0.1 atm while vacancy concentration is higher at p_{H_2O} = 0.0001 atm. This change in defect concentration induces a significant decrease in the total conductivity.

A higher concentration of vacancies does not automatically imply that oxygen ions dominate the conductivity, since conductivity is a function of both concentration and mobility of the charge carriers. From diffusion coefficients data for $[OH_O^{\bullet}]$ and $[V_O^{\bullet\bullet}]$ reported by Coors[162] it is here calculated that the m_{OH}/m_V ratio between their respective mobilities is circa 60 at 600 °C, therefore the oxide-ion conductivity is much smaller than the proton conductivity (see Figure 6.3) at p_{H_2O} = 0.1, 0.01 atm. Only at very low water partial pressures such as p_{H_2O} = 0.0001 atm it can contribute significantly to the total conductivity.

Concentrations of electrons and holes (n and p) are only semi-quantitative since accurate values for K_i and K_{ox} are not available. Moreover, there are almost no mobility / diffusion coefficient data for electrons and holes in the literature (apart from one work on BCY10[164]), therefore in the calculations the mobility of electrons and holes has been put equal to the mobility of the protons when data are not available. In general, the contribution of electronic carriers to the conductivity is expected to be significant only in

very reducing or oxidizing conditions, such as in dry H_2 or in pure O_2. In these conditions the relative magnitude of the mobilities of the carriers determines which one dominates the conductivity, as reported also by Bonanos and Poulsen.[160]

In order to study the effect of temperature on the concentration (and partial conductivities), the same simulation was carried out for T = 400 °C (see Figure 6.4). Lowering the temperature by 200 °C lowers the total conductivity, increases $[OH_O^{\bullet}]$ and reduces $[V_O^{\bullet\bullet}]$ at all water partial pressures. Notice that the contribution of oxygen ions to the conductivity decreases significantly at p_{H_2O} = 0.001 atm. Therefore, operating well below 600 °C ensures that, despite having a lower total conductivity, the oxide-ion conductivity is negligible at all humidities. In general it has been reported that the transport number of protons decreases with increasing temperature, both in reducing and oxidizing atmosphere,[164,165] while oxide-ion conductivity increases. Concerning electronic conductivity, the same reasoning previously used applies: the contribution of n/p conductivity depends on the relative magnitude of the mobilities of electrons/holes and protons.

Finally, to show the effect of the chemical composition on the defect chemistry, the simulation is carried out for $BaCe_{0.9}Y_{0.1}O_{3-\delta}$ (BCY10) and $BaZr_{0.9}Y_{0.1}O_{3-\delta}$ (BZY10) at 600 °C. The concentration and conductivity profiles are presented in Figure 6.5 and the parameters are reported in Table 6.2.

Table 6.2: Input parameters for simulations on BCY10 and BZY10 at 600 °C.

Description	Symbol	BCY10	BZY10	Ref.
Doping level	x	0.1	0.1	
A/B ratio	z	1	1	
Eq. constant for vacancy generation	K_s	10^{-20}	10^{-20}	159
Eq. constant for electronic equilibrium	K_i	10^{-11}	10^{-11}	159,163
Eq. constant for hole formation ($atm^{-1/2}$)	K_{ox}	$1.5{\cdot}10^{-5}$	$1.5{\cdot}10^{-5}$	159
Eq. constant for proton formation (atm^{-1})	K_w	10	1	147
Mobility of protons ($cm^2{\cdot}s^{-1}{\cdot}V^{-1}$)	m_{OH}	$3.4{\cdot}10^{-4}$	$2.23{\cdot}10^{-4}$	147
Mobility of vacancies ($cm^2{\cdot}s^{-1}{\cdot}V^{-1}$)	m_V	$7.2{\cdot}10^{-5}$	$1.1{\cdot}10^{-7}$	147
Mobility of electrons ($cm^2{\cdot}s^{-1}{\cdot}V^{-1}$)	m_n	$1.78{\cdot}10^{-3}$	$2.23{\cdot}10^{-4}$	
Mobility of holes ($cm^2{\cdot}s^{-1}{\cdot}V^{-1}$)	m_p	$1.78{\cdot}10^{-3}$	$2.23{\cdot}10^{-4}$	164

BCY10 has a higher $[OH_O^{\bullet}]/[V_O^{\bullet\bullet}]$ ratio than BZY10, which is due to the higher enthalpy of hydration (reflected in the higher value of K_w), that helps to stabilize the protonic defects. Despite this, BCY10 has a higher oxide-ion conductivity than BZY10. In fact, while mobility of protons is of the same order of magnitude for BCY10 and BZY10 the mobility of vacancies is two orders of magnitude lower in BZY10 than in BCY10, therefore the oxide-ion contribution to the total conductivity decreases dramatically. Since the

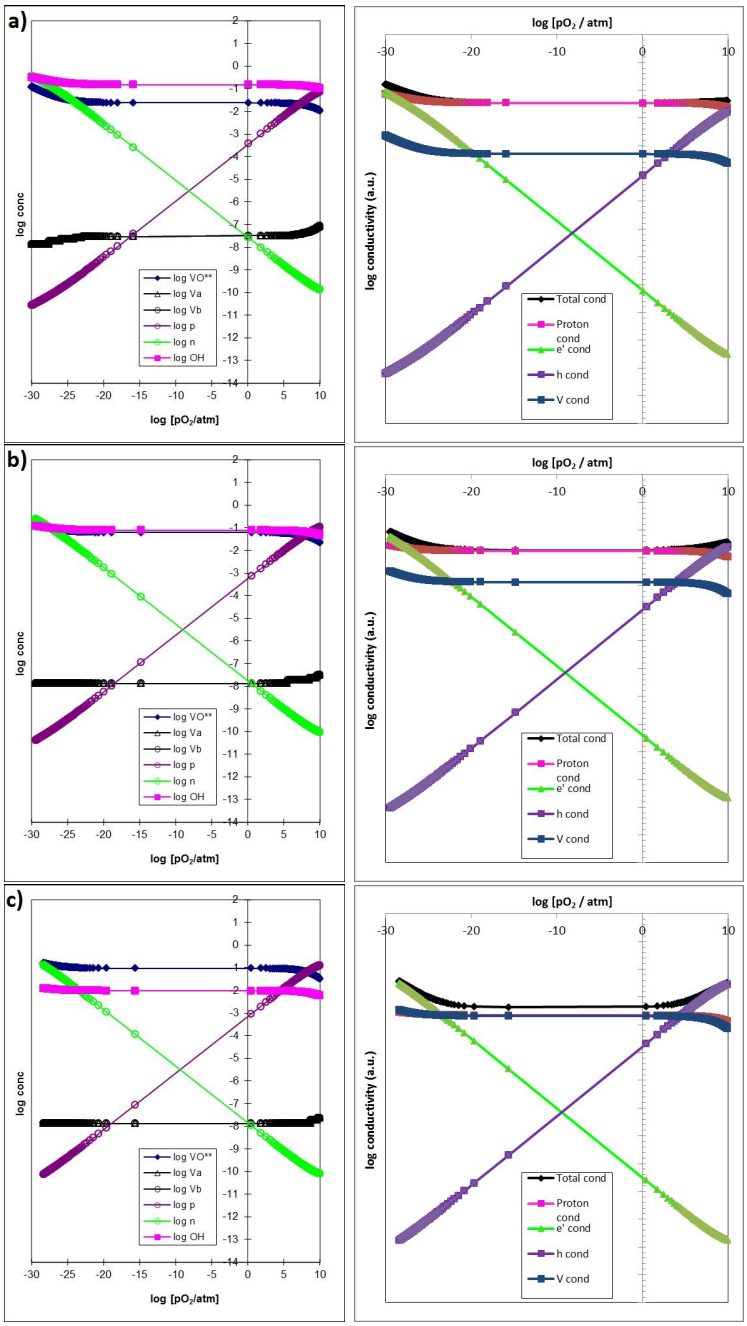

Figure 6.3: Concentration of defects and partial conductivities for BCZY26 at 600 °C at a) p_{H_2O} = 0.1 atm, b) p_{H_2O} = 0.01 atm, c) p_{H_2O} = 0.0001 atm.

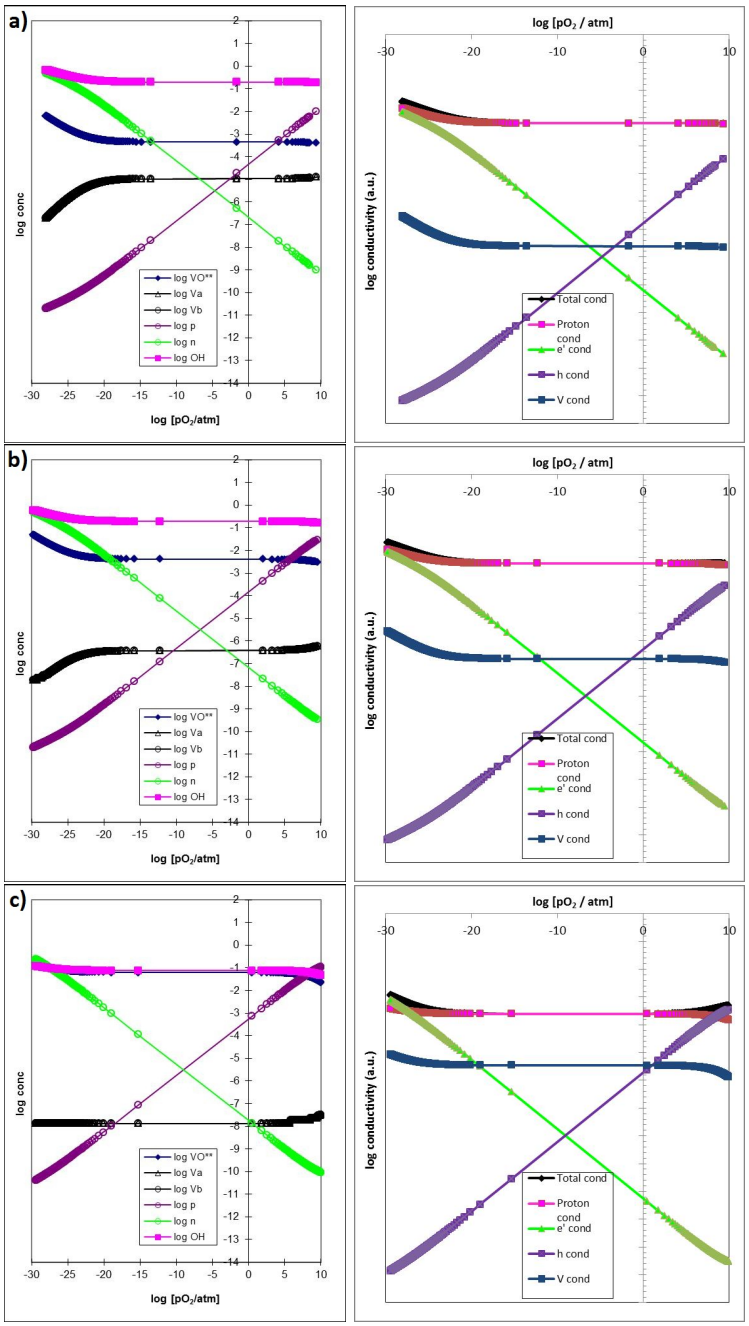

Figure 6.4: Concentration of defects and partial conductivities for BCZY26 at 400 °C at a) p_{H_2O} = 0.1 atm, b) p_{H_2O} = 0.01 atm, c) p_{H_2O} = 0.0001 atm.

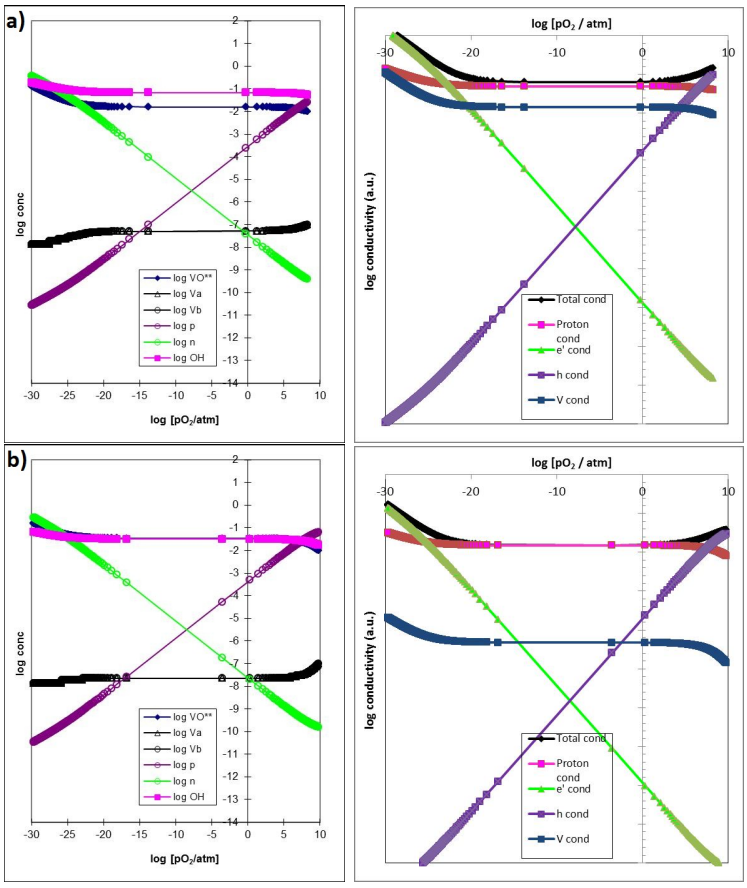

Figure 6.5: Concentration of defects and partial conductivities at 600 °C and p_{H_2O} = 0.01 atm for: a) BCY10, b) BZY10.

hole mobility of BCY10 is available from literature data[164] it is here used for calculations on BCY10 (both for holes and electrons), while the mobilities of electrons and holes are put equal to the mobility of protons for BZY10.

6.3 Conclusions

The calculations reported in this chapter show that Y-doped $BaCeO_3$-$BaZrO_3$ solid solutions exhibit dominant proton conductivity in a wide range of water and oxygen partial pressures. Proton conductivity increases with an increase in water partial pressure, while oxide-ion conductivity decreases. Lowering the temperature increases the concentration of protons and decreases the concentration of oxygen vacancies, increasing the fraction of protonic conductivity. BZY has a higher fraction of protonic conductivity compared to BCY because of the lower mobility of oxygen vacancies.

In conclusion, BCZY is an interesting candidate for electrochemical synthesis of ammonia, since proton conductivity dominates over oxide-ion conductivity, even at very low water partial pressures, below 600 °C. However electronic conductivity might pose a problem in extremely reducing conditions such as dry H_2 or under high polarization. In these calculations the contribution of n and p conductivity could be evaluated only semiquantitatevely for lack of accurate reference data.

Chapter 7

Choice of electrolyte

The electrolyte for a cell for electrochemical synthesis of ammonia needs to have an acceptable proton conductivity (i.e. $\sigma > 10^{-4}$ S/cm) below 500 °C in dry conditions (i.e. $p_{H_2O} < 0.001$ atm): as stated in Chapter 1, very low water partial pressures are necessary to avoid poisoning of the cathode electrocatalysts.[16] A proton conductivity of 10^{-4} S/cm is too low for technical applications, but would be acceptable for the present study since it would allow the testing of electrocatalysts in an electrochemical cell.

The conductivities in "dry" atmosphere ($p_{H_2O} < 0.001$ atm) measured in the present study are presented in Figure 7.1 together with literature data for BCZY26.

Ferroxane-derived materials have conductivities below 10^{-6} S/cm at 25-40 °C. The findings in this thesis suggest that the proton conduction takes place in a layer of adsorbed water on the surface of the grains. The conductivity is thus expected to decrease with increasing temperature because of thermally induced desorption. Therefore this class of materials is not a viable candidate for the present application.

Concerning pyrophosphates, SiY10, SnY10, ZrY10+P and all the titanium pyrophosphates (Ti370, T600, Ti650, Ti970) have conductivities lower than 10^{-4} S/cm, and thus are not suitable.

The only materials having conductivity higher than 10^{-4} S/cm below 500 °C in dry atmosphere are BCZY26, CeY10+P, CeGd10 and the composite CeY10+P/KH_2PO_4.

CeGd10, CeY10+P and CeY10+P/KH_2PO_4 have $\sigma > 10^{-4}$ S/cm below 200 °C, which is advantageous since the thermal stability of ammonia increases with decreasing temperature. However CeGd10 and CeY10+P degrade significantly in dry atmosphere upon hydration-dehydration cycling and long term testing (see Figure 5.11), with their conductivity going below 10^{-4} S/cm at 155 °C. The degradation behavior of CeY10+P/KH_2PO_4 has not been investigated in the present work, but considering the behavior of CeY10+P it is reasonable to expect a similar degradation behavior.

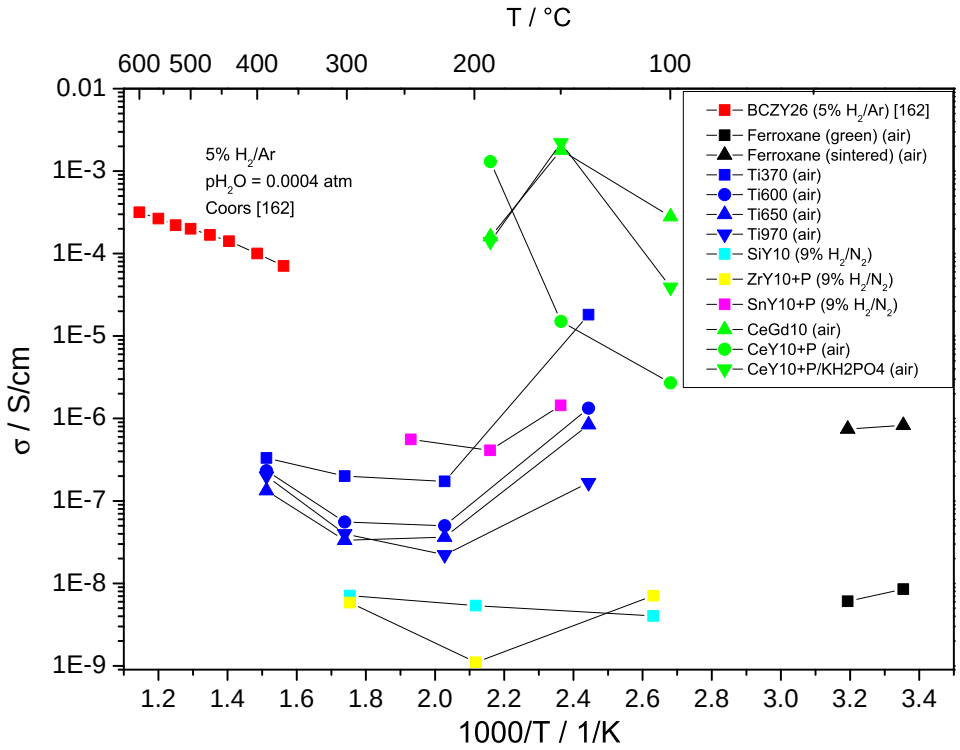

Figure 7.1: Conductivities in "dry" atmosphere ($p_{H_2O} < 0.001$ atm) for the classes of materials presented in Part I.

Moreover, the exact mechanism of proton conduction in these materials is not fully understood yet, thus this would add an additional factor of uncertainty to the studies carried out in the next part of the thesis.

On the contrary, Y-doped barium zirconates/cerates such as BCZY26 experience negligible degradation during testing and their defect chemistry is well understood (Chapter 6). The only drawback is that they have the desired conductivity in dry atmosphere ($p_{H_2O} < 0.001$ atm) only above 400 °C. A possible way to compensate for this would be using thinner electrolyte layers: however the fabrication of such thin layers would require a significant experimental effort. With respect to the aim of this thesis, BCZY is a reasonable compromise since electrode development must be addressed as well.

In conclusion, it is here chosen to use BCZY26 ($BaCe_{0.2}Zr_{0.6}Y_{0.2}O_{2.9}$) as electrolyte, and Part II of the thesis presents the development and testing of electrodes supported on BCZY26 electrolyte.

Part II

Electrodes

One of the main challenges for electrochemical synthesis of ammonia is to find electrocatalysts able to catalyse nitrogen reduction to ammonia ($N_2 + 6H^+ + 6e^- \rightarrow 2NH_3$) over hydrogen evolution ($2H^+ + 2e^- \rightarrow H_2$).

Nearly infinite combinations of elements can be used as catalysts. Indeed, when the Haber-Bosch process was developed at BASF, almost all the elements of the periodic table were tested in thousands of test in order to find the optimal catalyst.[166]

If the screening of a number of potential electrocatalysts has to be carried out, it is technically and economically convenient to have a flexible process for electrode fabrication, allowing to change the catalyst while keeping most of the process parameters unchanged.

In order to do this it is here suggested to use composite metal-BCZY electrodes fabricated with a two-step process. In the first step a porous backbone of a solid state proton conductor (BCZY26) is screen printed on BCZY26 electrolyte, producing an electrolyte-supported cell. In the second step the porous backbone is infiltrated with a solution containing metal ions. Different solutions can be used on identical porous backbones, making this fabrication process much simpler than for example the fabrication of metal/BCZY26 cermets.

In this thesis iron and molybdenum are investigated as possible electrocatalysts for electrochemical synthesis of ammonia: therefore Chapter 8 and Chapter 9 present a study of Fe-BCZY26 and Mo-BCZY26 electrodes.

Chapter 8

Composite Fe - BCZY26 electrodes

Fe is the standard Haber-Bosch catalyst, and therefore a reasonable first candidate for this electrocatalyst screening study. The Fe-BCZY electrode is here investigated by impedance spectroscopy and its potential is assessed.

Abstract

Symmetrical cells with composite Fe-$BaCe_{0.2}Zr_{0.6}Y_{0.2}O_{2.9}$ electrodes are produced by screen printing and infiltration on $BaCe_{0.2}Zr_{0.6}Y_{0.2}O_{2.9}$ electrolyte. The cells are studied by impedance spectroscopy at OCV in dry and wet H_2/N_2 and H_2/Ar mixtures at 250-500 °C to assess the electrochemical performance of the electrode and the possibility of using Fe as electrocatalyst for electrochemical synthesis of ammonia. The polarization resistance in 1 % wet H_2 is circa 1.6 Ω cm^2 at 500 °C and is estimated to be 0.45 Ω cm^2 at 600 °C in 1 % wet H_2. These low polarization resistances in wet H_2 suggest that this electrode could have potential as hydrogen electrode in proton conducting fuel cells. The composite electrode degrades over time, likely because of loss of electronic percolation due to coarsening of the iron nanoparticles. The comparison of the cell impedance measured at OCV in dry H_2/N_2 and H_2/Ar shows some differences in the low-frequency region, but because of uncertainties on the hydrogen content of the gases and cell degradation over time it cannot be assessed if Fe is active toward nitrogen reduction at OCV conditions.

8.1 Introduction

Fuel cells and electrolysers based on proton conducting elecrolytes are of great interest for their potential to operate at intermediate temperatures

(400-600 °C). Solid oxide fuel cells (SOFCs) require instead operating temperatures above 700 °C, which cause issues such as catalyst degradation by coarsening, interfacial reactions among components, interconnect oxidation and thermal expansion mismatches.[96,97] Reducing the operating temperature can limit these problems and lower costs.

Proton conductors are viable electrolytes at intermediate temperatures because protons migrate more easily than oxygen ions at 400-600 °C, thus conductivities are high enough for technical applications. Solid solutions of Y-doped $BaCeO_3$ and $BaZrO_3$, referred to as BCZY, are nowadays studied as electrolytes for proton conducting fuel cells (PCFCs) with encouraging results.[147,153]

Reducing the operating temperature below 600 °C reduces both electrolyte conductivity and electrode performance, leading to higher electrode overpotentials.[146] Therefore improvements of the electrodes are essential for the development of proton conducting electrochemical cells. The research on electrode materials specifically designed for proton conducting cells is still at an early stage, and simply using SOFC electrode materials is not a viable strategy since the reaction mechanisms differ.[132]

One interesting application for proton conducting electrochemical cells operating at intermediate temperatures is electrochemical synthesis of ammonia, i.e. producing NH_3 at the cathode of an electrochemical cell[20] according to Reaction 8.1:

$$N_2 + 6H^+ + 6e^- \rightarrow 2NH_3 \tag{8.1}$$

The research efforts in this area have been recently reviewed by Amar *et al.*[7] One of the main challenges in achieving electrochemical synthesis of ammonia is finding an electrocatalyst favoring the nitrogen reduction reaction over the competing hydrogen evolution reaction. So far mainly noble metals such as Pt, Pd and Ag have been used as electrocatalysts:[7,26,30,167] however these catalysts are expensive and according to density functional theory (DFT) calculations they are not the best candidates to catalyze ammonia synthesis.[13,51] All electrocatalysts need to operate in a water-free environment (at least on the cathode side of the cell), since oxygen atoms and OH groups would otherwise adsorb strongly poisoning all the sites available for N_2 dissociation.[16]

Iron is one of the best catalyst for ammonia production via the traditional Haber-Bosch process, developed at the beginning of the 20th centhury. Indeed, nowadays the production plants use multi-promoted iron catalysts which are still quite similar to the one originally developed by BASF a century ago.[166,168] Moreover, DFT calculations suggest that iron is a promising catalyst also for electrochemical synthesis of ammonia.[13]

This chapter thus studies the electrode performance of Fe - $BaCe_{0.2}Zr_{0.6}Y_{0.2}O_{2.9}$ composite electrodes, produced by screen printing and infiltration, sup-

ported on a $BaCe_{0.2}Zr_{0.6}Y_{0.2}O_{2.9}$ electrolyte. This fabrication strategy is believed to be effective in increasing the active thickness of the electrode, ensuring that the three-phase boundary extends into the bulk of the electrode.[154,169] The aim of the chapter is to evaluate the electrochemical performance of the electrode and to assess the potential of iron as electrocatalyst for electrochemical synthesis of ammonia. In order to do this, impedance spectroscopy at OCV is carried out on the cells at different temperatures and p_{H_2}.

8.2 Experimental

8.2.1 Cell Fabrication

The BCZY26 ($BaCe_{0.2}Zr_{0.6}Y_{0.2}O_{2.9}$) electrolyte substrates are prepared by solid state reactive sintering. As precursors, $BaCO_3$ (Alfa Aesar, 99.95 %), ZrO_2 (Tosoh), Y_2O_3 (Johnson Matthews, 99.9 %) and CeO_2 (Alfa Aesar, 99.9 %) are used. After drying the precursors, stoichiometric amounts of the compounds are weighted and 1 wt % of NiO (Alfa Aesar, 99 %), calculated with respect to the final target weight of the BCZY26 compound, is added as sintering aid.[153] The powders are ball milled in acetone for 24 hours with zirconia balls to homogenize the mixture. A small amount of binder, composed of PeOx (poly(2-ethyl-2-oxazoline)), Kellox dispersant (fish oil) and acetone, is then added and the mixture further ball milled for 1 hour. The powders are then dried at room temperature and sieved manually through a 106 µm sieve.

Cylindrical pellets (12 mm diameter) are produced by uniaxial pressing and sintered in air at 1500 °C for 8 hours according to this heating schedule: heating to 450 °C at 60 °C/h, heating to 1500 °C at 100 °C/h, holding at 1500 °C for 8 hours and cooling down at 100 °C/h. The pellets are cut to 500 µm thickness.

8.2.2 Screen printing of porous backbones and infiltration

The BCZY26 powders are prepared from the same precursors as described before. The precursors, without any sintering aid, are ball milled in acetone for 24 hours with zirconia balls to homogenize the mixture, calcined at 1400 °C for 30 hours and then ball milled in ethanol for 24 hours. The BCZY26 powders are mixed with Solsperse 20 wt % in Terpineol, dibutyl phthalate as plasticizer and 5 wt % ethylcellulose in Terpineol as binder. The ink is shaken for 48 hours with zirconia balls.

A layer is screen printed on both sides of the dense substrates using a stainless steel mesh (325 µm mesh) with a speed of the blade of 60 mm/s. The samples are dried for 10 minutes at 90 °C and subsequently heat treated

at 1300 °C for 2 hours in air (heating schedule: 60 °C/h to 450 °C, 100 °C/h to 1300 °C).

The iron nitrate solution (1 M concentration) is prepared by dissolving an appropriate amount of $Fe(NO_3)_3 \cdot 9H_2O$ (99.99 %, Sigma Aldrich) in distilled water. Triton X-100 is added as surfactant.

One drop of solution is placed on the porous backbone using a syringe, the excess liquid is removed and the cell put in a vacuum oven for 2 minutes. The same procedure is repeated for both the sides of the cell, which then is heat treated at 350 °C for 0.5 hours. This procedure is repeated for each infiltration step. Cells are infiltrated 3, 6, 9, 12 times: they are referred respectively as Fe3, Fe6, Fe9 and Fe12. The mass gain is measured after each infiltration by weighing the cells with a precision balance (XS205, Mettler Toledo).

8.2.3 XRD/SEM

X-Ray diffraction studies are performed on the cells to verify which phases are present in the material after the fabrication and after electrochemical testing. A Bruker D8 Discover X-Ray diffractometer is used (Cu K-α radiation, acceleration voltage 40kV, filament current 40 mA). SEM imaging is carried out on fractured cross sections of tested and untested cells using a Zeiss SUPRA SEM. The samples are attached to a metal sample holder using carbon tape and coated with a thin layer of carbon using a sputter coater.

8.2.4 Electrochemical characterization

Symmetrical cells are tested at 250 °C - 500 °C in 5-100 % H_2/N_2 mixtures and in 9 % H_2/Ar (uncertainty on H_2 content: ± 1 % H_2). A Pt net pressed against the electrode is used as a current collector. The p_{O_2} is monitored using a zirconia oxygen sensor at 1000 °C measuring the exhaust gases exiting the experimental setup; p_{H_2O} in dry gas is estimated from the H_2-O_2-H_2O equilibrium[170] to be $\approx 2 \cdot 10^{-4}$ atm.

Two-point impedance spectroscopy is performed at OCV using a Solartron 1260 Frequency Response Analyzer (Solartron Analytical, UK). Impedance spectra are recorded at OCV in the frequency range 980 kHz-0.05 Hz applying a sinusoidal signal with an amplitude of 0.05 V. The polarization resistance R_p and electrolyte resistance R_s are evaluated graphically.

The electrochemical test consists of three thermal cycles between 250 °C and 500 °C, carried out in the following order: in dry gas mixtures ($p_{H_2O} \approx 2 \cdot 10^{-4}$ atm), in 1 % wet gas mixtures ($p_{H_2O} = 0.01$ atm) and then again in dry gas mixtures. In each of the cycles the impedance spectroscopy at OCV is carried out upon cooling with 50 °C steps: for each step the temperature is kept constant and the composition of the gas mixture is changed.

The cell impedance is normalized by the surface area (0.66 cm^2) and divided by 2 to account for the two identical electrodes in series in the symmetrical cell. All electrode resistance values are therefore expressed in Ω cm^2. The capacitance values have been corrected as well to account for the two electrodes in series (i.e. the experimental value is divided by the area and multiplied by two): thus all capacitance values are expressed in F cm^{-2}.

8.3 Results

8.3.1 Phase identification and SEM imaging

During the heat treatment following the infiltration the iron in the iron nitrate solution reacts with BCZY26 to form $BaFeO_3$ (PDF 14-0180), and also other phases (that can not be indexed) are formed, as shown in Figure 8.1. After electrochemical testing (i.e. after exposure to wet and dry 5-100 % H_2 at 25-500 °C) only BCZY26 and Fe (PDF 06-0696) are visible in the XRD pattern (Figure 8.1c).

The porous backbone is approximately 10-15 µm thick and its morphology before and after infiltration is shown in Figure 8.2. The infiltrated particles are clearly visible after testing in the high magnification micrograph in Figure 8.3: their size is circa 70-100 nm.

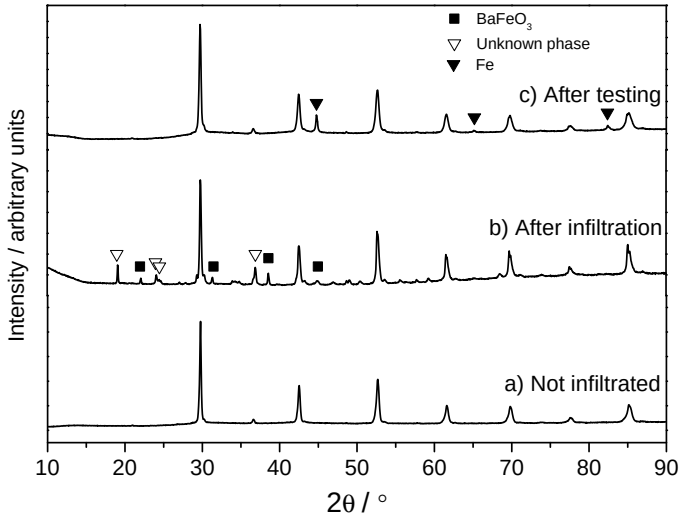

Figure 8.1: XRD patterns of cell a) not infiltrated, b) after infiltration, c) after electrochemical testing.

The average volume fraction of Fe relative to the total volume of the porous electrode is estimated from the increase in the mass of the cells after each infiltration step and is plotted in Figure 8.4 as a function of

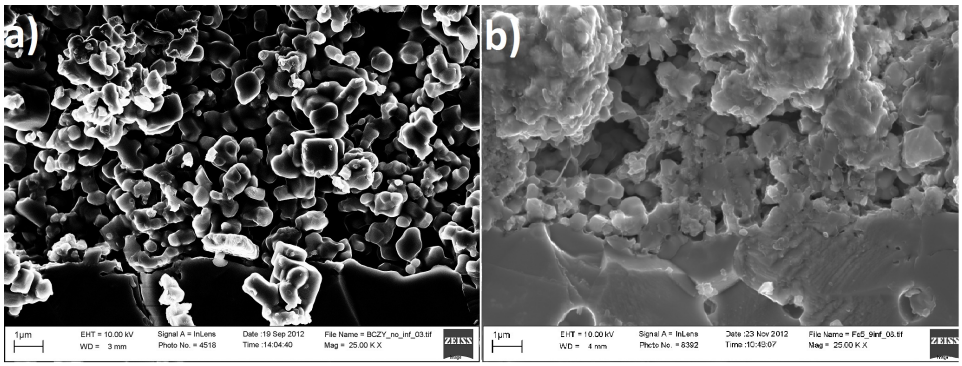

Figure 8.2: SEM micrographs of the fractured cross section of the porous backbone: a) before infiltration, b) after infiltration. The electrolyte is visible at the bottom of the micrographs.

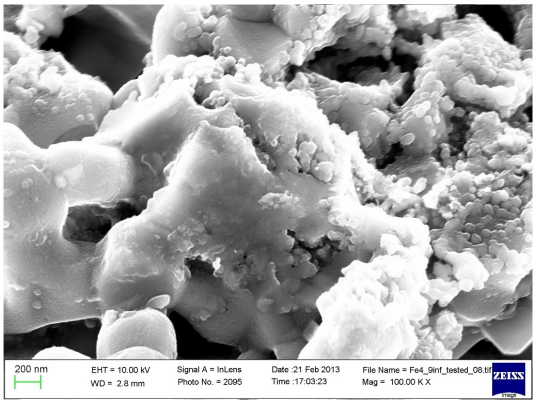

Figure 8.3: SEM micrograph of the fractured cross section of the infiltrated porous backbone after testing.

the number of infiltrations. The Fe loading increases monotonically with increasing number of infiltrations.

8.3.2 Cell impedance

Both polarization resistance R_p and electrolyte resistance R_s are strongly affected by the electrocatalyst loading, as can be seen comparing impedance spectra of different cells measured upon heating during the first thermal cycle of the test (Figure 8.5).

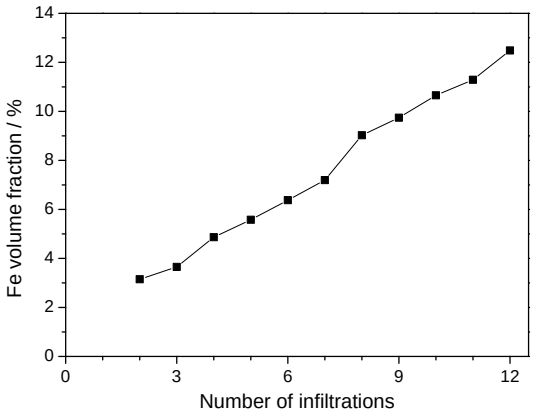

Figure 8.4: Estimated volume fraction of Fe as a function of the number of infiltration steps.

For Fe3 the Fe loading is too low for the porous layer to act as an electrode, thus the impedance is extremely high. For Fe6 the resistance values decrease significantly, reaching approximately a constant value after 9 infiltrations (cells Fe9 and Fe12). Only a Pt net is used as current collector, thus in practice only the infiltrated iron provides in-plane conductivity at the electrode surface.

R_s and R_p increase significantly over time upon thermal cycling. Figure 8.6 shows impedance spectra measured in the same conditions (400 °C, dry 9 % H_2/Ar) at different stages of the test. Spectrum *a* is measured upon heating during the first thermal cycle, while the spectrum *b* is measured upon cooling, i.e. the cell has further been 6 hours at 450 °C and 3 hours at 500 °C. Less than 10 hours of exposure at 450-500 °C are enough to cause a significant increase in R_s and R_p. These resistances increase even more (spectrum *c*) after a long term thermal cycle (circa 100 hours at 100-500 °C) in 1 % wet reducing gas mixtures (p_{H_2O} = 0.01 atm).

Figures 8.7, 8.8 and 8.9 provide an overview of the cell impedance of Fe12 measured at 450 °C in the first, second and third thermal cycle respectively. In all the spectra the electrode impedance includes at least two processes, with the one at lower frequency having a strong dependence on p_{H_2}.

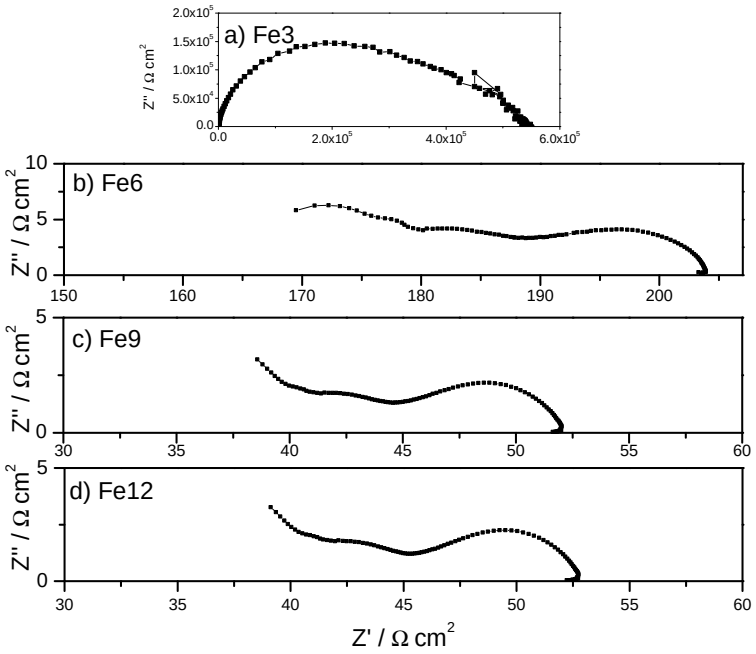

Figure 8.5: Nyquist impedance plots, measured at 450 °C in dry H_2 / Ar, of cells infiltrated: a) 3 times, b) 6 times, c) 9 times, d) 12 times. Notice the change in axis scale.

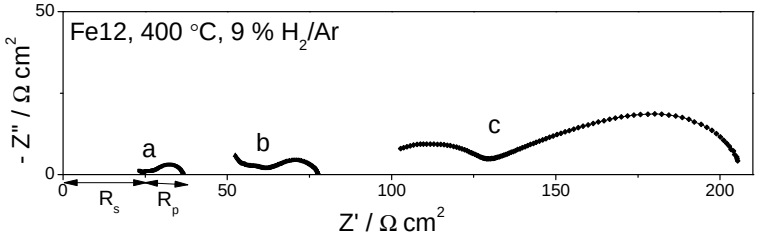

Figure 8.6: Nyquist plot for Fe12, measured at 400 °C in dry H_2: a) first measurement (upon heating), b) measured after spectrum *a* (after 6 hours at 450 °C and 4 hours at 500 °C), c) measured after a long-term thermal cycle in 1 % wet gas mixtures (circa 100 hours).

After switching to 1 % wet atmosphere (Figure 8.8) the electrolyte resistance R_s decreases significantly because of the increase in proton conductivity going from dry to wet atmosphere, while R_p decreases only slightly despite a change in shape of the spectra.

The impedance spectra measured in the third cycle (i.e. in dry gas after exposure to 1 % wet reducing atmosphere) exhibit much higher R_s and R_p values compared with the measurements in the first cycle.

R_p values (estimated graphically as in Figure 8.6) for 100 % H_2 in each of the thermal cycles are presented in Figure 8.10. The activation energies in the three cycles are respectively 0.63 eV, 0.7 eV and 0.63 eV.

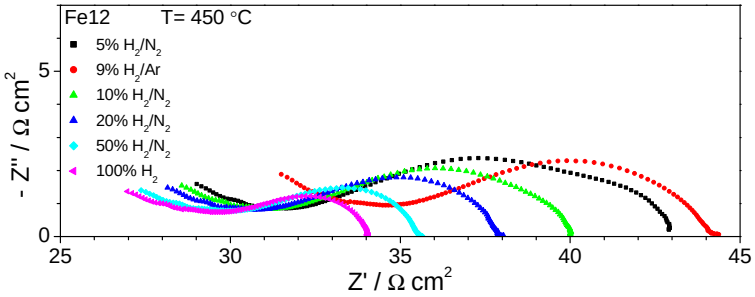

Figure 8.7: Nyquist plot of the impedance of Fe12 at 450 °C in dry H_2/N_2, H_2/Ar mixtures during the first thermal cycle (i.e. before exposure to 1 % wet reducing atmosphere).

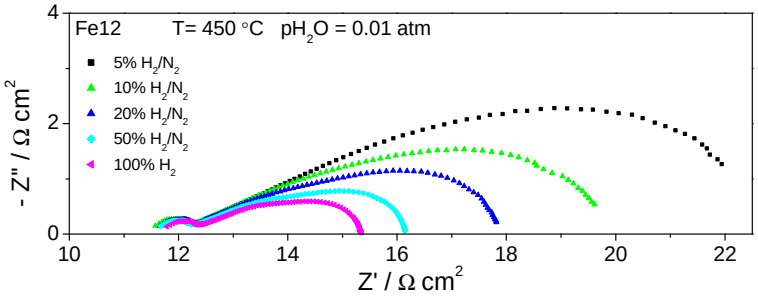

Figure 8.8: Nyquist plot of the impedance of Fe12 at 450 °C in 1 % wet (p_{H_2O} = 0.01 atm) H_2/N_2 mixtures.

8.3.3 Cell impedance in H_2/N_2 and H_2/Ar: a comparison

In order to assess whether the Fe-BCZY composite electrode can be a viable cathode for electrochemical synthesis of ammonia, Bode plots of impedance spectra measured at OCV in dry H_2/N_2 and H_2/Ar gas mixtures with approximately the same hydrogen concentration (9-10 %) are shown in Figures 8.11 and 8.12. The figures present impedances measured during the first and third cycle respectively.

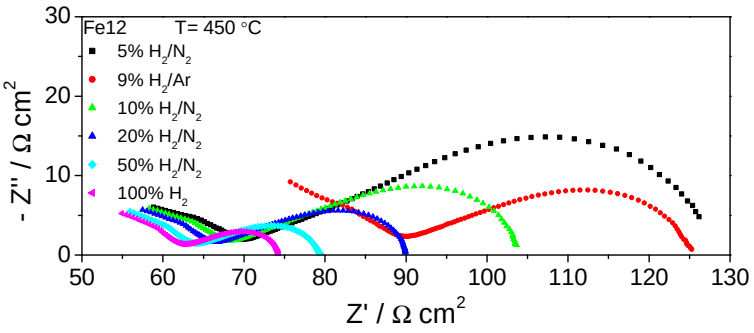

Figure 8.9: Nyquist plot of the impedance of Fe12 at 450 °C in dry H_2/N_2, H_2/Ar mixtures during the third thermal cycle (i.e. after exposure to 1 % wet reducing atmosphere).

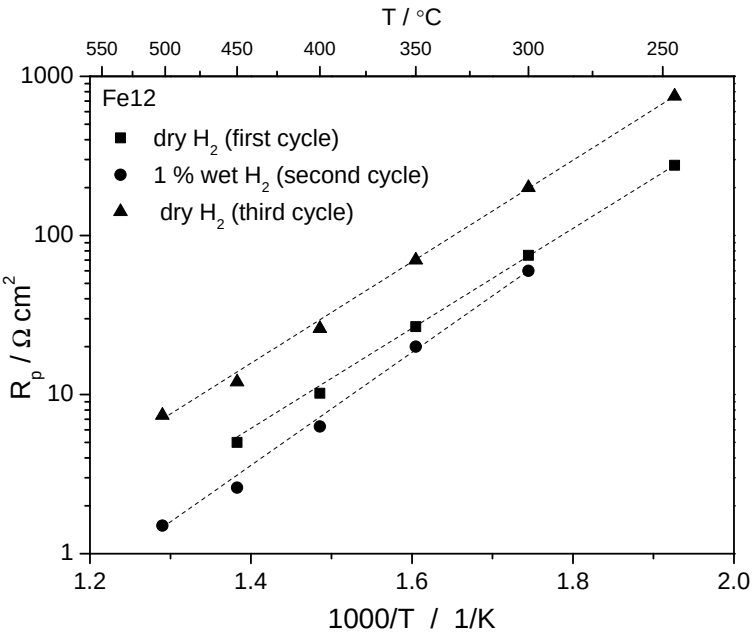

Figure 8.10: Arrhenius plot of polarization resistance R_p (evaluated graphically) in pure H_2 in each of the three thermal cycles.

Above 400 °C the real Bode plots measured in H_2/N_2 and H_2/Ar show differences almost independent of frequency (i.e. the curves have the same shape but with a constant offset between them).

The imaginary Bode plots show instead some minor differences in the low-frequency region (both in Figure 8.11 and 8.12): however they might be due to uncertainties in the hydrogen content of the gases and the degradation effects on the cell impedance.

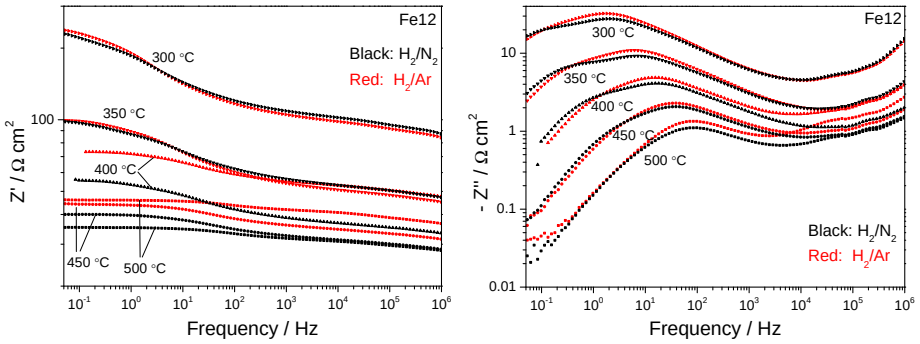

Figure 8.11: Bode impedance plot of Fe12, measured in dry H_2/N_2 and H_2/Ar gas mixtures (9-10 % H_2) at 300-500 °C during the first thermal cycle.

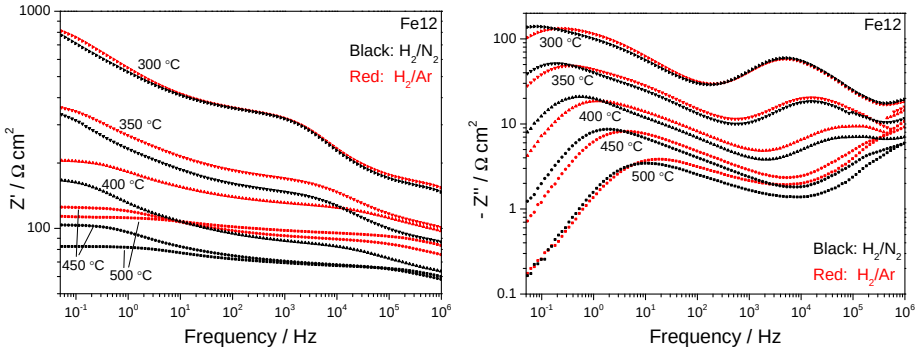

Figure 8.12: Bode impedance plot of Fe12, measured in dry H_2/N_2 and H_2/Ar gas mixtures (9-10 % H_2) at 300-500 °C during the third thermal cycle.

8.4 Discussion

The decrease in R_s with increasing iron loading suggests that the active area of the electrode is limited by the extent of the electronic percolation in the electrode structure. Electronic percolation in ceramic/metal composite electrodes is dependent on the volume fraction of metal: for Ni/YSZ anodes, circa 30 % Ni in volume is necessary to have electronic percolation.[171] In the present case of an infiltrated porous structure, the necessary metal volume

fraction is expected to be lower since the metal is not randomly distributed in a two-phase system but should instead form a layer of nanoparticles on BCZY in the pores. The fact that R_s does not decrease increasing the number of infiltrations above 9 (compare Fe9 and Fe12 in Figure 8.5) suggests that after 9 infiltrations all the geometrical area of the electrode is active.

The degradation of the electrode upon exposure to high temperatures during thermal cycling (Figure 8.6) might be attributed to microstructural changes of the infiltrated material, such as coarsening of the Fe nanoparticles. The coarsening processes are expected to take place also at 500 °C or below because of the submicrometric size of the Fe particles. Such processes would lead to a decrease in electronic percolation in the electrode structure and lead to an increase in both R_s and R_p. Considering that degradation would likely affect different electrode processes in different ways, this can explain the change in the shape of the impedance spectra between the first and third thermal cycle (Figures 8.7 and 8.9).

Fe has been studied as electrode on solid state proton conductors only by Hibino *et al.*[172] The authors use a FeO-containing slurry to fabricate a Fe electrode on Y-doped $BaCeO_3$, and test it under polarization at 600 °C in humidified H_2: from the slope of the polarization curves reported it is possible to estimate a R_p of circa 0.6 Ω cm^2, which decreases to 0.1 Ω cm^2 if the FeO powders in the slurry are impregnated with Pd particles.

In the study presented in this chapter the lowest R_p value measured is 1.6 Ω cm^2 at 500 °C in 1 % wet H_2 (Figure 8.10). The extrapolation up to 600 °C gives a value of 0.45 Ω cm^2, which is in agreement with the results of Hibino *et al.*[172]

The fact that this promising values are obtained despite the significant degradation of the cell and the use of only a Pt net as current collector makes Fe a promising candidate anode material for proton conducting fuel cells (PCFCs), in alternative to Ni. Improving the electronic percolation and reducing degradation, for example by increasing the catalyst loading and introducing sintering inhibitors to reduce coarsening,[173] could reduce R_p significantly.

By comparing the impedance spectra measured in H_2/N_2 and H_2/Ar (Figures 8.11 and 8.12) it is not possible to draw a conclusion on whether or not Fe is active toward reduction of nitrogen to ammonia, since the small differences between the spectra are likely due to degradation and small variations in the p_{H_2} of the gases. The differences in the real Bode plots between H_2/N_2 and H_2/Ar above 400 °C are equivalent to resistances, independent of frequency. This correlates well to the differences in R_s in the Nyquist plots, which are visible for example in Figure 8.7 and 8.9. This is due to the fact that in "dry" gas the conductivity of BCZY is much sensitive to changes in p_{O_2} and small changes in p_{H_2O} and temperature that inevitably occur when the atmosphere composition is changed. In order to evaluate the potential of Fe for electrochemical synthesis of ammonia it will be nec-

essary to minimize degradation of the cells and control more carefully the atmosphere: this would in fact reduce the causes of uncertainty.

8.5 Conclusions

Symmetrical cells with composite Fe-BCZY electrodes are produced by screen printing and infiltration and studied by impedance spectroscopy at OCV in dry and wet H_2/N_2 and H_2/Ar mixtures.

The cells degrade significantly upon exposure to temperatures up to 500 °C: it is suggested that the degradation is due to loss of electronic percolation caused by coarsening of the iron nanoparticles.

Despite the degradation, the polarization resistance in 1 % wet H_2 is circa 1.6 Ω cm^2 at 500 °C and is estimated by extrapolation to be 0.45 Ω cm^2 at 600 °C in 1 % wet H_2, in agreement with values reported in the literature by Hibino *et al.*[172] Iron may therefore be a promising anode material for PCFCs, once electronic percolation in the electrode is improved and degradation minimized.

The comparison of the cell impedance measured at OCV in dry H_2/N_2 and H_2/Ar shows some differences in the low-frequency region, but because of uncertainties in the hydrogen content of the gases and cell degradation over time it is not possible to assess if Fe is active toward nitrogen reduction at OCV conditions. Further measurements, also under polarization, will be required.

Chapter 9

Composite Mo - BCZY26 electrodes

Molybdenum is, according to DFT calculations, the best possible candidate for electrochemical synthesis of ammonia, thus Mo is an alternative candidate to Fe. Mo is integrated into the the BCZY porous backbone in a similar way as Fe and the performance of Mo-BCZY electrodes is investigated.

Abstract

Symmetrical cells with composite Mo-$BaCe_{0.2}Zr_{0.6}Y_{0.2}O_{2.9}$ electrodes are produced by screen printing and infiltration on $BaCe_{0.2}Zr_{0.6}Y_{0.2}O_{2.9}$ electrolyte. The cells are studied systematically by impedance spectroscopy at OCV in dry H_2/N_2 and H_2/Ar mixtures to assess the possibility of using Mo as electrocatalyst for electrochemical synthesis of ammonia and study the reaction kinetics at the electrode. The absence of significant differences in the impedance spectra measured at OCV in H_2/N_2 and H_2/Ar suggests that Mo is not an active electrocatalyst for nitrogen reduction to ammonia (at OCV). Three electrode processes are identified in the impedance spectra. The high-frequency process is assigned to proton transfer through the $BaCe_{0.2}Zr_{0.6}Y_{0.2}O_{2.9}$/Mo interface or inside the $BaCe_{0.2}Zr_{0.6}Y_{0.2}O_{2.9}$ porous electrode structure. The medium-frequency process is attributed to surface diffusion of hydrogen followed by a charge transfer. The third, low-frequency process is suggested to be related to adsorption of hydrogen on $Mo/BaMoO_4$.

9.1 Introduction

The cell concept used in Chapter 8, based on infiltration of a porous BCZY26 backbone to fabricate composite metal/BCZY26 electrodes, allows the infiltration of a number of different catalysts. DFT calculations by Howalt *et*

al.[13,52] suggest that molybdenum is one of the best electrocatalysts for the nitrogen reduction reaction:

$$N_2 + 6H^+ + 6e^- \rightarrow 2NH_3 \tag{9.1}$$

It must be pointed out that the electrocatalyst needs to operate in a water-free environment (at least on the cathode side of the cell), since oxygen atoms and OH groups would otherwise adsorb strongly on the electrocatalyst poisoning all the sites available for N_2 dissociation.[16]

This chapter investigates the electrode performance of composite Mo - $BaCe_{0.2}Zr_{0.6}Y_{0.2}O_{2.9}$ electrodes, produced by screen printing and infiltration, supported on a $BaCe_{0.2}Zr_{0.6}Y_{0.2}O_{2.9}$ electrolyte. This fabrication strategy is believed to be effective in increasing the active thickness of the electrode, ensuring that the three-phase boundary extends into the bulk of the electrode.[154,169] The aim of the work is to assess the potential of molybdenum as electrocatalyst for electrochemical synthesis of ammonia and to study the kinetics of the reaction taking place at the electrode. In order to do this, impedance spectroscopy at OCV is carried out on the cells at different temperatures and p_{H_2}.

9.2 Experimental

9.2.1 Cell Fabrication

The BCZY26 ($BaCe_{0.2}Zr_{0.6}Y_{0.2}O_{2.9}$) electrolyte substrates are prepared by solid state reactive sintering. As precursors, $BaCO_3$ (Alfa Aesar, 99.95 %), ZrO_2 (Tosoh), Y_2O_3 (Johnson Matthey, 99.9 %) and CeO_2 (Alfa Aesar, 99.9 %) are used. After drying the precursors, stoichiometric amounts of the compounds are weighted and 1 wt % of NiO (Alfa Aesar, 99 %), calculated with respect to the final target weight of the BCZY26 compound, is added as sintering aid.[153] The powders are ball milled in acetone for 24 hours with zirconia balls to homogenize the mixture. A small amount of binder, composed of PeOx (poly(2-ethyl-2-oxazoline)), Kellox dispersant (fish oil) and acetone, is then added and the mixture further ball milled for 1 hour. The powders are then dried at room temperature and sieved manually through a 106 µm sieve.

Cylindrical pellets (12 mm diameter) are produced by uniaxial pressing and sintered in air at 1500 °C for 8 hours according to this heating schedule: heating to 450 °C at 60 °C/h, heating to 1500 °C at 100 °C/h, holding at 1500 °C for 8 hours and cooling down at 100 °C/h. The pellets are cut to 500 µm thickness.

9.2.2 Screen printing of porous backbones and infiltration

The BCZY26 powders are prepared from the same precursors as described before. The precursors, without any sintering aid, are ball milled in acetone for 24 hours with zirconia balls to homogenize the mixture, calcined at 1400 °C for 30 hours and then ball milled in ethanol for 24 hours. The BCZY26 powders are mixed with Solsperse 20 wt % in Terpineol, dibutyl phthalate as plasticizer and 5 wt % ethylcellulose in Terpineol as binder. The ink is shaken for 48 hours with zirconia balls.

A layer is screen printed on both sides of the dense substrates using a stainless steel mesh (325 µm mesh) with a speed of the blade of 60 mm/s. The samples are dried for 10 minutes at 90 °C and subsequently heat treated at 1300 °C for 2 hours in air (heating schedule: 60 °C/h to 450 °C, 100 °C/h to 1300 °C).

The molybdenum solution (1 M concentration) is prepared dissolving an appropriate amount of MoO_3 in a 16:100 volume mixture of 28 wt % ammonia (Merck) and distilled water. Triton X-100 is added as surfactant.

One drop of solution is placed on the porous backbone using a syringe, the excess liquid is removed and the cell put in a vacuum oven for 2 minutes. The same procedure is repeated for both the sides of the cell, which then is heat treated at 500 °C for 0.5 hours. This procedure is repeated for each infiltration step. Cells are infiltrated 3, 6, 9 and 12 times. The mass gain is measured after each infiltration by weighing the cells with a precision balance (XS205, Mettler Toledo).

9.2.3 XRD/SEM

X-Ray diffraction studies are performed on the cells to verify which phases are present in the material after the fabrication and at different steps of the electrochemical testing. A Bruker D8 Discover X-Ray diffractometer is used (Cu K-α radiation, acceleration voltage 40kV, filament current 40 mA).

SEM imaging is carried out on fractured cross sections of tested and untested cells using a Zeiss SUPRA SEM. The samples are attached to a metal sample holder using carbon tape and coated with a thin layer of carbon using a sputter coater.

9.2.4 Electrochemical characterization

Gold paste (ESL Europe, UK) is painted on top of the porous backbones after infiltration to act as a current collector. The cells are reduced before testing, by heating at 900 °C in dry H_2 for 40 min. The symmetrical cells are tested at 440 °C - 650 °C in 5-100 % H_2/N_2 mixtures and in 9 % H_2/Ar (uncertainty on H_2 content: ±1 % H_2). Dry gas has $p_{H_2O} < 0.001$ atm and 1 % wet gas has $p_{H_2O} = 0.01$ atm. The p_{O_2} is monitored using a zirconia oxygen sensor.

Two-point impedance spectroscopy is performed using a 3522-50 LCR HiTester (Hioki, Japan). Impedance spectra are recorded at OCV in the frequency range 98 kHz-0.05 Hz applying a sinusoidal signal with an amplitude of 0.01 V and are analyzed with commercial softwares ZView (Scribner Associates, USA) and ZSimpWin (EChem Software, USA) and the in-house developed software Ravdav.[174] The data are corrected for inductance subtracting point-by-point the impedance of the short-circuited system from the impedance of the symmetrical cell.

The cell impedance is normalized by the surface area (0.66 cm^2) and divided by two to account for the two identical electrodes in series in the symmetrical cell. All electrode resistance values reported in this paper are therefore expressed in $\Omega\ cm^2$. The capacitance values have been corrected as well to account for the two electrodes in series (i.e. the experimental value is divided by the area and multiplied by two): thus all capacitance values are expressed in $F\ cm^{-2}$.

9.3 Results

9.3.1 Phase identification and SEM imaging

During the heat treatment following the infiltration the molybdenum in the infiltration solution reacts with the BCZY26 in the porous backbone to form $BaMoO_4$ (PDF 2-449), as confirmed by the XRD patterns in Figure 9.1. The subsequent reduction at 900 °C for 40 minutes in dry H_2 ($p_{O_2} \approx 10^{-23}$ atm) reduces $BaMoO_4$ to Mo (PDF 42-1120). The porous backbone is approximately 10-15 µm thick and its morphology before and after infiltration is shown in Figure 9.2: the infiltrated molybdenum particles seem to form a percolating structure across the porous backbone.

To carry out an exposure experiment a cell is heat treated for 96 hours at 550 °C in 9 % H_2/Ar (1 % wet), and subsequently for 48 hours in dry 9 % H_2/Ar. The XRD patterns in Figure 9.3 show that a small amount of $BaMoO_4$ is formed again upon exposure to wet reducing atmosphere, and that it does not get reduced to metallic molybdenum at 550 °C in dry 9 % H_2/Ar.

9.3.2 Fitting of impedance spectra

The four cells are infiltrated 3, 6, 9 and 12 times respectively. The number of infiltrations does not have a significant effect on the shape and dimension of the impedance spectra. The impedance spectra and the fitting calculations presented in this work belong to the cell infiltrated 9 times, which is representative of the behavior of all the cells. Within experimental error, the four cells exhibit the same trends versus temperature and p_{H_2}.

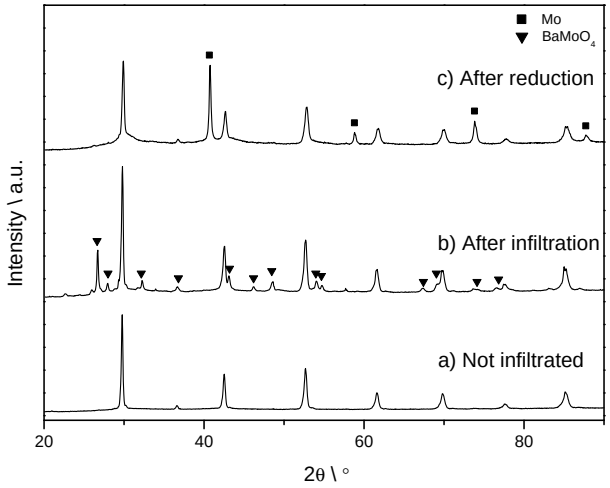

Figure 9.1: XRD patterns of cell a) not infiltrated, b) after infiltration, c) after reduction.

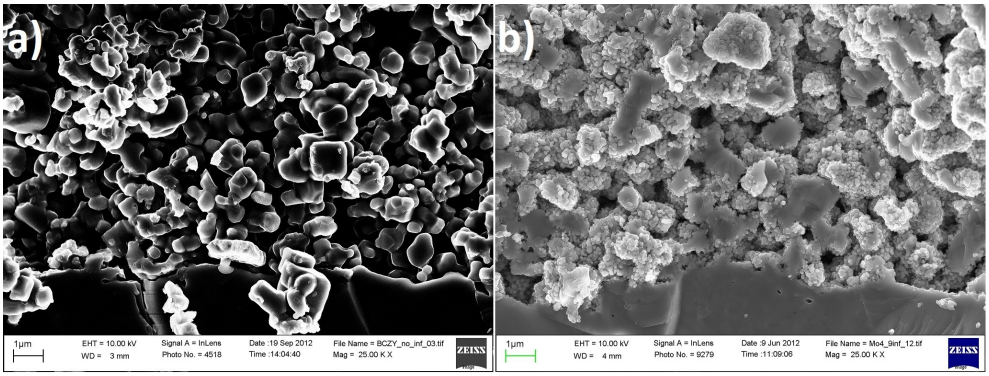

Figure 9.2: SEM micrographs of the fractured cross section of the porous backbone: a) not infiltrated, b) infiltrated 9 times and reduced (before testing). The electrolyte is visible at the bottom of the micrographs.

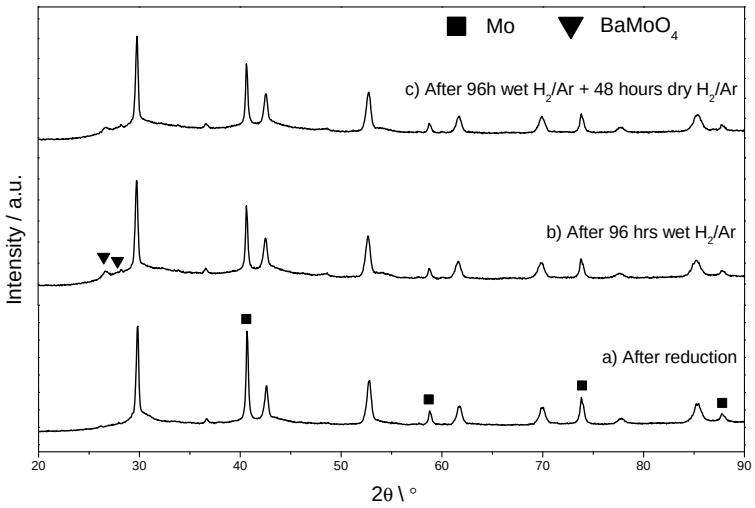

Figure 9.3: XRD patterns of cell a) after reduction, b) after 96 hours in 9 % H_2/Ar (1 % wet) at 550 °C, c) after 96 hours in 1 % wet and 48 hours in dry 9 % H_2/Ar at 550 °C.

Figure 9.4 and Figure 9.5 give an overview of how the impedance spectra change with changing temperature and p_{H_2} in dry gas mixtures.

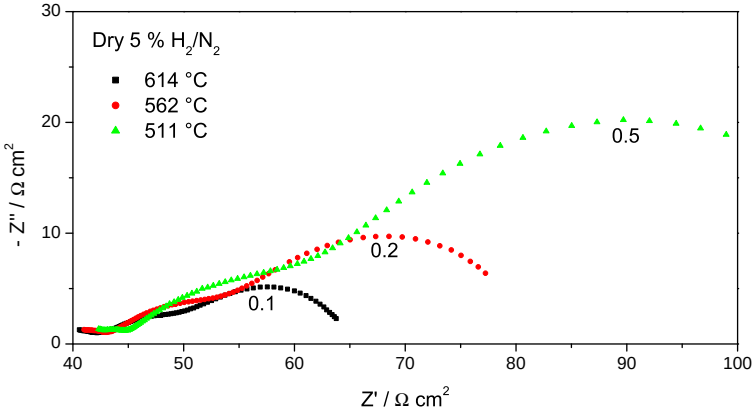

Figure 9.4: Nyquist plot for cell tested in dry 5 % H_2/N_2 at different temperatures. Numbers on plot indicate summit frequencies.

The impedance spectra are fitted using a $R_s(R_{gb}Q_{gb})(R_1Q_1)(R_2Q_2)(R_3Q_3)$ equivalent circuit, where R_s is the electrolyte bulk resistance, $(R_{gb}Q_{gb})$ fits the grain boundary impedance and the other three (RQ) elements fit the three processes that contribute to the electrode impedance (as shown in Figure 9.6). Each (RQ) element consists of a resistance R and a constant phase element Q connected in parallel.[63] The impedance of a constant phase element is given by Equation 9.2:

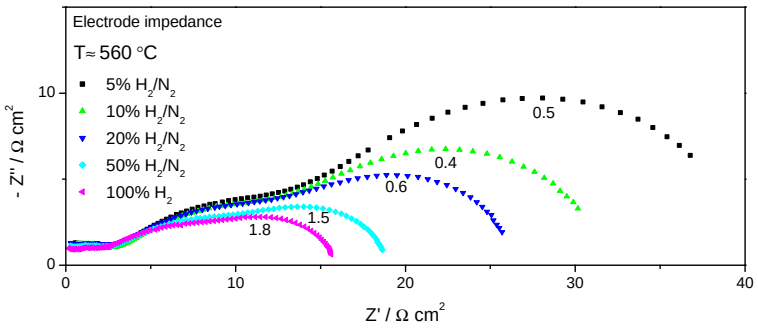

Figure 9.5: Nyquist plot for the electrode impedance of cell tested in 560 °C in dry H_2/N_2 mixtures. The total electrolyte resistance has been subtracted from the cell impedance. Numbers on plot indicate summit frequencies.

$$Z_Q = \frac{1}{Y_0(j\omega)^n} \tag{9.2}$$

Y_0 is a frequency-independent constant, $\omega = 2\pi f$, j is the square root of -1, and n is a constant whose value is between 0 and 1. If $n = 1$, Q is an ideal capacitance, while if $n = 0$, Q becomes an ideal resistor.

In order to calculate the equivalent capacitance for the process fitted by a RQ parallel, Equation 9.3 has been used:[175]

$$C = \frac{(RY_0)^{\frac{1}{n}}}{R} \tag{9.3}$$

Because of limitations in the frequency range investigated, only a small part of the impedance spectrum provides information about the grain boundary impedance. Therefore in the data fitting the grain boundaries have been fitted with a (RQ) where the values of the parameters of Q have been kept constant, with values compatible with those obtained from fitting of impedance spectra measured at lower temperatures, where the grain boundary arc is visible.

High-frequency artifacts and distortions are inevitably present at f > 20-50 kHz, and the impedance of the high-frequency electrode process is much smaller than the ones of neighboring arcs: this means that the exact temperature and p_{H_2} dependence can not be obtained for the high frequency electrode process. However, thanks to its small value compared to the other contributions to the electrode impedance, possible errors do not affect significantly the fitting of the other processes.

To ensure that the resistance and capacitance values obtained from the fitting can be significantly compared, the n values of the constant phase elements are kept constant when fitting spectra measured at different temperatures and in different dry gas mixtures. The n parameters are instead changed to fit the impedance spectra in wet atmosphere (see Section 9.3.8).

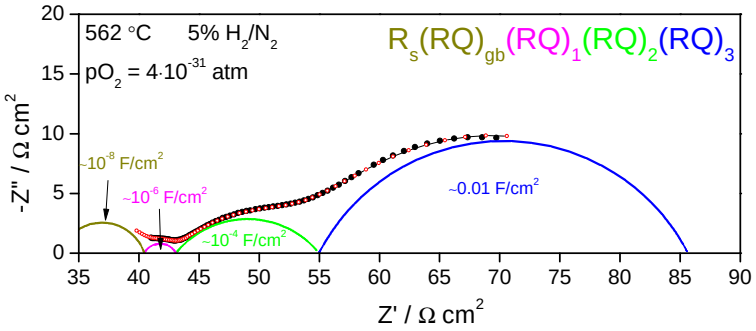

Figure 9.6: Nyquist plot measured at 562 °C in 5 % H_2/N_2. Each semicircle corresponds to each of the RQ parallels in the circuit used for the data fitting.

Table 9.1: Voltage readings of p_{O_2} sensor at 560 °C in dry gas mixtures and corresponding p_{O_2} values.

Gas mixture	Voltage / V	p_{O_2} / atm
5 % H_2/N_2	1.238	$4.96{\cdot}10^{-31}$
10 % H_2/N_2	1.264	$1.29{\cdot}10^{-31}$
20 % H_2/N_2	1.282	$4{\cdot}10^{-32}$
50 % H_2/N_2	1.315	$6.36{\cdot}10^{-33}$
100 % H_2	1.337	$3.14{\cdot}10^{-33}$

9.3.3 Electrode impedance in dry gas mixtures

An overview of the values obtained by fitting for the electrode processes of the spectra measured at 560 °C in different dry gas mixtures (Figure 9.5) is reported in Table 9.2. Table 9.1 reports the p_{O_2} values measured at that temperature with the *in-situ* zirconia oxygen sensor.

Figure 9.7 shows the total electrode resistance R_p (i.e. the sum of R_1, R_2 and R_3) and its dependence on temperature and p_{H_2}. The overall activation energy of R_p is 0.68-0.72 eV, and assuming a power-law dependence on the p_{H_2} according to the equation

$$R_p \propto p_{H_2}^{-m} \tag{9.4}$$

the m value is between 0.28 and 0.4 (Figure 9.7).

However, it is clear from the Nyquist plots in Figure 9.4 and 9.5 that each of the processes has a different temperature and p_{H_2} dependence, therefore they are considered separately in the following sections.

9.3.4 Electrode process 1 (high frequency)

The dependence of resistance of process 1 on temperature and p_{H_2} is shown in Figure 9.8. Because of the experimental limitations explained in Sec-

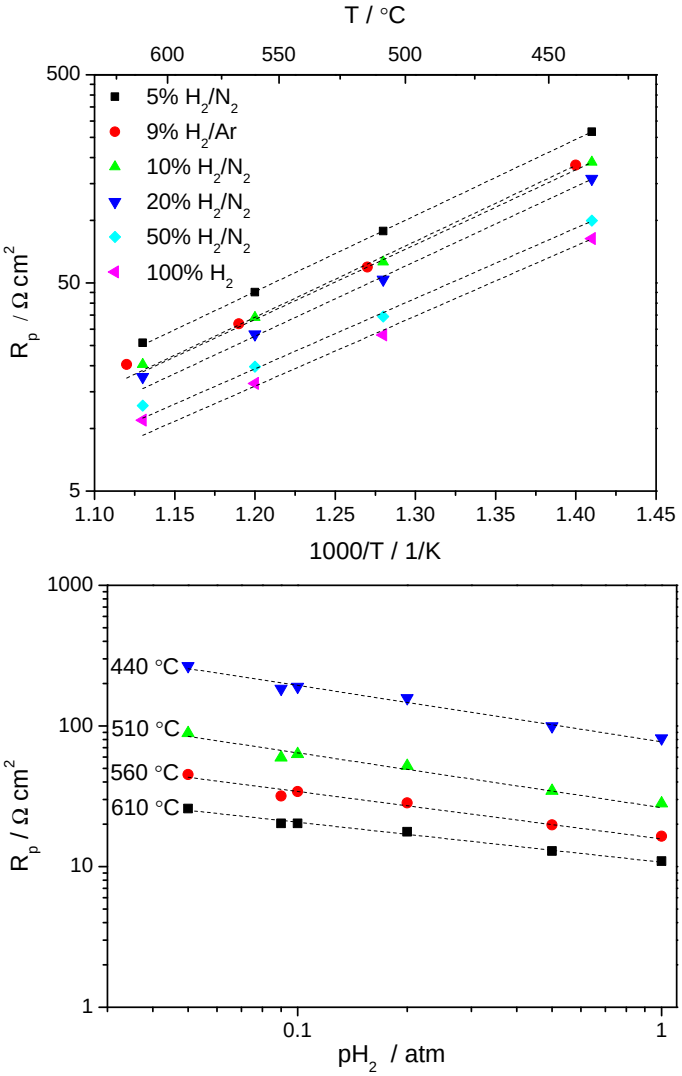

Figure 9.7: Arrhenius plot of the total electrode resistance R_p measured in dry gas mixtures.

Table 9.2: Fitting parameters for electrode processes in Figure 9.5.

	5 % H_2	**10 % H_2**	**20 % H_2**	**50 % H_2**	**100 % H_2**
R_1 ($\Omega\cdot$ cm^2)	2.63	2.83	2.68	2.51	2.11
Y_{0_1} ((F·s)$^{1-n}$/cm^2)	$9.45{\cdot}10^{-5}$	$8.94{\cdot}10^{-5}$	$1.38{\cdot}10^{-4}$	$1.52{\cdot}10^{-4}$	$2.1{\cdot}10^{-4}$
n_1	0.68	0.68	0.68	0.68	0.68
R_2 ($\Omega\cdot$ cm^2)	11.88	11.09	10.93	8.64	7.42
Y_{0_2} ((F·s)$^{1-n}$/cm^2)	$4.06{\cdot}10^{-3}$	$4.18{\cdot}10^{-3}$	$4.09{\cdot}10^{-3}$	$4.58{\cdot}10^{-3}$	$4.82{\cdot}10^{-3}$
n_2	0.57	0.57	0.57	0.57	0.57
R_3 ($\Omega\cdot$ cm^2)	30.67	20.20	14.70	8.67	6.92
Y_{0_3} ((F·s)$^{1-n}$/cm^2)	$3.06{\cdot}10^{-2}$	$3.12{\cdot}10^{-2}$	$3.06{\cdot}10^{-2}$	$3.30{\cdot}10^{-2}$	$3.30{\cdot}10^{-2}$
n_3	0.7	0.7	0.7	0.7	0.7

tion 9.3.2, these values are only indicative. The resistance is circa constant between 500-600 °C, with a small increase at 440 °C (Figure 9.8). The capacitance is in the range 2-20·10^{-6} F cm^{-2} (Figure 9.9). There is little or no dependence on the p_{H_2} for both resistance and equivalent capacitance.

9.3.5 Electrode process 2 (intermediate frequency)

R_2 decreases with increasing temperature (Figure 9.10) with an activation energy of 0.47-0.54 eV and weakly depends on p_{H_2} (m = 0.16-0.21). The equivalent capacitance is in the range 1-10·10^{-4} F cm^{-2}: it decreases with increasing temperature (Figure 9.9) and is independent of p_{H_2}.

9.3.6 Electrode process 3 (low frequency)

R_3 has a pronounced temperature dependence, with activation energy of 0.79-0.87 eV (Figure 9.11); also the p_{H_2} dependence is strong (m = 0.46-0.54).

The equivalent capacitance (1-4·10^{-2} F cm^{-2} range) slightly decreases with temperature (Figure 9.9) and decreases with increasing p_{H_2}.

9.3.7 Comparison of impedance spectra in H_2/N_2 and H_2/Ar

In order to assess whether the Mo-BCZY electrode can be a viable cathode for electrochemical synthesis of ammonia, impedance spectra are measured in H_2/N_2 and H_2/Ar gas mixtures with approximately the same hydrogen concentration (9-10 %).

Impedance measurements at OCV taken in the two atmospheres have similar shapes (Figure 9.12) and give similar values for the fitting of the electrode process. Therefore there is no clear evidence of a selectivity of Mo as electrocatalyst toward nitrogen reduction.

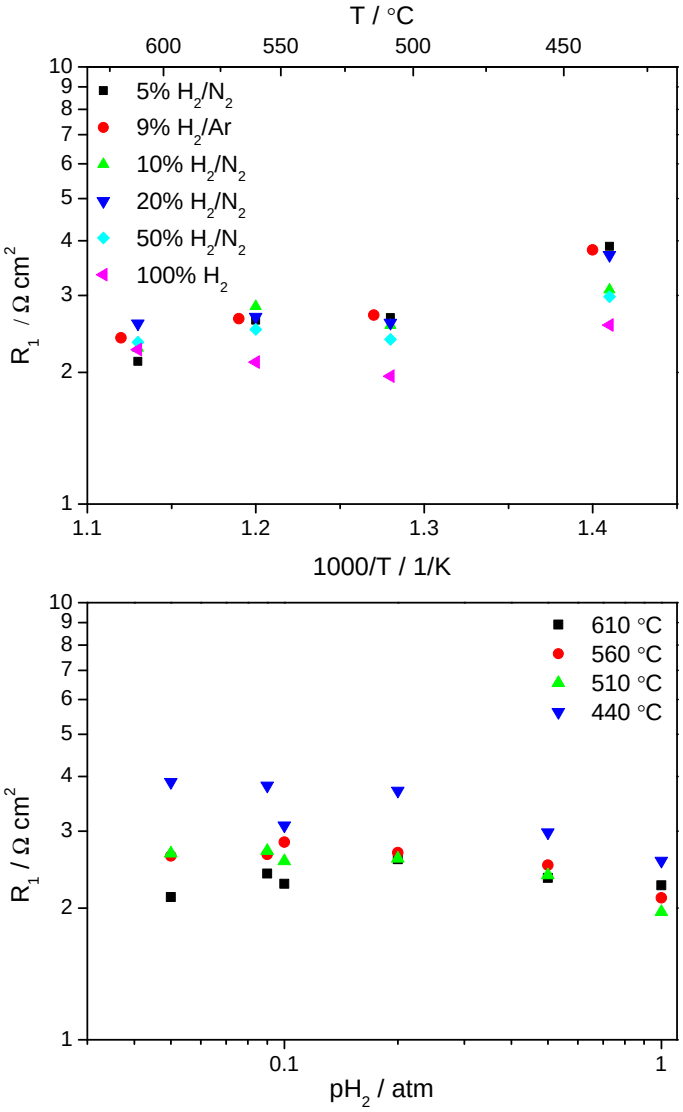

Figure 9.8: Dependence on temperature and p_{H_2} of resistance of process 1.

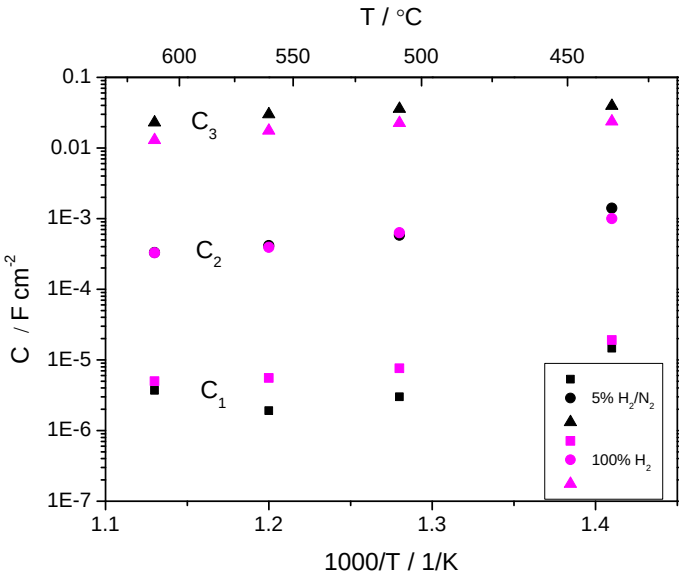

Figure 9.9: Arrhenius plot of equivalent capacitances of process 1, 2 and 3. Black symbols: 5 % H_2/N_2. Magenta symbols: 100 % H_2.

9.3.8 Electrode impedance in wet gas mixtures

After exposure to wet H_2/N_2 mixtures the impedance spectra evolve over time as shown in Figure 9.13. A $R_{el}(R_1Q_1)(R_2Q_2)(R_3Q_3)$ circuit, with R_{el} being the total electrolyte resistance (since the grain boundary arc is not visible in the frequency range investigated in wet atmosphere), has been used to fit the impedance spectra in wet reducing atmosphere. The values of n_1, n_2 and n_3 are changed to 0.64, 0.45, and 0.8 respectively to properly fit the spectra measured in wet reducing atmosphere.

Both the electrolyte resistance and R_2 decrease fast initially and then slowly over time during the first ten hours. R_3 slightly increases over the first 10 hours of exposure to wet H_2/N_2 (1 % H_2O, i.e. p_{H_2O} = 0.01 atm) but decreases significantly upon thermal cycling (taking place between 20 and 65 hours) and longer times in wet H_2/N_2 (Figure 9.14). Upon switching to wet atmosphere the capacitance of processes 2 and 3 increases, reaching respectively $5{\cdot}10^{-3}$ and $8{\cdot}10^{-2}$ F cm^{-2} (Figure 9.14).

R_1 and C_1 decrease upon switch to wet atmosphere, but because of the small values involved and the experimental difficulties explained in Section 9.3.2, it is not possible to find a clear trend over time.

After switching back to dry atmosphere (Figure 9.13d) the shape of the impedance spectra changes compared to the spectra before exposure to wet. The electrolyte resistance is the same as in Figure 9.13a, but only two semicircles are visible. Their equivalent capacitances (circa $1.1{\cdot}10^{-6}$ and 0.16 F cm^{-2}) suggest they correspond to process 1 and 3 respectively.

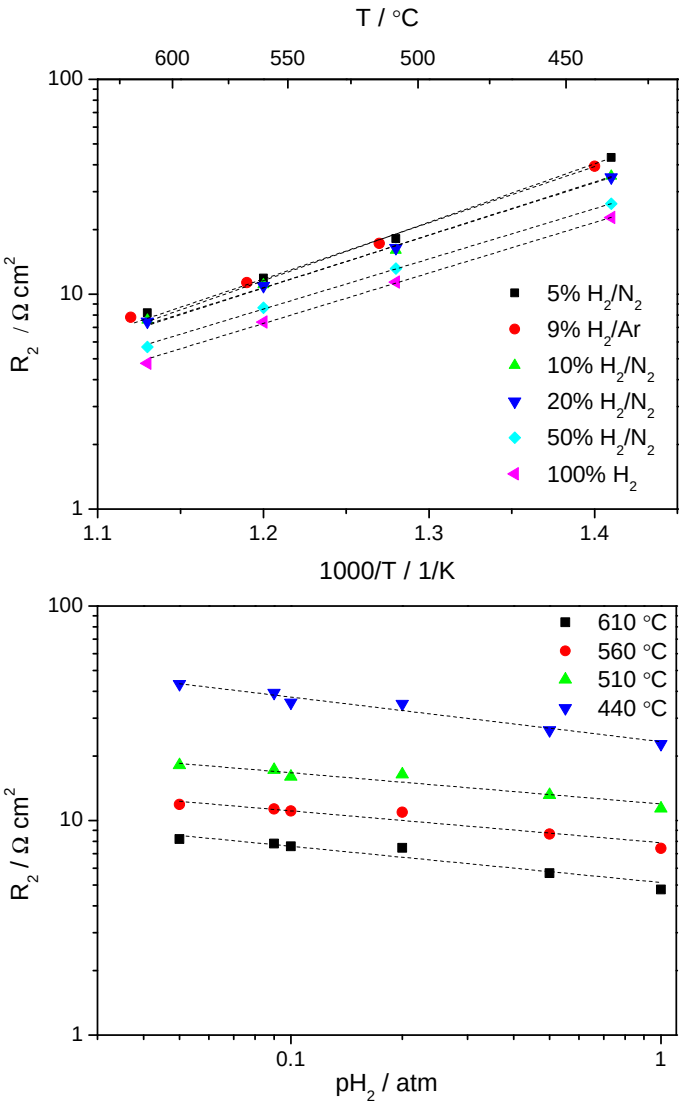

Figure 9.10: Dependence on temperature and p_{H_2} of resistance of process 2.

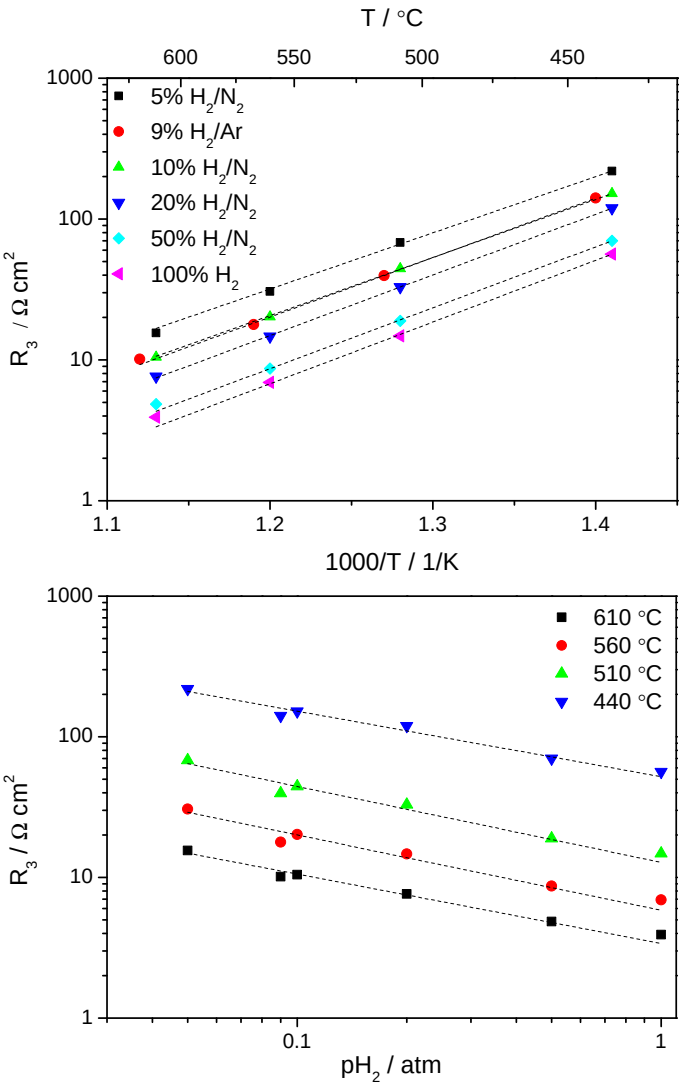

Figure 9.11: Dependence on temperature and p_{H_2} of resistance of process 3.

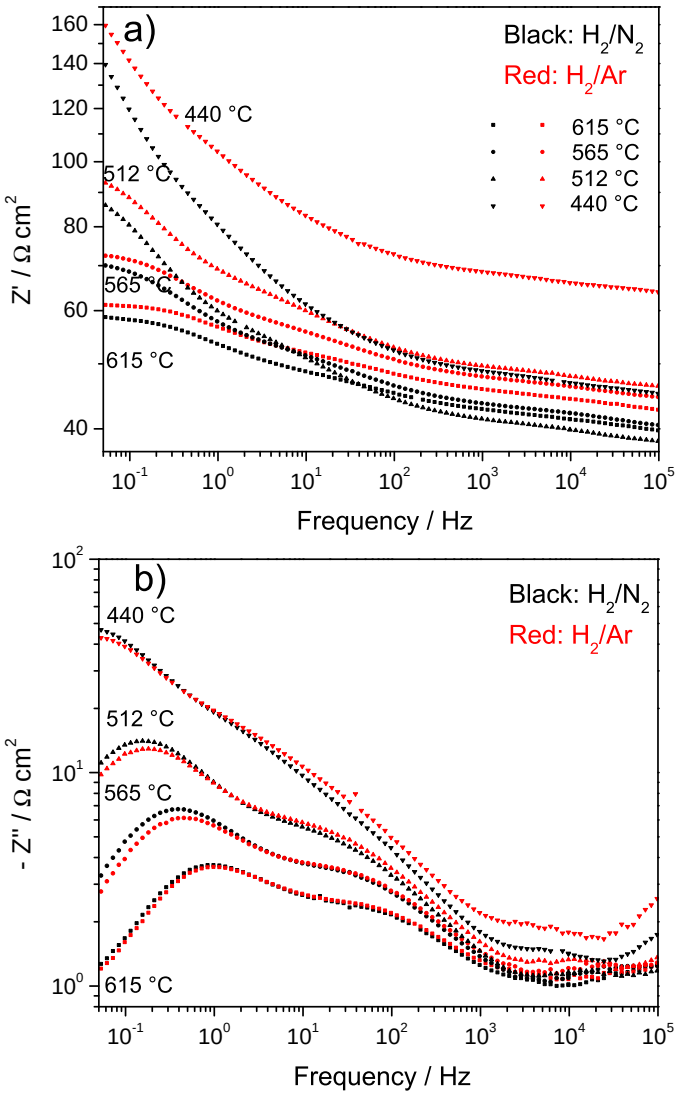

Figure 9.12: Bode plot of impedance measured in dry H_2/N_2 and H_2/Ar gas mixtures (9-10 % H_2) at different temperatures.

Process 2 is not visible instead, likely because it is overshadowed by the other electrode processes.

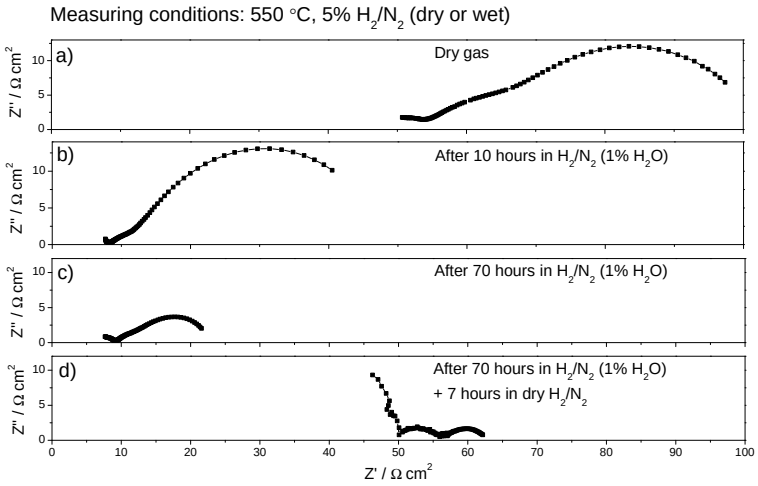

Figure 9.13: Evolution of impedance spectra over time in dry and wet 5 % H_2/N_2.

9.4 Discussion

XRD measurements (Figure 9.3) show that the phase composition of the infiltrated electrode changes upon exposure to wet reducing atmosphere: part of the Mo reacts with BCZY26 to form $BaMoO_4$.

Upon exposure to wet (p_{H_2O} = 0.01 atm) reducing atmosphere, p_{O_2} in 5 % H_2/N_2 at 550 °C increases from $9{\cdot}10^{-32}$ atm to 10^{-27} atm. According to the Ellingham diagram for molybdenum oxides, at 550 °C this increase in p_{O_2} may cause the formation of MoO_2: however it is possible that at the lower temperatures experienced by the cells during the thermal cycling the p_{O_2} of the gas exceeds the threshold value for the formation of MoO_3. The formation of MoO_3 or other volatile molybdenum oxide species is suggested by the fact that $BaMoO_4$ is detected by EDS also in parts of the cells not in direct contact with infiltrated molybdenum. This suggests that in wet reducing atmosphere molybdenum evaporates and redeposits reacting with the BCZY26 to form $BaMoO_4$.

Because of the very low p_{O_2} involved it is reasonable to expect the oxidation process to take place slowly, i.e. over many hours. This time-scale is compatible with the time scale over which the part of the impedance spectra related to process 3 show the most significant changes upon exposure to wet reducing atmosphere, suggesting the process is affected by the change of phase in the electrode.

The Nyquist plots in Figure 9.4 and 9.5 show clearly that the different features of the electrode impedance have different dependencies on hydro-

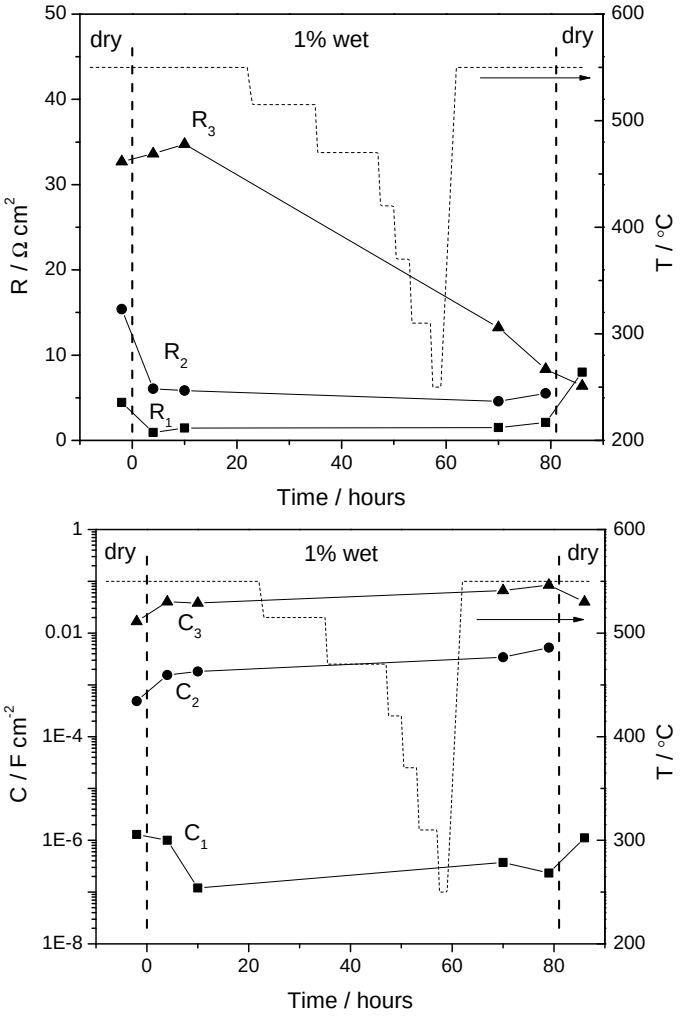

Figure 9.14: Evolution of fitting values over time in dry and wet 5 % H_2/N_2.

gen partial pressure and temperature. Thus, while it makes sense from an engineering point of view to consider the activation energy and p_{H_2} dependency of the total electrode impedance (Figure 9.7), it is better to examine each electrode process separately to understand which processes contribute to the electrode impedance.

While there is a number of works on systematic studies of the oxygen reduction reaction on cathodes for SOFCs based on oxygen ion conductors,[176–180] to the best of our knowledge there are only few systematic studies of electrode kinetics on proton conductors.[181–184] One way to help determine the rate-determining step of an electrode reaction is to consider the dependence of the electrode resistance with respect to the partial pressure of the gas involved in the reaction (p_{O_2} for oxygen electrodes, p_{H_2} for hydrogen electrodes), according to the expression $R \propto p^{-m}$. In the literature, the electrode resistance has been measured either with polarization experiments[180] or by impedance spectroscopy at OCV.[176]

In the present case, if $m = 1$ molecular hydrogen is involved in the step controlling the process whose resistance is considered.[185,186] The process could be diffusion of molecular hydrogen in the gas phase, or adsorption according to Reaction 9.5:

$$H_2(g) \leftrightarrow H_{2,ads} \; or \; 2H_{ads} \tag{9.5}$$

If instead $m = 1/2$, hydrogen atoms / protons are involved in the limiting step.[185,186] The process can be charge transfer

$$2H^+ + 2e^- \leftrightarrow H_{2,ads} \; or \; 2H_{ads} \tag{9.6}$$

or diffusion of H_{ads}.

Experimental values of m usually do not match exactly these theoretical values. This is not just due to experimental uncertainties, but to the fact that more than one process could contribute to what appears to be one single process in the impedance spectra. Moreover, it has been reported by Kek *et al.*[185,186] that the m values can be influenced by the degree of coverage of the electrode by the adsorbed species.

The evidence presented in Section 9.3.7 suggests that only hydrogen oxidation / reduction is taking place at the electrodes in this study, i.e. the electrochemical synthesis of ammonia reaction (Reaction 9.1) does not occur. Therefore only hydrogen is considered as possible active species at the electrode.

Based on the experimental observations, I suggest the following interpretation for the three electrode processes:

(a) *Process 1 (high frequency)*: fitting difficulties and experimental errors / distortions permit only general observations on this process. The

resistance is approximately constant in the 500-620 °C range, and increases at 440 °C: it exhibits the same trend as the total electrolyte resistance, which is almost constant in the temperature range 500-600 °C.[165] This, associated with the fact that R_1 decreases in wet atmosphere, suggests that the process depends on the proton conductivity of BCZY26. The capacitance is about one order of magnitude higher than the grain boundary capacitance (measured from impedance measurements at lower temperature), thus it can be ruled out that this process is related to the grain boundary impedance. Since the process is independent of p_{H_2} and depends on proton conductivity, it is here suggested that it is due to proton transfer through the BCZY26/Mo interfaces or inside the BCZY26 porous electrode backbone.

(b) *Process 2 (medium frequency)*: the resistance has an activation energy (E_a = 0.45-0.55 eV) similar to the one reported for proton conduction in BCZY.[165] Upon hydration R_2 decreases within the same timescale as the electrolyte resistance and then stays about constant over time, suggesting that the process depends on the proton concentration in BCZY26. The resistance depends on p_{H_2} (m = 0.15-0.25). The fact that the process is dependent on hydration and on p_{H_2}, associated with a capacitance of 1-10·10^{-4} F cm^{-2}, suggests that this process may be due to surface diffusion of hydrogen followed by a charge transfer.

(c) *Process 3 (low frequency)*: R_3 has a strong p_{H_2} dependence (m = 0.45-0.60), and dominates the electrode impedance at low p_{H_2}. The capacitance is very high (1-4·10^{-2} F cm^{-2}) and increases upon exposure to wet reducing atmosphere.

In SOFC cathodes, strong p_{O_2} dependence and high capacitance have been associated with molecular oxygen dissociation phenomena,[176,178] or attributed to a slow passivation phenomenon.[177] For the cells presented in this study the high capacitances could be related to an alternate oxidation/reduction process between Mo and Mo oxide upon the application of the AC signal during the test: however this is unlikely since the amplitude of the AC voltage signal (10 mV) is small and metallic Mo is well within the p_{O_2} stability range when testing in dry gas mixtures.

The capacitance is one order of magnitude higher than the value presented by Srinivasan[187] as highest possible value for hydrogen adsorption on Pt (1.6·10^{-3} F cm^{-2}), but might be related to an adsorption process if the real electrode area is considered in place of the geometrical area of the electrode.

The area of the molybdenum surface exposed to the atmosphere (and thus available for hydrogen adsorption) should be much higher than the geometrical area of the electrode, since molybdenum is present as nanoparticles in a 3D porous structure. A 8 % volume loading of Mo

(with respect to the total porous backbone volume) is calculated from the mass gain during the infiltration procedure. If an electrode thickness of 15 µm and spherical molybdenum particles with a diameter of 100 nm are considered, the real surface area of the Mo would be circa 72 cm^2 for a geometrical electrode area of 1 cm^2. Considering an experimental value of 0.05 F cm^{-2} (with respect to the geometrical area of the electrode), the real capacitance per area would be $7 \cdot 10^{-4}$ F cm^{-2}, which is below the maximum value presented by Srinivasan.[187] Thus it is feasible to assume that this process is related to hydrogen adsorption.

R_3 does not change dramatically upon switches between dry and wet atmosphere, but decreases 75 % upon long term exposure to wet reducing atmosphere: therefore it appears that the process does not depend on p_{H_2O} but is sensitive to the phase changes taking place in wet reducing atmosphere (Section 9.3.1). If the process is adsorption, the phase change from Mo to $BaMoO_4$ and eventual microstructural changes could make hydrogen adsorption easier.

Therefore, considering the high m value and the high capacitance it is here suggested that process 3 is related to adsorption of hydrogen on Mo and $BaMoO_4$.

9.5 Conclusions

Symmetrical cells with composite Mo-BCZY electrodes are produced by screen printing and infiltration. Metallic molybdenum is formed upon reduction at 900 °C in dry H_2 and is partially oxidized to $BaMoO_4$ after exposure to wet reducing atmosphere. The cells are studied systematically by impedance spectroscopy at OCV in dry H_2/N_2 and H_2/Ar mixtures.

There are no significant differences between the electrode impedance in H_2/N_2 and H_2/Ar, suggesting that Mo is not an active electrocatalyst for nitrogen reduction to ammonia at open circuit voltage (i.e. without DC polarization).

The electrode impedance in hydrogen consists of three processes, going from high frequency to low frequency:

- Process 1 depends on proton conductivity and is independent on p_{H_2}. It is suggested that it is due to proton transfer through the BCZY26/Mo interface or inside the BCZY26 porous backbone.
- Process 2 depends on proton conductivity and on p_{H_2} and has a capacitance of 1-$10 \cdot 10^{-4}$ F cm^{-2}, and it is assigned to surface diffusion of hydrogen followed by a charge transfer.
- Process 3 has a strong p_{H_2} dependence and a high capacitance (1-$4 \cdot 10^{-2}$ F cm^{-2}). It is suggested that it is related to adsorption of

hydrogen on Mo/$BaMoO_4$.

Chapter 10

Summary, conclusions and outlook

10.1 Summary and conclusions

In this thesis three classes of materials (iron oxides / oxyhydroxides, pyrophosphates, Y-doped $BaCeO_3$-$BaZrO_3$) are studied as proton conductors, either experimentally or by means of calculations. Despite differences in the conduction mechanism among them, in all cases proton conductivity is heavily dependent on water partial pressure.

Neither ferroxanes-derived materials (Chapter 2) nor pyrophosphates (Chapters 3, 4 and 5) are considered suitable for electrochemical synthesis of ammonia: a high temperature solid state proton conductor (BCZY26, Chapter 6) is chosen as electrolyte, based on its proton conductivity ($>10^{-4}$ S/cm at 400 °C in dry H_2/Ar) and its well known defect chemistry.

A new cell concept, based on infiltration of a porous BCZY ceramic backbone with a solution containing metal ions, is tested successfully to produce composite metal/BCZY electrodes using Fe and Mo as metals. This type of cell can be used as a platform for screening of electrocatalysts.

Because of degradation issues and experimental uncertainties it is not possible to evaluate with certainty if the small differences in the impedance spectra of Fe-BCZY electrodes, measured at OCV in H_2/N_2 and H_2/Ar, are related to different reactions taking place in the two atmospheres, i.e. to iron being active towards nitrogen reduction to ammonia.

For the Mo-BCZY electrodes no significant differences are visible in the impedance spectra measured in H_2/N_2 and H_2/Ar (Chapter 9, Figure 9.12), indicating that Mo is not an active electrocatalyst for nitrogen reduction to ammonia at open circuit voltage.

Summarising, the measurements at OCV (i.e. without electrode polarisation) do not show any clear evidence of activity of Fe and Mo supported on BCZY toward nitrogen reduction to ammonia. However in this thesis work

it has not been possible to cover all the possible experimental parameters, such as polarisation and pressure. The effect of these parameters should therefore be addressed in future work.

Nonetheless, the detailed electrode characterization carried out permits to study in detail, to the best of my knowledge for the first time, the hydrogen reaction on Fe and Mo electrodes on a solid state proton conductor. The Fe-BCZY electrode shows promisingly low polarization resistance in wet H_2/N_2 gas mixtures, which suggests that it could have potential as hydrogen electrode for PCFCs (see Section 8.4). The electrode impedance of Mo-BCZY electrodes is modeled with an equivalent circuit and a tentative interpretation of the mechanisms behind the three processes identified in the impedance spectra is given.

10.2 Outlook

The next step necessary to complete the assessment of the potential of Fe and Mo as electrocatalysts for synthesis of ammonia is to study composite Fe-BCZY and Mo-BCZY electrodes under polarization.

Within the work carried out during this PhD study button cells with Fe-BCZY and Mo-BCZY electrodes have been fabricated on anode-supported half cells provided by Coorstek Inc. (BZY10-NiO cermet anode, 10 µm BZY10 electrolyte) to be studied under polarization. However, the brittleness of the cells has led repeatedly to mechanical failure, thus it has not been possible to carry out reliable measurements under polarization and the preliminary measurements have not been inserted in this thesis. Therefore the next step in electrocatalyst testing will require first the development of cells with higher mechanical strength.

Using a dual chamber experimental setup, i.e. separating the atmospheres at the two electrodes, would be helpful in studying electrochemical ammonia synthesis. Such a setup, allowing tests in a 1-100 bars pressure range, is now available in the laboratories of DTU Energy Conversion: it will therefore be possible to study also the effect of pressure on the electrode reactions. The use of a dual chamber setup could allow using humidified gases on the hydrogen-electrode side, thus improving the proton conductivity of the electrolyte. However, it is possible that BCZY would hydrate on the hydrogen-electrode side and dehydrate on the nitrogen-side of the cell, thus transferring water from one side of the cell to the other and potentially poisoning the electrocatalysts on the nitrogen side. Whether or not this process takes place (and whether or not it affects ammonia formation) must be addressed experimentally: therefore it will be necessary to carry out tests using both dry and humidified hydrogen at the hydrogen electrode.

Bibliography

[1] *Energy Strategy 2050 - from coal, oil and gas to green energy*; 2011.

[2] Mogensen, M. et al. Electrolysis for Integration of Renewable Electricity and Routes towards Sustainable Fuels. 10th International Workshop on Large-Scale Integration of Wind Power into Power Systems as well as on Transmission Networks for Offshore Wind Farms. Aarhus, Denmark, 2011.

[3] Zamfirescu, C.; Dincer, I. *Journal of Power Sources* **2008**, *185*, 459–465.

[4] Graves, C. R. Recycling CO_2 into Sustainable Hydrocarbon Fuels : Electrolysis of CO_2 and H_2O. Ph.D. thesis, Columbia University, 2010.

[5] Hallinder, J. Electrolytes and Electrodes for Electrochemical Cells Operating at 200 - 300 °C. PhD thesis, Technical University of Denmark, 2013.

[6] Kelly, T.; Matos, G. *Historical statistics for mineral and material commodities in the United States: U.S. Geological Survey Data Series 140*; 2011.

[7] Amar, I. A.; Lan, R.; Petit, C. T. G.; Tao, S. *Journal of Solid State Electrochemistry* **2011**, *15*, 1845–1860.

[8] Green Jr, L. *International Journal of Hydrogen Energy* **1982**, *7*, 355–359.

[9] Thomas, G.; Parks, G. *Potential Roles of Ammonia in a Hydrogen Economy*; 2006.

[10] Lan, R.; Irvine, J. T.; Tao, S. *International Journal of Hydrogen Energy* **2012**, *37*, 1482–1494.

[11] Christensen, C. H.; Sørensen, R. Z.; Johannessen, T.; Quaade, U. J.; Honkala, K.; Elmøe, T. D.; Køhler, R.; Nørskov, J. K. *Journal of Materials Chemistry* **2005**, *15*, 4106–4108.

[12] *CRC Handbook of Chemistry and Physics*, 93rd ed.; CRC press, 2012.

[13] Howalt, J. G.; Bligaard, T.; Rossmeisl, J.; Vegge, T. *Physical chemistry chemical physics : PCCP* **2013**, *15*, 7785–95.

[14] Modak, J. M. *Resonance* **2002**, 69–77.

[15] Lan, R.; Irvine, J. T. S.; Tao, S. *Scientific reports* **2013**, *3*, 1145.

[16] Hellman, A. et al. *Journal of Physical Chemistry B* **2006**, *110*, 17719–35.

[17] Klerke, A.; Christensen, C. H.; Nørskov, J. K.; Vegge, T. *Journal of Materials Chemistry* **2008**, *18*, 2304–2310.

[18] *Energy Efficiency and CO_2 Emissions in Ammonia Production: 2008-2009 Summary Report, International Fertilizer Industry Association, Technical Report*; 2009.

[19] Gosnell, J. Efficient Ammonia Production. 2005.

[20] Marnellos, G.; Stoukides, M. *Science* **1998**, *282*, 98–100.

[21] Skodra, A.; Stoukides, M. *Solid State Ionics* **2009**, *180*, 1332–1336.

[22] Kordali, V.; Kyriacou, G.; Lambrou, C. *Chemical Communications* **2000**, 1673–1674.

[23] Liu, R.; Xu, G. *Chinese Journal of Chemistry* **2010**, *28*, 139–142.

[24] Xu, G.; Liu, R. *Chinese Journal of Chemistry* **2009**, *27*, 677–680.

[25] Xu, G.; Liu, R.; Wang, J. *Science in China Series B: Chemistry* **2009**, *52*, 1171–1175.

[26] Marnellos, G.; Zisekas, S.; Stoukides, M. *Journal of Catalysis* **2000**, *193*, 80–87.

[27] Ouzounidou, M.; Skodra, A.; Kokkofitis, C.; Stoukides, M. *Solid State Ionics* **2007**, *178*, 153–159.

[28] Skodra, A.; Ouzounidou, M.; Stoukides, M. *Solid State Ionics* **2006**, *177*, 2217–2220.

[29] Liu, R.; Xie, Y.; Wang, J.; Li, Z.; Wang, B. *Solid State Ionics* **2006**, *177*, 73–76.

[30] Wang, X.; Yin, J.; Xu, J.; Wang, H.; Ma, G. *Chinese Journal of Chemistry* **2011**, *29*, 1114–1118.

[31] Yin, J.; Wang, X.; Xu, J.; Wang, H.; Zhang, F.; Ma, G. *Solid State Ionics* **2011**, *185*, 6–10.

[32] Zhang, M.; Xu, J.; Ma, G. *Journal of Materials Science* **2011**, *46*, 4690–4694.

[33] Zhang, F.; Yang, Q.; Pan, B.; Xu, R.; Wang, H.; Ma, G. *Materials Letters* **2007**, *61*, 4144–4148.

[34] Wang, W.; Cao, X.; Gao, W.; Zhang, F.; Wang, H.; Ma, G. *Journal of Membrane Science* **2010**, *360*, 397–403.

[35] Wang, W.; Liu, J.; Li, Y.; Wang, H.; Zhang, F.; Ma, G. *Solid State Ionics* **2010**, *181*, 667–671.

[36] Liu, J.; Li, Y.; Wang, W.; Wang, H.; Zhang, F.; Ma, G. *Journal of Materials Science* **2010**, *45*, 5860–5864.

[37] Chen, C.; Ma, G. *Journal of Alloys and Compounds* **2009**, *485*, 69–72.

[38] Chen, C.; Ma, G. *Journal of Materials Science* **2008**, *43*, 5109–5114.

[39] Amar, I. A.; Petit, C. T.; Zhang, L.; Lan, R.; Skabara, P. J.; Tao, S. *Solid State Ionics* **2011**, *201*, 94–100.

[40] Amar, I. A.; Lan, R.; Petit, C. T.; Arrighi, V.; Tao, S. *Solid State Ionics* **2011**, *182*, 133–138.

[41] Murakami, T.; Nishikiori, T.; Nohira, T.; Ito, Y. *Journal of the American Chemical Society* **2003**, *125*, 334–5.

[42] Murakami, T.; Nishikiori, T.; Nohira, T.; Ito, Y. *Electrochemical and Solid-State Letters* **2005**, *8*, D19–D21.

[43] Murakami, T.; Nohira, T.; Goto, T.; Ogata, Y. H.; Ito, Y. *Electrochimica Acta* **2005**, *50*, 5423–5426.

[44] Murakami, T.; Nohira, T.; Ogata, Y. H.; Ito, Y. *Electrochemical and Solid-State Letters* **2005**, *8*, D12–D14.

[45] Murakami, T.; Nohira, T.; Ogata, Y. H.; Ito, Y. *Journal of The Electrochemical Society* **2005**, *152*, D109–D112.

[46] Murakami, T.; Nishikiori, T.; Nohira, T.; Ito, Y. *Journal of The Electrochemical Society* **2005**, *152*, D75–D78.

[47] Murakami, T.; Nohira, T.; Araki, Y.; Goto, T.; Hagiwara, R.; Ogata, Y. H. *Electrochemical and Solid-State Letters* **2007**, *10*, E4–E6.

[48] Denvir, A.; Murphy, O.; Cisar, A. J.; Robertson, P.; Uselton, K. USA Patent US 20030164292A1, Electrochemical synthesis of ammonia. 2003.

[49] Denvir, A.; Murphy, O.; Cisar, A. J.; Robertson, P.; Uselton, K. USA Patent US 6881308 B2, Electrochemical synthesis of ammonia. 2005.

[50] Logadottir, A.; Rod, T. H.; Nø rskov, J.; Hammer, B.; Dahl, S.; Jacobsen, J. H. *Journal of Catalysis* **2001**, *197*, 229–231.

[51] Skúlason, E.; Bligaard, T.; Gudmundsdóttir, S.; Studt, F.; Rossmeisl, J.; Abild-Pedersen, F.; Vegge, T.; Jónsson, H.; Nørskov, J. K. *Physical Chemistry Chemical Physics* **2012**, *14*, 1235–45.

[52] Howalt, J. G.; Vegge, T. *In preparation*

[53] Sone, Y.; Edkunge, P.; Simonsson, D. *Journal of The Electrochemical Society* **1996**, *143*, 1254–1259.

[54] Tsui, E. M.; Cortalezzi, M. M.; Wiesner, M. R. *Journal of Membrane Science* **2007**, *306*, 8–15.

[55] Tsui, E. M.; Wiesner, M. R. *Journal of Membrane Science* **2008**, *318*, 79–83.

[56] Rose, J.; Cortalezzi-Fidalgo, M. M.; Moustier, S.; Magnetto, C.; Jones, C. D.; Barron, A. R.; Wiesner, M. R.; Bottero, J.-Y. *Chemistry of Materials* **2002**, *14*, 621–628.

[57] Zhang, L. Synthesis and characterization of novel proton-conductive composite membranes derived from the hybridization of metal oxyhydroxide nanoparticles and organic polymers for fuel cell applications. Master Thesis, Duke University, 2010.

[58] Guo, H.; Barnard, A. S. *Physical Chemistry Chemical Physics* **2011**, *13*, 17864–17869.

[59] Refait, P.; Génin, J.-M. *Corrosion Science* **1993**, *34*, 797–819.

[60] Colomer, M.; Zenzinger, K. *Microporous and Mesoporous Materials* **2012**, *161*, 123–133.

[61] Colomer, M. *Journal of Power Sources* **2011**, *196*, 8280–8285.

[62] Ye, X.; Lin, D.; Jiao, Z.; Zhang, L. *Journal of Physics D: Applied Physics* **1998**, *31*, 2739–2744.

[63] Barsoukov, E., Macdonald, J. R., Eds. *Impedance Spectroscopy: Theory, Experiment, and Applications*, 2nd ed.; Wiley-Interscience, 2005; p 606.

[64] Cortalezzi, M. M.; Rose, J.; Wells, G. F.; Bottero, J.-Y.; Barron, A. R.; Wiesner, M. R. *Journal of Membrane Science* **2003**, *227*, 207–217.

[65] Colomer, M.; Anderson, M. *Journal of Non-Crystalline Solids* **2001**, *290*, 93–104.

[66] Colomban, P. *Proton Conductors: Solids, Membranes and Gels - Materials and Devices*; Cambridge University Press, 1992.

[67] Jin, Y.; Shen, Y.; Hibino, T. *Journal of Materials Chemistry* **2010**, *20*, 6214–6217.

[68] Nagao, M.; Kamiya, T.; Heo, P.; Tomita, A.; Hibino, T.; Sano, M. *Journal of The Electrochemical Society* **2006**, *153*, A1604–A1609.

[69] Sun, X.; Wang, S.; Wang, Z.; Ye, X.; Wen, T.; Huang, F. *Solid State Ionics* **2008**, *179*, 1138–1141.

[70] Thakkar, R.; Patel, H.; Chudasama, U. *Bulletin of Materials Science* **2007**, *30*, 205–209.

[71] Chen, X.; Wang, C.; Payzant, E. A.; Xia, C.; Chu, D. *Journal of The Electrochemical Society* **2008**, *155*, B1264–B1269.

[72] Paschos, O.; Kunze, J.; Stimming, U.; Maglia, F. *Journal of Physics: Condensed Matter* **2011**, *23*, 234110.

[73] Genzaki, K.; Heo, P.; Sano, M.; Hibino, T. *Journal of The Electrochemical Society* **2009**, *156*, B806–B810.

[74] Wu, X.; Verma, A.; Scott, K. *Fuel Cells* **2008**, *8*, 453–458.

[75] Wang, H.; Zhang, H.; Xiao, G.; Zhang, F.; Yu, T.; Xiao, J.; Ma, G. *Journal of Power Sources* **2011**, *196*, 683–687.

[76] Le, M.-V.; Tsai, D.-S.; Yang, C.-Y.; Chung, W.-H.; Lee, H.-Y. *Electrochimica Acta* **2011**, *56*, 6654–6660.

[77] Nalini, V.; Amezawa, K.; Xing, W.; Norby, T. *Journal of The Electrochemical Society* **2010**, *157*, B1491–B1498.

[78] Lan, R.; Tao, S. *Journal of Alloys and Compounds* **2009**, *486*, 380–385.

[79] Nagao, M.; Takeuchi, A.; Heo, P.; Hibino, T.; Sano, M.; Tomita, A. *Electrochemical and Solid-State Letters* **2006**, *9*, A105–A109.

[80] Einsla, M. L.; Mukundan, R.; Brosha, E. L.; Garzon, F. H. Synthesis and Conductivity of Indium-Doped Tin Pyrophosphates. ECS Transactions. 2007; pp 347–355.

[81] Wang, H.; Xiao, J.; Zhou, Z.; Zhang, F.; Zhang, H.; Ma, G. *Solid State Ionics* **2010**, *181*, 1521–1524.

[82] Makart, H. *Helvetica Chimica Acta* **1967**, *50*, 399–405.

[83] Poojary, D.; Borade, R.; Campbell, F.; Clearfield, A. *Journal of Solid State Chemistry* **1994**, *112*, 106–112.

[84] Matsui, T.; Kukino, T.; Kikuchi, R.; Eguchi, K. *Electrochemical and Solid-State Letters* **2005**, *8*, A256–A258.

[85] Matsui, T.; Muroyama, H.; Kikuchi, R.; Eguchi, K. *Journal of the Japan Petroleum Institute* **2010**, *53*, 1–11.

[86] Gover, R.; Withers, N.; Allen, S.; Withers, R.; Evans, J. *Journal of Solid State Chemistry* **2002**, *166*, 42–48.

[87] Teranishi, S.; Kondo, K.; Nishida, M.; Kanematsu, W.; Hibino, T. *Electrochemical and Solid-State Letters* **2009**, *12*, J73–J76.

[88] Onoda, H.; Inagaki, Y.; Kuwabara, A.; Kitamura, N.; Amezawa, K.; Nakahira, A.; Tanaka, I. *Journal of Ceramic Processing Research* **2010**, *11*, 344–347.

[89] White, K. M.; Lee, P. L.; Chupas, P. J.; Chapman, K. W.; Payzant, E. A.; Jupe, A. C.; Bassett, W. A.; Zha, C.-S.; Wilkinson, A. P. *Chemistry of Materials* **2008**, *20*, 3728–3734.

[90] Chatzichristodoulou, C.; Hallinder, J.; Lapina, A.; Holtappels, P.; Mogensen, M. *Journal of the Electrochemical Society* **2013**, *160*, F798–F805.

[91] Shirai, T.; Satou, S.; Saito, Y.; Saito, M.; Kuwano, J.; Shiroishi, H. *Phosphorus Research Bulletin* **2007**, *21*, 31–37.

[92] Shirai, T.; Satou, S.; Saito, M.; Kuwano, J.; Shiroishi, H. *Solid State Ionics* **2009**, *180*, 569–574.

[93] Li, Y.; Kunitake, T.; Aoki, Y.; Muto, E. *Advanced Materials* **2008**, *20*, 2398–2404.

[94] Park, C.-J.; Kim, D.-H.; Kim, J.-K.; Lee, J.-S.; Song, S.-J. *Journal of The Electrochemical Society* **2009**, *156*, E23–E25.

[95] Yang, C.; Costamagna, P.; Srinivasan, S.; Benziger, J.; Bocarsly, A. B. *Journal of Power Sources* **2001**, *103*, 1–9.

[96] Hsiao, C. Y.; Selman, R. *Solid State Ionics* **1997**, *98*, 33–38.

[97] Tanasini, P.; Cannarozzo, M.; Costamagna, P.; Faes, A.; Herle, J. V.; Comninellis, C. *Fuel Cells* **2009**, *9*, 740–752.

[98] Norby, T. *Solid State Ionics* **1999**, *125*, 1–11.

[99] Phadke, S. R.; Bowers, C. R.; Wachsman, E. D.; Nino, J. C. *Solid State Ionics* **2011**, *183*, 26–31.

[100] Tomita, A.; Kajiyama, N.; Kamiya, T.; Nagao, M.; Hibino, T. *Journal of The Electrochemical Society* **2007**, *154*, B1265–B1269.

[101] Tanimoto, S.; Hirukawa, S.; Shirai, T.; Sato, S.; Kusano, T.; Saito, M.; Kuwano, J.; Shiroishi, H. *Key Engineering Materials* **2009**, *388*, 57–60.

[102] Jin, Y.; Lee, B.; Hibino, T. *Journal of the Japan Petroleum Institute* **2010**, *53*, 12–23.

[103] Nalini, V.; Haugsrud, R.; Norby, T. *Solid State Ionics* **2010**, *181*, 510–516.

[104] Nalini, V.; Sørby, M. H.; Amezawa, K.; Haugsrud, R.; Fjellvåg, H.; Norby, T. *Journal of the American Ceramic Society* **2011**, *94*, 1514–1522.

[105] Miyazaki, K.; Kato, Y.; Matsui, T.; Hayashi, S.; Iriyama, Y.; Fukutsuka, T.; Abe, T.; Ogumi, Z. *Physical Chemistry Chemical Physics* **2012**, *14*, 11135–8.

[106] Tran, A.; Duke, M.; Gray, P.; Diniz da Costa, J. *Developments in Chemical Engineering & Mineral Processing* **2006**, *14*, 101–118.

[107] Norberg, S. T.; Svensson, G.; Albertsson, J. *Acta Crystallographica Section C Crystal Structure Communications* **2001**, *57*, 225–227.

[108] Ohtsuka, H.; Aomura, K. *Bulletin of The Japan Petroleum Institute* **1962**, *4*, 3–14.

[109] Hwang, M. J.; Lee, S. Y.; Han, C. S. *Journal of Nanoscience and Nanotechnology* **2006**, *6*, 3491–3493.

[110] Huang, Y.; Li, Q.; Jensen, A. H.; Yin, M.; Jensen, J. O.; Christensen, E.; Pan, C.; Bjerrum, N. J.; Xing, W. *Journal of Materials Chemistry* **2012**, *22*, 22452–22458.

[111] Harrison, D. E.; Hummel, F. A. *Journal of the American Ceramic Society* **1959**, *42*, 487–490.

[112] Bamberger, C. E.; Begun, G. M. *Journal of the Less Common Metals* **1987**, *134*, 201–206.

[113] Schmidt, T. J. Durability and Degradation in High-Temperature Polymer Electrolyte Fuel Cells. ECS Transactions. 2006; pp 19–31.

[114] Brown, E. H.; Whitt, C. D. *Industrial & Engineering Chemistry* **1952**, *44*, 615–618.

[115] Kreller, C. R.; Wilson, M. S.; Mukundan, R.; Brosha, E. L.; Garzon, F. H. Proton Conductivity and Stability of In^{3+} doped SnP_2O_7 with Varying P:M. ECS PRIME 2012. Honolulu, Hawaii, USA, 2012.

[116] Kwon, K.; Yano, M.; Sun, H.; Park, J. USA Patent US 20050221143, Proton conductor for fuel cell. 2005.

[117] Tran, A. T. T.; Duke, M. C.; Gray, P. G.; Diniz Da Costa, J. C. *International Journal of Modern Physics B* **2006**, *20*, 4147–4152.

[118] Wang, H.; Liu, J.; Wang, W.; Ma, G. *Journal of Power Sources* **2010**, *195*, 5596–5600.

[119] Kitamura, N.; Amezawa, K.; Tomii, Y.; Hanada, T.; Yamamoto, N.; Omata, T.; Otsuka-Yao-Matsuo, S. *Journal of The Electrochemical Society* **2005**, *152*, A658–A663.

[120] Onoda, H.; Inagaki, Y.; Kuwabara, A.; Kitamura, N.; Amezawa, K.; Nakahira, A.; Tanaka, I.; Nakaragi-cyo, S.; Chemistry, A.; Group, B. *Phosphorus Research Bulletin* **2009**, *23*, 20–24.

[121] Singh, B.; Im, H.-N.; Park, J.-Y.; Song, S.-J. *Journal of the Electrochemical Society* **2012**, *159*, F819–F825.

[122] Singh, B.; Im, H.-N.; Park, J.-Y.; Song, S.-J. *The Journal of Physical Chemistry C* **2013**, *117*, 2653–2661.

[123] Muroyama, H.; Kudo, K.; Matsui, T.; Kikuchi, R.; Eguchi, K. *Solid State Ionics* **2007**, *178*, 1512–1516.

[124] Tsuhako, M.; Ikeuchi, S.; Matsuo, T.; Motooka, I.; Kobayash, M. *Chemistry Letters* **1977**, 195–198.

[125] Masui, T.; Hirai, H.; Imanaka, N.; Adachi, G. *Physica Status Solidi (a)* **2003**, *198*, 364–368.

[126] Tao, S. *Solid State Ionics* **2009**, *180*, 148–153.

[127] Xu, X.; Tao, S.; Irvine, J. T. *Solid State Ionics* **2009**, *180*, 343–350.

[128] Iwahara, H.; Esaka, T.; Uchida, H.; Maeda, N. *Solid State Ionics* **1981**, *3-4*, 359–363.

[129] Iwahara, H.; Uchida, H.; Maeda, N. *Journal of Power Sources* **1982**, *7*, 293–301.

[130] Iwahara, H. *Journal of The Electrochemical Society* **1988**, *135*, 529–533.

[131] Iwahara, H. *Solid State Ionics* **1988**, *28-30*, 573–578.

[132] Fabbri, E.; Bi, L.; Pergolesi, D.; Traversa, E. *Advanced Materials* **2012**, *24*, 195–208.

[133] Fabbri, E.; Pergolesi, D.; Traversa, E. *Chemical Society Reviews* **2010**, *39*, 4355–69.

[134] Malavasi, L.; Fisher, C. A. J.; Islam, M. S. *Chemical Society Reviews* **2010**, *39*, 4370–87.

[135] Kreuer, K. *Annual Review of Materials Research* **2003**, *33*, 333–359.

[136] Kreuer, K.-D. *Chemistry of Materials* **1996**, *8*, 610–641.

[137] Bonanos, N. *Solid State Ionics* **2001**, *145*, 265–274.

[138] Nowick, A.; Du, Y. *Solid State Ionics* **1995**, *77*, 137–146.

[139] Kreuer, K. *Solid State Ionics* **2000**, *136-137*, 149–160.

[140] Iwahara, H.; Yajima, T.; Hibino, T.; Ozaki, K.; Suzuki, H. *Solid State Ionics* **1993**, *61*, 65–69.

[141] Iwahara, H. *Solid State Ionics* **1996**, *86-88*, 9–15.

[142] Yajima, T.; Suzuki, H.; Yogo, T.; Iwahara, H. *Solid State Ionics* **1992**, *51*, 101–107.

[143] Scholten, M. J.; Schoonman, J.; Van Milterburg, J. C.; Oonk, H. A. J. No Title. Proceedings of the Third International Symposium on Solid Oxide Fuel Cells, The Electrochemical Society Proceedings. 1993; pp 146–155.

[144] Tanner, C. W.; Virkar, A. V. *Journal of The Electrochemical Society* **1996**, *143*, 1386–1389.

[145] Kreuer, K. *Solid State Ionics* **1997**, *97*, 1–15.

[146] Fabbri, E.; Pergolesi, D.; Traversa, E. *Science and Technology of Advanced Materials* **2010**, *11*, 044301.

[147] Kreuer, K. *Solid State Ionics* **1999**, *125*, 285–302.

[148] Babilo, P.; Uda, T.; Haile, S. M. *Journal of Materials Research* **2007**, *22*, 1322–1330.

[149] Ricote, S.; Caboche, G.; Estournes, C.; Bonanos, N. *Journal of Nanomaterials* **2008**, *2008*, 1–5.

[150] Anselmi-Tamburini, U.; Buscaglia, M.; Viviani, M.; Bassoli, M.; Bottino, C.; Buscaglia, V.; Nanni, P.; Munir, Z. *Journal of the European Ceramic Society* **2006**, *26*, 2313–2318.

[151] Stuart, P. A.; Unno, T.; Ayres-Rocha, R.; Djurado, E.; Skinner, S. J. *Journal of the European Ceramic Society* **2009**, *29*, 697–702.

[152] Khani, Z.; Taillades-Jacquin, M.; Taillades, G.; Marrony, M.; Jones, D. J.; Rozière, J. *Journal of Solid State Chemistry* **2009**, *182*, 790–798.

[153] Ricote, S.; Bonanos, N.; Manerbino, A.; Coors, W. *International Journal of Hydrogen Energy* **2012**, *37*, 7954–7961.

[154] Ricote, S.; Bonanos, N. *Solid State Ionics* **2010**, *181*, 694–700.

[155] Duval, S.; Holtappels, P.; Stimming, U.; Graule, T. *Solid State Ionics* **2008**, *179*, 1112–1115.

[156] Babilo, P.; Haile, S. M. *Journal of the American Ceramic Society* **2005**, *88*, 2362–2368.

[157] Fabbri, E.; D'Epifanio, A.; Di Bartolomeo, E.; Licoccia, S.; Traversa, E. *Solid State Ionics* **2008**, *179*, 558–564.

[158] Haile, S. M.; Staneff, G.; Ryu, K. H. *Journal of Materials Science* **2001**, *6*, 1149–1160.

[159] Poulsen, F. W. *Journal of Solid State Chemistry* **1999**, *143*, 115–121.

[160] Bonanos, N.; Poulsen, F. W. *Journal of Materials Chemistry* **1999**, *9*, 431–434.

[161] Ricote, S.; Caboche, G.; Heintz, O. *Journal of Applied Electrochemistry* **2009**, *39*, 553–557.

[162] Coors, W. G. In *Advances in Ceramics - Synthesis and Characterization, Processing and Specific Applications*; Sikalidis, C., Ed.; InTech, 2011; Chapter 22, pp 501–520.

[163] Schober, T.; Schilling, W.; Wenzl, H. *Solid State Ionics* **1996**, *86-88*, 653–658.

[164] Oishi, M.; Akoshima, S.; Yashiro, K.; Sato, K.; Mizusaki, J.; Kawada, T. *Solid State Ionics* **2008**, *179*, 2240–2247.

[165] Ricote, S.; Bonanos, N.; Wang, H.; Haugsrud, R. *Solid State Ionics* **2011**, *185*, 11–17.

[166] Appl, M. *Ullmann's Encyclopedia of Industrial Chemistry*; Wiley-VCH, 2006; p 153.

[167] Xie, Y.-H.; Wang, J.-D.; Liu, R.-Q.; Su, X.-T.; Sun, Z.-P.; Li, Z.-J. *Solid State Ionics* **2004**, *168*, 117–121.

[168] Jacobsen, C. J. H. *Chemical Communications* **2000**, 1057–1058.

[169] Klinsrisuk, S.; Irvine, J. *Solid State Ionics* **2010**, *181*, 168–172.

[170] Høgh, J. Influence of impurities on the H_2 / H_2O / Ni / YSZ electrode. PhD thesis, DTU, 2005.

[171] Dees, D. W.; Claar, T. D.; Easler, T. E.; Fee, D. C.; C, M. F. *Journal of The Electrochemical Society* **1987**, *134*, 2141–2146.

[172] Hibino, T.; Hashimoto, A.; Suzuki, M.; Sano, M. *Journal of The Electrochemical Society* **2002**, *149*, A1503–A1508.

[173] Klemensø, T.; Thydén, K.; Chen, M.; Wang, H.-J. *Journal of Power Sources* **2010**, *195*, 7295–7301.

[174] Graves, C. RAVDAV data analysis software, version 0.9.7, 2012.

[175] Fleig, J. *Solid State Ionics* **2002**, *150*, 181–193.

[176] Escudero, M.; Aguadero, A.; Alonso, J.; Daza, L. *Journal of Electroanalytical Chemistry* **2007**, *611*, 107–116.

[177] Jørgensen, M. J.; Mogensen, M. *Journal of The Electrochemical Society* **2001**, *148*, A433–A442.

[178] Mauvy, F.; Lalanne, C.; Bassat, J.-M.; Grenier, J.-C.; Zhao, H.; Huo, L.; Stevens, P. *Journal of The Electrochemical Society* **2006**, *153*, A1547–A1553.

[179] Yang, Y. L.; Chen, C. L.; Chen, S. Y.; Chu, C. W.; Jacobson, a. J. *Journal of The Electrochemical Society* **2000**, *147*, 4001–4007.

[180] Takeda, Y.; Kanno, R.; Noda, M.; Tomida, Y.; Yamamoto, O. *Journal of The Electrochemical Society* **1987**, *134*, 2656–2661.

[181] Dailly, J.; Fourcade, S.; Largeteau, A.; Mauvy, F.; Grenier, J.; Marrony, M. *Electrochimica Acta* **2010**, *55*, 5847–5853.

[182] Pekridis, G.; Kalimeri, K.; Kaklidis, N.; Athanasiou, C.; Marnellos, G. *Solid State Ionics* **2007**, *178*, 649–656.

[183] Akoshima, S.; Oishi, M.; Yashiro, K.; Sato, K.; Mizusaki, J. *Solid State Ionics* **2010**, *181*, 240–248.

[184] Bonanos, N.; Mogensen, M. *Solid State Ionics* **1997**, *97*, 483–488.

[185] Kek, D.; Bonanos, N. *Solid State Ionics* **1999**, *125*, 345–353.

[186] Kek, D.; Bonanos, N.; Mogensen, M.; Pejovnik, S. *Solid State Ionics* **2000**, *131*, 249–259.

[187] Srinivasan, S. *Fuel Cells*; Springer US, 2006; Chapter 2, pp 27–92.